

University of Wollongong - Research Online

Thesis Collection

Title: Effect of the starting boron powder on the superconducting properties of MgB

Author: Xun Xu

Year: 2008

Repository DOI:

Copyright Warning

You may print or download ONE copy of this document for the purpose of your own research or study. The University does not authorise you to copy, communicate or otherwise make available electronically to any other person any copyright material contained on this site.

You are reminded of the following: This work is copyright. Apart from any use permitted under the Copyright Act 1968, no part of this work may be reproduced by any process, nor may any other exclusive right be exercised, without the permission of the author. Copyright owners are entitled to take legal action against persons who infringe their copyright. A reproduction of material that is protected by copyright may be a copyright infringement. A court may impose penalties and award damages in relation to offences and infringements relating to copyright material.

Higher penalties may apply, and higher damages may be awarded, for offences and infringements involving the conversion of material into digital or electronic form.

Unless otherwise indicated, the views expressed in this thesis are those of the author and do not necessarily represent the views of the University of Wollongong.

Research Online is the open access repository for the University of Wollongong. For further information contact the UOW Library: research-pubs@uow.edu.au

University of Wollongong Thesis Collections

University of Wollongong Thesis Collection

University of Wollongong

Year 2008

Effect of the starting boron powder on the superconducting properties of MgB

Xun Xu
University of Wollongong

Xu, Xun, Effect of the starting boron powder on the superconducting properties of MgB, PhD thesis, Institute of Superconducting and Electronic Materials, University of Wollongong, 2008. <http://ro.uow.edu.au/theses/353>

This paper is posted at Research Online.
<http://ro.uow.edu.au/theses/353>

NOTE

This online version of the thesis may have different page formatting and pagination from the paper copy held in the University of Wollongong Library.

UNIVERSITY OF WOLLONGONG

COPYRIGHT WARNING

You may print or download ONE copy of this document for the purpose of your own research or study. The University does not authorise you to copy, communicate or otherwise make available electronically to any other person any copyright material contained on this site. You are reminded of the following:

Copyright owners are entitled to take legal action against persons who infringe their copyright. A reproduction of material that is protected by copyright may be a copyright infringement. A court may impose penalties and award damages in relation to offences and infringements relating to copyright material. Higher penalties may apply, and higher damages may be awarded, for offences and infringements involving the conversion of material into digital or electronic form.

Effect of the Starting Boron Powder on the Superconducting Properties of MgB₂

A thesis submitted in fulfillment of the requirements for the award of the
degree of

DOCTOR OF PHILOSOPHY

From the

UNIVERSITY OF WOLLONGONG

By

XUN XU, B. Eng., M. Eng.

Institute for Superconducting and Electronic Materials

2008

DECLARATION

This is to certify that the work presented in this thesis was carried out by the candidate in the laboratories of the Institute for Superconducting and Electronic Materials (ISEM), at the University of Wollongong, NSW, Australia, and has not been submitted for a degree to any other institution for higher education.

Xun Xu

2008

ACKNOWLEDGMENTS

I would like to express my deep gratitude to my supervisors, Prof. S. X. Dou, Dr. M. J. Qin, and Dr. J. H. Kim, for their continuous academic guidance, encouragement, and support during my three years of PhD study in the Institute for Superconducting and Electronic Materials at the University of Wollongong.

I thank Dr. T. Silver for her kind help in proofreading and correcting the English in the manuscripts of my journal articles and this thesis.

I would also like to express my appreciation to Prof. H. K. Liu, Prof. X. L. Wang, Dr. J. Horvat, Dr. J. H. Jiang, Dr. G. Peleckis, Dr. Y. Zhao, and Dr. K. Konstantinov for their contributions to measurements and for useful discussions and valuable suggestions.

This work would not have been completed without the help of Dr. S. K. Chen and Dr. W. K. Yeoh from the University of Cambridge, Mr. M. Tomsic and Mr. M. Rindfleish from Hyper Tech, USA, Dr. S. Choi, Dr. T. Kiyoshi, Dr. T. Nakane, and H. Kumakura from the National Institute for Materials Science (NIMS), Japan, Miss J. H. Lee and Prof. H. W. Park from the Korea University of Technology and Education, Mr. D. Z. Liu from TangShan Weihao Magnesium Powder Co., Ltd., and Prof. P. R. Munroe from the University of New South Wales for their great collaboration.

My special thanks to all my colleagues at ISEM including Mr. D. P. Chen, Mrs. Y. Zhang, Dr. S. Zhou, Mr. W. X. Li, Dr. Z. Rong, M. S. Park, S. H. Ng, S. Y. Chew, J. S. Park, and all the members and technicians at the Faculty of Engineering, especially Mr. R. Kinnell, Mr. G. Tillman, and Mr. N. Mackie, for their friendly help and assistance in using the facilities.

I would also like to acknowledge the Australian Research Council for providing my APAI scholarship and the Research Student Centre at the University of Wollongong who managed my scholarship for their enthusiastic support.

Finally I wish to thank my parents, parents-in-law, and my wife for their patience and support. In particular, without my wife's encouragement, I really would not have been able to continue my academic work. I also believe that my lovely son has given me good luck, as well as a lot of fun. I consecrate this thesis to my wonderful mother, who passed away at the beginning of this year. I wish she could understand my hard work and forgive any mistakes I have made.

Table of Content

ABSTRACT	1
CHAPTER 1: INTRODUCTION.....	4
1.1 BACKGROUND.....	4
1.2 MOTIVATION AND AIMS	6
1.3 THESIS ORGANIZATION:.....	8
1.4 REFERENCES	11
CHAPTER 2: LITERATURE REVIEW ON POLYCRYSTALLINE MGB₂ SUPERCONDUCTOR	13
2.1 INTRODUCTION	13
2.2 “PURE” POLYCRYSTALLINE MGB ₂	20
2.2.1. <i>Discovery of MgB₂</i>	20
2.2.2. <i>Fabrication of MgB₂ conductors</i>	21
2.2.3 <i>Wire and tape preparation</i>	23
2.2.4 <i>Phase transformation and crystal structure of MgB₂</i>	24
2.2.5 <i>Formation of MgO within MgB₂</i>	26
2.2.6 <i>Superconductivity and microstructures of MgB₂</i>	30
2.2.7 <i>Comparison between wire and tape</i>	37
2.2.8 <i>Comparison between in situ and ex situ processing</i>	42
2.3 EFFECT OF BORON POWDER PURITY ON MGB ₂	44
2.3.1 <i>Characteristics of Boron (B)</i>	44
2.3.2 <i>Market trends</i>	44
2.3.3 <i>Influence of Boron Precursor Powders</i>	45
2.3.4 <i>Purification of low-grade boron powders -- acid leaching process</i>	47
2.3.5 <i>Mechanical alloying effect on MgB₂</i>	57
2.4 EFFECTS OF MG PRECURSOR POWDER ON MGB ₂ SUPERCONDUCTIVITY	64
2.4.1 <i>Mg powder</i>	64
2.4.2 <i>MgH₂ powder instead of Mg powder</i>	66
2.5 CHEMICAL DOPING EFFECTS	68
2.5.1 <i>Dual reaction model and dopant categories</i>	68
2.5.2 <i>Carbohydrate Doping</i>	70
2.6 LARGE-SCALE APPLICATION WITH MGB ₂	71

2.7 REFERENCES	75
CHAPTER 3: EXPERIMENTAL TECHNIQUES	86
3.1 SAMPLE PREPARATION AND PROCESSING CONDITIONS	86
3.1.1 Planetary Ball-milling	86
3.1.2 Preparation of bulk and wire samples	88
3.2 SAMPLE CHARACTERIZATION	89
3.2.1 Particle Size Analysis	89
3.2.2 X-ray Diffraction (XRD)	90
3.2.3 Differential Thermal Analysis (DTA)	91
3.2.4 Scanning electron microscopy (SEM), Energy dispersive X-ray spectrometry (EDS), and Transmission electron microscopy (TEM)	93
3.2.5 Brunauer-Emmett-Teller (BET)	93
3.2.6 Measurements of T_c , J_c , H_{c2} , H_{irr}	94
3.3 REFERENCES	99
CHAPTER 4: DIFFERENT MEDIA EFFECT FOR THE MGB₂ BULK SAMPLE BY BALL MILLED HIGH PURITY BORON.....	101
4.1 INTRODUCTION	101
4.2 SAMPLE PREPARATIONS	103
4.3 PHASE INFORMATION AND LATTICE PROPERTIES	104
4.4 SEM STUDIES	107
4.5 INFERENCE ON J_c AND T_c	109
4.6 SUMMARY	112
4.7 REFERENCES	113
CHAPTER 5: INFLUENCE OF BALL-MILLED LOW PURITY BORON POWDER ON THE SUPERCONDUCTIVITY OF MGB₂ BULK SAMPLE.....	115
5.1 MOTIVATION AND SCOPE	115
5.2 EXPERIMENTAL DETAIL	116
5.3 PHASE INFORMATION AND MICROSTRUCTURE OF 96% BORON	117
5.4 PHASE INFORMATION AND LATTICE PARAMETERS	119
5.5 COMPARISON OF T_c , J_c , AND PINNING FORCE	122
5.6 SUMMARY	125
5.7 REFERENCES	126

CHAPTER 6: THE PHASE TRANSFORMATION AND SUPERCONDUCTING PROPERTIES OF MgB_2 BY DIFFERENT BORON SOURCE 127

6.1 OPEN WINDOW FOR LOW PURITY BORON	127
6.2 EXPERIMENTAL DETAIL.....	129
6.3 SEM STUDIES FOR DIFFERENT BORON POWDER.....	131
6.4 PHASE TRANSFORMATION OF MgB_2 SAMPLE WITH DIFFERENT SOURCE	133
6.5 PARTICLE SIZE DISTRIBUTIONS OF BALL-MILLED 96% BORON POWDER	135
6.6 PHASE INFORMATION AND LATTICE PARAMETERS	137
6.7 MGO EFFECT (TWO KNIFE-EDGES)	139
6.8 RESISTIVITY AND CONNECTIVITY EFFECT.....	141
6.9 COMPARISON OF T_c , J_c , AND PINNING FORCE STRENGTH.....	143
6.10 UPPER CRITICAL FIELD AND IRREVERSIBILITY FIELD FROM TRANSPORT MEASUREMENT	146
6.11 CONCLUSION.....	148
6.12 REFERENCES	149

CHAPTER 7: FURTHER STUDY OF TRANSPORT CURRENT DENSITY AND GRAIN CONNECTIVITY IN MgB_2/Fe WIRE MADE FROM BALL-MILLED LOW PURITY BORON..... 150

7.1 WHY NEED WIRE RESULT FOR COMPARISON.....	150
7.2 SAMPLE PREPARATIONS.....	153
7.3 PARTICLE SIZE DISTRIBUTIONS	155
7.4 SEM STUDIES	157
7.5 TRANSPORT CRITICAL CURRENT (J_{ct})	159
7.6 RELATION BETWEEN THE TRANSITION TEMPERATURE AND RESISTIVITY	161
7.7 UPPER CRITICAL FIELD AND IRREVERSIBILITY FIELD FROM TRANSPORT MEASUREMENT	163
7.8 CONCLUSION.....	165
7.9 REFERENCES	166

CHAPTER 8: THE DOPING EFFECTS OF OXYGEN-FREE PYRENE ON THE SUPERCONDUCTIVITY OF MgB_2 WIRES... 167

8.1 PRESENTMENT THE DOPING EFFECTS WITH OXYGEN-FREE CARBON SOURCE	167
8.2 SIMPLY SAMPLE PREPARATION ROUTE	170

8.3 PHASE INFORMATION AND LATTICE PROPERTIES.....	171
8.4 TRANSPORT CRITICAL CURRENT (J_c)	175
8.5 POWER-LAW RELATIONSHIP BETWEEN J_c AND N-VALUE	177
8.6 SUMMARY	179
8.7 REFERENCES	180
CHAPTER 9: PROPERTIES OF CARBON SPHERES DOPED MgB_2	
WIRE BY LOW PURITY BORON POWDER.....	181
9.1 POSSIBILITY OF CARBON SOURCE DOPING EFFECTS IN LOW PURITY BORON	181
9.2 CARBON SPHERES PREPARATIONS.....	183
9.3 MgB_2 WIRE PREPARATIONS	184
9.4 COMPARISON BETWEEN MgB_2 WIRES BY HIGH AND LOW PURITY BORON WITHOUT DOPING	185
9.5 CARBON SPHERES DOPED MgB_2 WIRES BY THE LOW PURITY BORON	190
9.6 CONCLUSION	197
9.7 REFERENCES	198
CHAPTER 10: CONCLUSIONS AND FURTHER WORK.....	200
10.1 CONCLUSION.....	200
10.2 SUGGESTIONS FOR FURTHER WORK	203
PUBLICATIONS	205

List of Figures

Figure 2.1	History of superconductor development with time.....	14
Figure 2.2	Crystal structure of MgB_2 , $a = 3.086 \text{ \AA}$ and $c = 3.524 \text{ \AA}$ [26].....	20
Figure 2.3	The powder-in-tube (PIT) process for the <i>in situ</i> and <i>ex situ</i> methods [38].....	22
Figure 2.4	SEM images of (a) Mg and (b) B powders [24].....	23
Figure 2.5	Differential Thermal Analysis (DTA) for MgB_2/Fe wire.....	24
Figure 2.6	X-ray diffraction (XRD) patterns for un-doped MgB_2/Fe wires sintered at different temperatures. The XRD was performed on the ground MgB_2 cores [23].....	25
Figure 2.7	(a) Lattice parameters and (b) weight fractions of MgB_2 and MgO for samples made at different sintering temperatures [23].....	27
Figure 2.8	Standard Gibbs free energy (ΔG) of $2\text{Mg(s)} + \text{O}_2(\text{g}) = 2\text{MgO(s)}$; $4\text{Mg(s)} + \text{B}_2\text{O}_3(\text{l}) = 3\text{MgO(s)} + \text{MgB}_2(\text{s})$; and $\text{Mg(s)} + 2\text{B(s)} = \text{MgB}_2(\text{s})$ as a function of temperature.....	29
Figure 2.9	Lattice strain versus average grain size (from measured results) as a function of sintering temperature [23].....	31
Figure 2.10	Field emission gun-scanning electron microscopy (FEG-SEM) images of core surface for samples sintered at 650°C ((a) and (b)), 800°C ((c) and (d)), and 1000°C ((e) and (d)) [24].....	32
Figure 2.11	Critical current density (J_c) of all MgB_2/Fe wire samples at 4.2 K and 10 T. Magnetic fields were applied parallel to the wire axis of the MgB_2 wire. Inset shows the $J_c(B)$ of all samples as a function of sintering temperature [24].....	33
Figure 2.12	Resistivity (ρ) of MgB_2/Fe wires as a function of temperature for three samples sintered at different temperatures. Transport measurements for ρ were done using a standard ac four probe method. The inset shows an enlargement of the temperature range around T_c [24].....	34
Figure 2.13	FEG-SEM images of polished core surfaces for samples sintered at (a) 650°C , (b) 800°C , and (c) 1000°C [24].....	36

Figure 2.14	Temperature dependence of irreversibility field (H_{irr}) and upper critical field (H_{c2}) for MgB ₂ /Fe wires sintered at various sintering temperatures for 30 min[24].....	37
Figure 2.15	(a) Transport J_c for round wires and flat tapes at 4.2 K. Inset figure shows the J_c behaviour of referenced wire samples at 4.2 K and 10 T as a function of sintering temperature. (b) Kramer plot (F_K), $J_c^{1/2} \times B^{1/4}$ vs. B , for round wires and flat tapes at 4.2 K [23].....	39
Figure 2.16	SEM images of polished cross-sections for round wire ((a) and (b)) and flat tape ((c) and (d)) [64].....	40
Figure 2.17	SEM image of cross-section of a flat tape. There were cracks in the middle of the core (indicated by white arrows) [64].....	41
Figure 2.18	$J_c(B)$ behaviour of <i>in situ</i> processed flat tape compared to commercial and modified <i>ex situ</i> processed flat tapes [64].....	42
Figure 2.19	FEG-SEM images of samples (a) C98, (b) C99, (c) A9597, and (d) A9999 [67].....	46
Figure 2.20	Magnetic critical current densities versus applied magnetic field at 6 K and 20 K [67].....	47
Figure 2.21	Acid leaching process [68].....	49
Figure 2.22	BET results for different B powders [68].....	50
Figure 2.23	SEM images of different Boron powders [68].....	51
Figure 2.24a	X-ray powder diffraction patterns of MgB ₂ samples made from pure 99% B powder [68].....	52
Figure 2.24b	X-ray powder diffraction patterns of MgB ₂ samples made from 96% B powder [68].....	53
Figure 2.24c	X-ray powder diffraction patterns of MgB ₂ samples made from purified 92% B powder [68].....	54
Figure 2.25	J_c of samples made from different B powders [68].....	56
Figure 2.26	Granulometry for different ball milled MgB ₂ powders: (a) 2 h, distribution peaks 3/30 μ m; (b) 3 h, distribution peaks 1.5/10 μ m; (c) 14 h, distribution peaks 1/7 μ m; and (d) 100 h, distribution peak 1 μ m [69].....	58
Figure 2.27	Transport and inductive measurements of the irreversibility field H_{irr} , for MgB ₂ /Fe tapes prepared with commercial and ball milled powders[69].....	59

Figure 2.28	Dependence of the critical current density on the parallel field for CuNi/Nb double-sheathed tapes with nanocarbon-doped MA precursor annealed at different temperatures [96].....	63
Figure 2.29	SEM images of the magnesium powders with a particle size of (a) 44 μm (Alfa Aesar), (b) 12–17 μm (Tangshan Weihao), (c) 4–6 μm (Tangshan Weihao), and (d) boron powder with 95–97% purity from Tangshan Weihao [103].....	65
Figure 2.30	Comparison of critical current density, J_c , as a function of magnetic field at 5 and 20 K for samples W5, W6, and W7 annealed at 700 °C for 30 min [103].....	66
Figure 2.31	The ASG MRI 0.5 T cryogenic-free magnet [184].....	72
Figure 2.32	The ASG MRI 0.5 T cryogenic-free magnet [184].....	73
Figure 3.1	planetary Ball-milling working principles [8].....	87
Figure 3.2	Principle about determination of the powder particle size [10].....	89
Figure 3.3	X-ray diffract meter in θ - 2θ configuration taken from reference [11]	90
Figure 3.4	Schematic illustration of a DTA cell [14]	92
Figure 3.5	A typical DTA result of a sample with endothermic and exothermic reactions [14].....	92
Figure 3.6	Schematic diagram of magnetic hysteresis loop of a Superconductor showing the width of the magnetic hysteresis loop ΔM [18].....	96
Figure 3.7	Magnetic hysteresis measured on a bulk MgB_2 at 6K up to 7T. The flux jumping is due to thermomagnetic instabilities causing a sudden dissipative re-arrangement of magnetic flux lines [19].....	97
Figure 4.1	The X-ray diffraction patterns for the MgB_2 samples made with and without ball milling in various media.....	105
Figure 4.2	SEM images for the MgB_2 samples.....	107
Figure 4.3	The magnetic critical current density J_c as a function of field for the MgB_2 samples.....	109
Figure 4.4	The T_c curves for the MgB_2 samples.....	110
Figure 5.1	X-ray diffraction patterns for the different B powders.....	117

Figure 5.2	SEM images of the different B powders.....	118
Figure 5.3	X-ray diffraction patterns for MgB ₂ samples made with the different B powders.....	119
Figure 5.4	The magnetic critical current density J_c as a function of field for the MgB ₂ samples.....	122
Figure 5.5	Normalized volume pinning force ($F_p/F_{p,max}$) as a function of field at 20K for the MgB ₂ samples.....	123
Figure 6.1	Scanning electron microscope (SEM) images of (a) 96% B and (b) 99% B. Inset shows a high magnification image of 96% B.....	131
Figure 6.2	Scanning electron microscope (SEM) images for (a) B96, (b) BM4B96, (c) BM8B96, and (d) BM12B96.....	132
Figure 6.3	Differential Thermal Analysis (DTA) for MgB ₂ with different B powders.....	133
Figure 6.4	Particle size distributions for (a) B96, (b) BM4B96, (c) BM8B96, and (d) BM12B96.....	135
Figure 6.5	(a) a - and c -axis lattice parameters, (b) c/a , (c) full width at half maximum (FWHM) of the (110) peak, and (d) lattice strain of MgB ₂ samples using different B.....	138
Figure 6.6	Relative intensity, MgO(220) / MgB ₂ (110) + MgB ₂ (102), as a function of ball-milling time. The inset shows the relative pinning force as a function of field for the different samples.....	139
Figure 6.7	The magnetic critical current density (J_c) for all MgB ₂ samples as a function of external magnetic field at 5 and 20 K.....	143
Figure 6.8	Kramer plot (F_k) of the pinning force, $J_c^{1/2} \times B^{1/4}$, for all samples at 20 K.....	144
Figure 6.9	Temperature dependence of irreversibility field (H_{irr}) and upper critical field (H_{c2}) for all samples with different ball-milling times.....	146
Figure 7.1	Particle size distributions for (a) as-supplied and (b) ball-milled boron powders.....	155
Figure 7.2	Scanning electron microscope (SEM) images at two magnifications for (top) wire sample prepared from as-supplied boron, and (bottom) wire sample prepared from ball-milled boron. All samples were sintered at 700°C for 30 minutes.....	157

Figure 7.3	Transport critical current density (J_{ct}) for all MgB ₂ wires as a function of external magnetic field at 4.2 K.....	159
Figure 7.4	The correlations between (a) the transition temperature (T_c) and the residual resistivity ratio (RRR), and (b) the critical temperature (T_c) and the normalized resistivity (ρ_{norm}).....	162
Figure 7.5	Temperature dependence of (a) the upper critical field (B_{c2}) and (b) the irreversibility field (B_{irr}) for MgB ₂ wires as a function of sintering temperature.....	163
Figure 8.1	(a) a -axis lattice parameter, (b) lattice strain, and (c) fraction of MgO/Mg for pristine MgB ₂ and MgB ₂ + C ₁₆ H ₁₀ /Fe wires as a function of amount of the pyrene. All wire samples were sintered at 650°C for 30 min. The solid line show a linear fit to the data.....	172
Figure 8.2	(a) a -axis lattice parameter, (b) c -axis lattice parameter, and (c) actual amount of carbon (C) substitution (x) in the composition of Mg(B _{1-x} C _x) ₂ for pristine MgB ₂ and MgB ₂ + 10wt% C ₁₆ H ₁₀ /Fe wires as a function of sintering temperature. The wire samples were sintered at 600°C for 4 hours, 620°C for 1 hour, 650°C for 30 min, 700°C for 30 min, and 800°C for 30 min, respectively. The solid line show a linear fit to the data.....	173
Figure 8.3	Transport critical current density (J_c) of pristine MgB ₂ and MgB ₂ + 10wt% C ₁₆ H ₁₀ /Fe wires as a function of applied magnetic field and sintering temperature.....	175
Figure 8.4	Power-law relationship between J_c and n -value, $n \propto J_c^m$	177
Figure 9.1	SEM images of the submicron-sized carbon spheres prepared by hydrothermal treatment of glucose solution at 180°C.....	183
Figure 9.2	XRD patterns of the pure MgB ₂ samples prepared by sintering at different temperatures.....	185
Figure 9.3	Magnetic AC susceptibility as a function of temperature for the pure samples sintered at different temperatures.....	187
Figure 9.4	Critical current density, J_{cm} , as a function of magnetic field at 5 and 20 K for the undoped samples sintered at different temperatures. The J_{cm} of the sample (700°C) prepared from high purity (99%) amorphous boron is included as reference.....	188
Figure 9.5	Temperature dependence of H_{c2} and H_{irr} for the pure samples sintered at 650 and 800°C, and the sample prepared from 99% amorphous boron sintered at 700°C.....	190

Figure 9.6	The (002) and (110) XRD reflections of the pure, 5 and 10 wt.% CS doped samples. The heat treatment temperature for these samples is 800°C.....	192
Figure 9.7	Critical current density, J_{cm} , as a function of magnetic field at 5 and 20 K for the pure and CS doped samples.....	193
Figure 9.8	The H_{c2} and H_{irr} of the pure and CS doped samples sintered at 800°C as a function of reduced temperature (T/T_c).....	194
Figure 9.9	Normalized flux pinning force as a function of reduced magnetic field at 20 K for the pure and CS doped samples sintered at 800°C. The solids lines corresponds to the function $h^p(1-h)^q$ with different p and q values representing different pinning mechanisms.....	195

List of Tables

Table 2.1	Source, form, and purity of the different boron powders with their particle size distribution [67].....	45
Table 2.2	Nominal purity, impurities, grain size, and crystallinity of boron precursor powders from different suppliers [69].....	60
Table 2.3	Synthesis parameters, structural analysis by x-ray diffraction, microstructure analysis by SEM-EDX and superconducting properties of hot pressed bulk samples [69].....	62
Table 2.4	Synthesis parameters, microstructure analysis by SEM-EDX and superconducting properties of tapes [69]	54
Table 2.5	Ranking of dopants by Dual Reaction Model [Dou, 2007-EUCAS]....	69
Table 4.1	The full-width at half maximum (FWHM) of 3 main peak positions and lattice parameters for the MgB ₂ samples made with and without ball milling in various media.....	104
Table 5.1	The lattice constants and structural features for the MgB ₂ samples made with the different B powders.....	121
Table 6.1	The measured resistivity values, residual resistivity ratios (RRR), and active cross-sectional area fraction (A_F) for MgB ₂ with different ball-milling times.....	141
Table 7.1	The measured resistivity values, residual resistivity ratios (RRR), active cross-sectional area fractions (A_F), critical temperatures (T_c), and lattice strain for MgB ₂ wire made from ball-milled boron and from as-supplied boron under comparable sintering conditions.....	158
Table 9.1	Summaries of characteristic data for the pure and CS doped MgB ₂ samples sintered at 800°C.....	192

Abstract

The effect of the properties of the starting boron powders on the superconducting properties of MgB_2 has been studied. Low grade boron powders are attractive because of their low cost, but produced lower surface reactivity and larger particle size than high purity (99%) amorphous boron powder, indicating that the low grade powders cannot be used to achieve the same superconducting properties as those of samples made from pure 99% boron powder. However, the low purity boron powders can be improved by using simple physical and chemical processes, leading to enhanced magnetic critical current density, J_c . In order to get high performance MgB_2 , it is obviously important to control the phase composition and microstructure of the boron starting powders and the solid state reaction conditions.

Ball milling is an effective method to reduce the boron particle size, so, the effects of ball milling boron powders in different media, such as acetone, ethanol, and toluene, on the superconducting properties of MgB_2 needed to be considered and studied. It was observed that toluene was the most effective medium of them all for enhancing J_c . J_c was estimated to be $5 \times 10^3 \text{ A cm}^{-2}$ at 8 T and 5 K for a sample that was ball milled in toluene. This value is much higher than that of the pure MgB_2 reference sample that was not ball milled, by a factor of 20. It was considered that ball milling B using toluene leads to smaller MgB_2 grains, resulting in enhanced J_c at low operating temperatures and high fields.

MgB_2 samples were prepared using as-supplied commercial 96% boron with strong crystalline phase and the same 96% boron (B) after ball milling. The effects of the properties of the starting B powder on the superconductivity were evaluated. It was

observed that samples using ball-milled 96% B, in comparison with the reference sample made from the as-supplied 96% B, were characterized by small grain size and enhanced magnetic critical current density (J_c), which reached $2 \times 10^3 \text{ A cm}^{-2}$ at 5 K and 8 T. The improved pinning seen in these samples seems to be caused by enhanced grain boundary pinning at high field. MgB_2 samples were also prepared by using 96% boron powder with strong crystalline phase that had been ball milled for various times. Based on Rowell connectivity analysis, when the ball-milling time increased, the connectivity factor, described as the active cross-sectional area fraction (A_F), was decreased. This implies that the inter-grain connectivity became worse. These properties could lead to poor J_c in low field. However, the pinning force strength of samples using ball-milled 96% B is larger than that of the reference sample using as-supplied commercial 96% B powder. These results accompany enhanced irreversibility (H_{irr}) and upper critical fields (H_{c2}).

Furthermore, the magnetic field dependence of the transport critical current density (J_{ct}) and the grain connectivity of MgB_2/Fe wires fabricated from ball-milled boron have been investigated in detail, and strong correlations have been found, as evidenced by differences in grain size, critical transition temperature, and resistivity. It was observed that the samples fabricated by ball milling had relatively small grain sizes, resulting in a weaker field dependence of the J_{ct} in the high field region. On the other hand, the ball-milled boron was associated with poor connectivity between adjacent grains. It is clearly shown that the observed reduction in low field J_{ct} is related to the reduction in the superconducting area fraction that is reflected by the connectivity factor. Even though high temperature sintering could always compensate for the degradation of the J_{ct} in the low field region, the subsequent grain growth in this case was mainly responsible for the degradation of J_{ct} in the high field region. The strong correlation

between the grain size and the connectivity can change the field dependence of the J_{ct} , and both these factors are primarily affected by the sintering temperature and by the presence and extent of ball milling.

In the MgB_2 field, chemical doping is the most popular way to improve the superconductor properties. It has been reported that significantly enhanced critical current density in MgB_2 superconductor could be easily obtained by doping with a hydrocarbon, highly active pyrene ($C_{16}H_{10}$), while using a sintering temperature as low as $600^\circ C$. The processing advantages of the $C_{16}H_{10}$ additive include production of a highly active carbon (C) source, an increased level of disorder, and the introduction of small grain size, resulting in enhancement of J_c .

Using the same concept, low purity boron powders were used to fabricate pure and submicron-sized carbon sphere doped MgB_2 superconductor. The boron powders used showed low reactivity towards MgB_2 formation, as compared to high purity (99%) amorphous boron, which might result from the larger grain size and the existence of crystalline boron or boron oxide in the former. However, the samples prepared from this boron powder showed comparable J_c values at 20 K and in low field (<1 T) to those from a sample prepared from 99% amorphous boron. Doping submicron-sized carbon spheres successfully introduced carbon substitution for boron, and so improved the H_{c2} , H_{irr} , and in-field J_c properties of the MgB_2 .

Chapter 1: Introduction

1.1 Background

Enormous research efforts have been made into areas such as materials performance properties, wire conductor development, and magnet demonstrations in the MgB₂ field since its discovery in 2001 [1]. It is well known that the critical current density (J_c) of pure MgB₂ is drastically decreased in an increasing external magnetic field, because of its poor flux pinning properties when compared to low temperature superconductors (LTS). Quite interestingly, however, unique features of the superconductivity observed in MgB₂ are related to its two-band nature and the lack of weak-links at the grain boundaries [2]. In addition, the advantages of the simple binary composition, the transition temperature of 39 K, and the low cost of the starting materials have been sufficient to put it on the road to real applications.

Specifically, the best self-field critical current density (J_c) of MgB₂ conductor fabricated by the powder-in-tube (PIT) method has passed 10^5 Acm^{-2} for operating temperatures up to 20 K. In the real market, nevertheless, the cost and performance of MgB₂ play a significant role in determining its value as a replacement for conventional conductors and other low and high temperature superconducting materials. For instance, MgB₂ conductor has a very low materials cost at $\$0.20 \text{ m}^{-1}$ (depending on the total current and current density, it is better to use 1000 A meter unit), which translates into $\$1.00 \text{ m}^{-1}$ for finished strands and approximately $\$1.00 \text{ kA}^{-1} \text{ m}^{-1}$ at 2 T and 4.2 K, based on a published report [3]. Therefore, MgB₂ superconductor is one of the most promising

candidates for magnet applications, when compared to Nb-Ti and Nb₃Sn, especially since its T_c of 39 K can be applied in a convenient cryogen-free magnet to work at an operating temperature of 15 - 20 K.

1.2 Motivation and Aims

From the cost point of view, furthermore, high grade ($> 99\%$) amorphous boron (B) powder is about 10 times more expensive than low grade (96-97%) B powders, which contain some crystalline phase. Eventually, low purity starting materials are expected to have a great impact on the production economics, if the low purity B powders can be used to produce commercial MgB_2 conductors. However, there are still considerable advantages in the 99% B, i.e., amorphous B with $> 99\%$ grade has high reactivity compared to low grade 96% B, making possible a decreased sintering temperature without compromising quality. To attain the desirable properties of 99% B, the properties of the low grade B powders, such as purity, size distribution, particle size, etc., need to be well studied and systematically analysed, as they can play an important role in determining the fundamental properties of the MgB_2 .

It has been reported that samples made from crystalline boron powders have around an order of magnitude lower J_c than samples made from amorphous precursors [4]. Gas phase plasma methods for powder production have been used to promote intimate mixing of the doping components on an atomic scale in the initial boron powder production, so that both the grain size and the precipitate size have been reported to be smaller [5]. It has also been found that the enhancement in J_c from mixing MgB_2 with $\text{MgH}_2 + 2\text{B}$ is due to the optimization of densification by the addition of MgB_2 and improvement in grain coupling, depending on the phase formation of MgB_2 from $\text{MgH}_2 + 2\text{B}$ [6]. In another study, elementary boron was obtained via an acid leaching process, after reacting B_2O_3 and Mg in an argon atmosphere at 800°C . Energy dispersive x-ray spectroscopy (EDX) results revealed that the powder obtained from the reaction was

boron of 92% purity with magnesium as the major impurity [7]. The effect of B powder purity on J_c and critical temperature, T_c , has also been found to be noticeable [8]. Currently, in order to achieve the highest J_c , high purity amorphous B powders (99%) are used. However, in practical applications, the cost of the materials must be considered. If 92% or 96% boron powders can be used to make MgB_2 , the material cost could be decreased significantly.

To improve these properties, various methods have been reported. They include, for example, a ball-milling method [9], a thermo-mechanical processing method [10], and the use of an acid leaching process [10]. Among them, the ball-milling method is particularly interesting, as size control of the starting material may induce more effective pinning without any dopants.

On the other hand, the critical current density (J_c) and the low irreversibility field (B_{irr}) of ~ 8 T, compared to commercial low temperature superconductors such as the Nb-based ones, need to be further improved, especially for magnet applications.

1.3 Thesis Organization:

Chapter One introduces the background of this work. The motivation and aims are outlined, and the organization of the thesis is presented.

Chapter Two reviews 5 parts of the relevant work:

- The progress on the materials processing and characterization of polycrystalline superconducting MgB_2 conductors based on pure boron powder (99%, amorphous).
- The influence of the nature of the boron precursor on the superconducting properties of polycrystalline MgB_2 compared to that made from amorphous boron.
- Some study of the effect of the initial MgB_2 powder grain size shows that both the J_c and B_{irr} in ex situ Fe/ MgB_2 tapes are enhanced after reducing the initial powder by ball milling to sizes of the order of $3\text{ }\mu\text{m}$ under Ar atmosphere, while B_{c2} remains unchanged. Mechanical alloying is a handy, simple and useful processing technique in the performance point of view that is now being employed in the production of nano-crystals and/or nano-particles from all material classes. The performance depends on various factors such as the type of ball and jar, size of the ball, ball to powder ratio, speed and time of milling.
- The demonstration of a unified mechanism, according to the dual reaction model, by which the optimal doping effect can be achieved when C substitution and MgB_2 formation take place simultaneously at low temperatures.
- Significant progress has been made on the development of MgB_2 superconductor wires and coils. Many groups around the world are now focusing on the

electrical and mechanical properties of MgB_2 wire. As the improvement on the performance, the price performance at 4 K operation could exceed both NbTi and Nb_3Sn superconductor wire and enable several commercial applications using MgB_2 conductors. In the future, it is positive for MgB_2 superconductors will be directed toward commercial applications.

Chapter Three describes the techniques and methods used for characterizing samples.

Chapter Four demonstrates the effects of ball milling pure boron (B) powder (99%, amorphous) using different media, such as acetone, ethanol, and toluene. Using toluene has led to enhancements in the magnetic critical current density (J_c) in high field [11].

Chapter Five also discusses samples prepared from low grade boron (96%) with semi-crystalline phase via ball-milling in toluene as well. The results of this have demonstrated the possibility and cost effectiveness of fabricating high performance samples using low grade boron [12].

Chapter Six argues that the benefits of ball-milling processing could be related to the small grain size and poor crystallinity. Specifically, the MgO fraction was increased within the matrix through ball milling, which influences properties such as flux pinning. Further study of the ball-milling process thus promises to allow adjustment of the desired phase form, which should be optimized along with the sintering conditions, so as to create a balance between the inter-grain connectivity and the pinning centres [13].

Chapter Seven concerns wire processing, which further promotes grain connectivity due to the high pressure applied to the sample, resulting in different performances of conductors and pellets. Therefore, we need to evaluate the correlation between the transport current density and the grain connectivity in wire conductor .

Chapter Eight reports on carbon doping of MgB_2 using various carbon sources. It is found to be especially effective in enhancing the upper critical field of MgB_2 . So far, there are quite a few carbon sources that have been tried, such as nano-SiC, B_4C , carbon nanotubes, nano-carbon, hydrocarbons, etc. One common feature of these successful carbon dopants is that they are initially of nanometre size or they can be evenly mixed with boron powders in the liquid state. A higher sintering temperature is usually necessary for most of the other C sources, leading to crystalline growth and worse pinning. The use of low temperature processing is also crucial for selection of various sensitive sheath materials and the reduction of production costs. It is suggested that a different hydrocarbon, pyrene ($\text{C}_{16}\text{H}_{10}$), without any oxygen content, might act as a superior C source [14].

Chapter Nine presents results from doping with submicron-sized carbon, although this only achieved limited success. In this chapter, the doping effects of reactive submicron-sized carbon spheres (CS), which were prepared by hydrothermal treatment of glucose solution, on the properties of MgB_2 superconductor, were investigated [15].

Chapter Ten contains a general conclusion and suggestions for further work. A list of published works is given at the end of the thesis.

1.4 References

1. J. Nagamatsu, *Nature* **410** 63-64, (2001).
2. D. C. Larbalestier, M. O. Rikel, L. D. Cooley, A. A. Polyanskii, J. Y. Jiang, S. Patnaik, X. Y. Cai, D. M. Feldmann, A. Gurevich, A. A. Squitieri, M. T. Naus, C. B. Eom, E. E. Hellstrom, R. J. Cava, K. A. Regan, N. Rogado, M. A. Hayward, T. He, J. S. Slusky, P. Khalifah, K. Inumaru, and M. Haas, *Nature* **410** 186, (2001).
3. L. D. Cooley, A. K. Ghosh, and R. M. Scanlan, *Supercond. Sci. Technol.* **18** R51, (2005).
4. S. K. Chen, K. A. Yates, M. G. Blamire, and J. L. MacManus-Driscoll, *Supercond. Sci. Technol.* **18** 1473, (2005).
5. J. V. Marzik, R. J. Suplinskas, R. H. T. Wilke, P. C. Canfield, D. K. Finnemore, M. Rindfleisch, J. Margolies, and S. T. Hannahs, *Physica C* **423** 83, (2005).
6. H. Fujii, K. Togano, and H. Kumakura, *Supercond. Sci. Technol.* **15** 1571, (2002).
7. M. Yavas, S. Okur, M. Egilmez, M. Kalkanci, and L. Ozyuzer, *Journal of Optoelectronics and Advanced Materials* **7** 407, (2005).
8. S. H. Zhou, A. V. Pan, J. Horvat, M. J. Qin, and H. K. Liu, *Supercond. Sci. Technol.* **17** S528, (2004).
9. H. Fang, S. Padmanabhan, Y. X. Zhou, and K. Salama, *Appl. Phys. Lett.* **82** 4113-4115, (2003).
10. X. Xu, M. J. Qin, K. Konstantinov, D. Dos Santos, W. K. Yeoh, J. H. Kim and S. X. Dou, *Supercond. Sci. Technol.* **19** 466–469, (2006).
11. X. Xu, J. H. Kim, W. K. Yeoh, Y. Zhang, and S. X. Dou, *Supercond. Sci. Technol.* **19** L47, (2006).
12. X. Xu, J. H. Kim, W. K. Yeoh, M. Rindfleisch, M. Tomsic, Dayse I. dos Santos, and S. X. Dou, *IEEE Trans. Appl. Supercond.* **17** (2) 2782, (2007).
13. X. Xu, J. H. Kim, M. S. A. Hossain, J. S. Park, Y. Zhao, S. X. Dou, W. K. Yeoh, M. Rindfleisch, and M. Tomsic, *J. Appl. Phys.* **103** 023912, (2008).

14. J. H. Kim, X. Xu, M. S. A. Hossain, D. Q. Shi, Y. Zhao, X. L. Wang, S. X. Dou, S. Choi, and T. Kiyoshi, *Appl. Phys. Lett.* **92** 042506, (2008).
15. C. H. Jiang, X. Xu, and S. X. Dou, *Supercond. Sci. Technol.* **21**(6) 5006, (2008).

Chapter 2: Literature Review on Polycrystalline MgB_2 Superconductor

2.1 Introduction

The history of superconductivity was closely related to low temperature research, H. Karmelinh Onnes liquefied helium in 1908 which he then used as a coolant. It was later realised that the highest superconducting transition temperature, T_c measured for pure elements was only around 9.25 K for Nb. Consequently, the compound of Nb_3Ge with A15 structure was found to show higher T_c at 23.2 K. The puzzling phenomenon of superconductivity was explained by the BCS theory in 1957. According to the theory, the electrical transport in superconductors is due to the pairing of electrons (Cooper pairs) with opposite moment and spins instead of single electrons. The coherent travelling of electron pairs leads to resistance-less current flow through a superconducting material.

In 1986, higher T_c , above 30K was observed in the Ba-La-Cu-O system. The T_c of this compound went up to 52 K under high pressure. Following this, Wu *et al.* reported the superconducting phase above 93 K in Y-B-Cu-O system, i.e. higher than the liquid nitrogen temperature. In a short while, Tl-Ba-Cu-O and Bi-Sr-Ca-Cu-O systems were found to exhibit T_c of 125 K and 110 K, respectively. Later on, Hg-Ba-Ca-Cu-O was shown to be superconducting at 134 K and goes up to 153 K under high pressure. In these highly anisotropic materials, it is believed that the quasi two dimensional-like Cu-O layers are the key to the origin of high T_c value. Recently, a simple binary compound

conductors and is competitive with other superconductors, such as Nb-based, Bi-based, and Y-based materials. The fabrication of MgB₂ conductor in lengths > 1 km and stabilized form is now a technology of great interest [1-3]. However, to make MgB₂ really viable, the critical current density (J_c) of MgB₂ conductor must be raised considerably.

So far, different kinds of powder-in-tube (PIT) processes for MgB₂ conductor, i.e., *ex situ* and *in situ* processes, have been developed, which show different advantages [4]. Even though J_c for *in situ* processed MgB₂ conductor in particular shows the better result at present, it is still not at the highest levels achieved by Nb-Ti low temperature superconductor (LTS). The main reason is that connectivity between grains is very low. Using the methodology of Rowell to estimate the grain connectivity has suggested that the connection factor for polycrystalline MgB₂ is below 0.2 [5]. On the other hand, MgB₂ thin film fabricated by hybrid physical-chemical vapour deposition (HPCVD) has a higher density and better connectivity, resulting in improvement of J_c [6]. For these reasons, the J_c values of round wire could be further improved if the core density of these wires can be increased by the optimization of wire fabrication, especially mechanical deformation. It has been speculated that the low core density of round wire is related to the low J_c value. However, round wire is preferred against a flat tape to achieve low AC loss and to support a layered coil winding [7]. The necessity to improve the J_c for competition with Nb-Ti and Nb₃Sn LTSs is driving the work on the optimization of MgB₂ conductors.

Further enhancement of intergranular J_c has remained a topic of great scientific and technological interest. For example, the current path of MgB₂ is locally limited by the

presence of secondary phases or lattice defects [8]. Oxygen (O)-rich secondary phases, particularly MgO, may be of great importance and yield a positive effect for J_c if the particle size is of the order of the coherence length ($\xi^{ab}(0)$) of MgB₂, ~ 6.5 nm. The intergranular J_c in polycrystalline MgB₂ is also limited by various factors, such as poor connectivity between superconducting grains and chemical heterogeneity at the grain boundaries [9]. The impurities or chemical inhomogeneities at the MgB₂ grain boundaries could act as a source of weak-links [10-12]. The major challenge is how to overcome the major inter-grain connectivity limitations of MgB₂ to raise J_c as a whole. It is thus necessary to study the fabrication parameters related to the superconductivity of MgB₂. Endeavours in these directions help us to understand the relationship between fabrication parameters and excellent J_c .

In addition, pinning mechanisms have been widely studied for almost all types of MgB₂ samples [13-22]. There are two main pinning mechanisms: one is inter-grain boundary pinning, and the other is point defect pinning. However, among the different types of MgB₂ samples, only c -axis oriented films have been suitable for the study of pinning mechanisms until now. Polycrystalline samples could not be used to study the pinning mechanism due to the random orientations of grains with anisotropic superconductivity, which affects the field dependence of J_c and the determination of pinning mechanisms.

In this chapter, therefore, I firstly review the progress on the materials processing and characterization of polycrystalline superconducting MgB₂ conductors. MgB₂/Fe conductors, such as round wires and flat tapes, were fabricated by using the PIT method and samples sintered at different temperatures, and then I evaluated the strong correlations among phase transformation, changes in the a -axis and c -axis lattice

parameters, impurity phases, full width at half maximum (FWHM), T_c , transport J_c , upper critical field (H_{c2}), irreversibility field (H_{irr}), and resistivity (ρ). These properties of *in situ* processed MgB_2/Fe conductor are compared, taking into account the microstructures. In addition, J_c , flux pinning strength, and microstructures were evaluated for both wire and tape samples.

Secondly, the influence of the nature of the boron precursor on the superconducting properties of polycrystalline MgB_2 will be discussed, mostly with respect to its effects on critical current density, resistivity, and phase formation. It is shown that MgB_2 samples made from crystalline boron powders have about an order of magnitude lower J_c compared to those made from amorphous boron. The low purity boron powders produce lower surface reactivity and larger particle size in the MgB_2 than the high purity boron powder, indicating that the low purity powders cannot be used to achieve the same superconducting properties as those of samples made from the high purity boron powder. However, the low purity boron powders can be improved by using a simple chemical process, leading to enhanced magnetic J_c .

Thirdly, the use of mechanical alloying (MA) for the preparation of MgB_2 superconductors was shown to be an appropriate technique that yields a highly pure, homogeneous, and refined particle size, thus, enhancing flux pinning ability of the grain boundaries. In practically Ball-Milling is an important processing technique that will be improve the manufacturability of MgB_2 samples. More recently, it was demonstrated for MgB_2 with carbon doping under high-energy mechanical milling combined with HIP that substantial enhancement of the critical current density and the upper critical field can be obtained.

The fourth part of the review considers the enormous research efforts that have been directed at MgB₂ in the past seven years since its discovery in 2001. Significant breakthroughs in the improvement of critical current density (J_c), the irreversibility field (H_{irr}), and the upper critical field (H_{c2}) were achieved through chemical doping, in particular using SiC, carbon nanotubes (CNT), and C nanoparticles. A record H_{c2} (4.2 K) of 43 T has been achieved with nano-SiC and CNT doped MgB₂. These important advances in MgB₂ conductor properties have had a significant impact on the development of technical MgB₂ superconductors. These breakthroughs have been confirmed by leading groups around the world. The most recent report shows that 4.2 K J_c of 10^5 A/cm² and 10^4 A/cm² at 8 T and 16 T have been achieved with C-doped MgB₂ wires [81]. As the result of the significant enhancement in $J_c(H)$ by nanoscale SiC doping, MgB₂ wires for large scale applications have become more competitive in comparison with all other superconductors. On the basis of systematic studies, Prof. Dou was able to propose a dual reaction model to demonstrate a unified mechanism, according to which the optimal doping effect can be achieved when the C substitution and MgB₂ formation take place simultaneously at low temperatures. The dual reaction concept has led to the discovery of the advantages of carbohydrate doping in MgB₂, resulting in significant enhancements in J_c , H_{irr} , and H_{c2} . The dual reaction model can provide comprehensive assessment of many other dopants, as well as leading to the selection of dopants suitable for enhancing the performance properties of MgB₂.

In the end, it demonstrates that the MgB₂ superconductors have the potential to be integrated in a variety of commercial applications such as magnetic resonance imaging, fault current limiters, transformers, motors, generators, adiabatic demagnetization

refrigerators, magnetic separation, magnetic levitation, energy storage, and high energy physics applications.

2.2 “Pure” polycrystalline MgB₂

2.2.1. Discovery of MgB₂

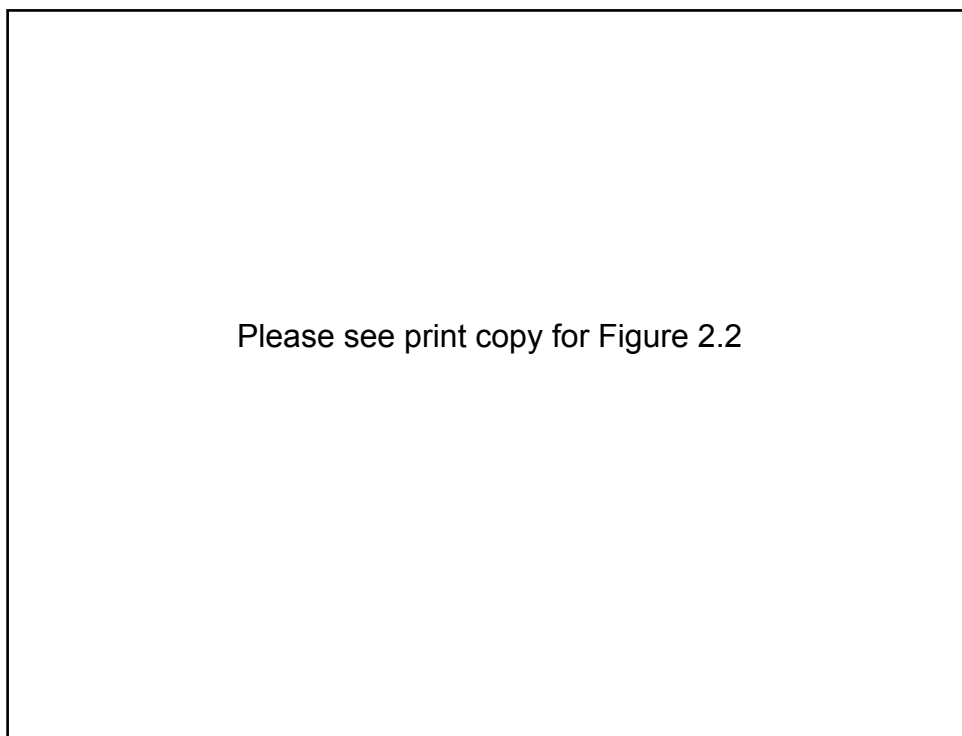


Figure 2.2 Crystal structure of MgB₂, $a = 3.086 \text{ \AA}$ and $c = 3.524 \text{ \AA}$. [26]

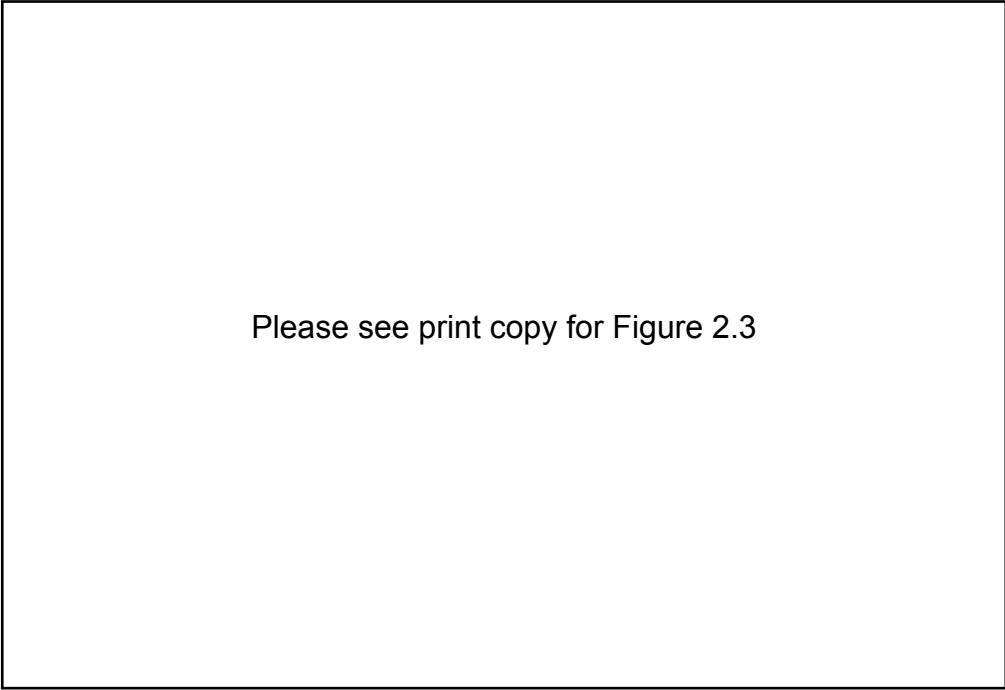
MgB₂ is an inter-metallic, polycrystalline material that has been known since 1953 and was used in the commercial preparation of elemental boron (B). It was not known to be superconducting until this property was accidentally discovered by Jun Akimitsu and his colleagues [25]. MgB₂ consists of alternating layers of boron and magnesium atoms in a hexagonal structure, as shown in Figure 2.2. L. H. He *et al.* analysed the crystal structure of MgB₂ using the Rietveld method [26]. They found that the compound has hexagonal symmetry (Space Group P6/mmm) with the unit cell lattice parameters: $a =$

0.308136(14) nm and $c = 0.351782(17)$ nm. Similar conclusions on the crystal structure were soon made on the basis of studies using high resolution transmission electron microscopy (HRTEM) [27], high resolution powder neutron diffraction [28], and electron energy loss spectroscopy (EELS) [29].

Up to now, MgB_2 has attracted considerable experimental and theoretical research efforts [30-34] because of its high T_c of 39 K. Besides the high T_c , its simple crystal structure, large coherence length, high critical field, transparency of grain boundaries, and low normal state resistivity have made this material a fascinating topic to study for both large scale applications and electronic devices. Moreover, the presence of two-gap superconductivity (π and σ bands) has been theoretically and experimentally established. In addition, it shows a significant isotope effect like a low temperature superconductor.

2.2.2. Fabrication of MgB_2 conductors

In the *ex situ* processing method, already formed MgB_2 powder is packed into metallic tubes and processed [35-38]. This type of processing is more reliable for obtaining high density and a homogeneous core for wires. High performance J_c is measured for *ex situ* processed MgB_2 conductors, even without any heat treatment. However, doping with impurities is not effective compared to *in situ* processing. In addition, commercially reactive MgB_2 powder exhibits a broad particle range from the submicron scale up to > 100 nm, including agglomerates.



Please see print copy for Figure 2.3

Figure 2.3 The powder-in-tube (PIT) process for the *in situ* and *ex situ* methods [38].

On the other hand, mixed Mg and boron (B) powders for *in situ* processing are packed into a metallic tube, and this is followed by heat treatment [39-42]. The heat treatment is usually done at 650 – 900°C under oxygen (O) protective conditions or vacuum. Figure 2.3 shows the powder-in-tube process for the *in situ* and *ex situ* methods.

The *in situ* route offers the advantage that impurity particles of a secondary phase can be added to the powder mixture. These are distributed in the microstructures of the MgB₂ and constitute the primary means of hindering grain growth during phase formation. Up to now, SiC is the most effective additive when added at 10 wt% in the form of 15 nm - 30 nm small particles [43]. However, most solid type nano-particle dopants have been rendered less effective by the agglomeration behaviour of the nano-particles, and it is still difficult to uniformly disperse nanometer sized particles into a reaction powder such as B. Recently, Kim *et al.* were the first to report that carbohydrate doped MgB₂ bulks fabricated by a chemical solution route exhibited an enhancement of $J_c(B)$ properties, as determined by a magnetic measurement [44]. Even

though O is present in carbohydrate (e.g. malic acid, $C_4H_6O_5$), they suggested that a carbohydrate as an organic reagent could introduce homogeneous mixing [45]. In addition, due to the fact that most carbohydrates decompose at temperatures below the formation temperature of MgB_2 , highly reactive and fresh carbon (C) on an atomic scale can be introduced, hence, they argued that C substitution for B can take place at as low a temperature as the formation temperature of MgB_2 [46].

2.2.3 Wire and tape preparation

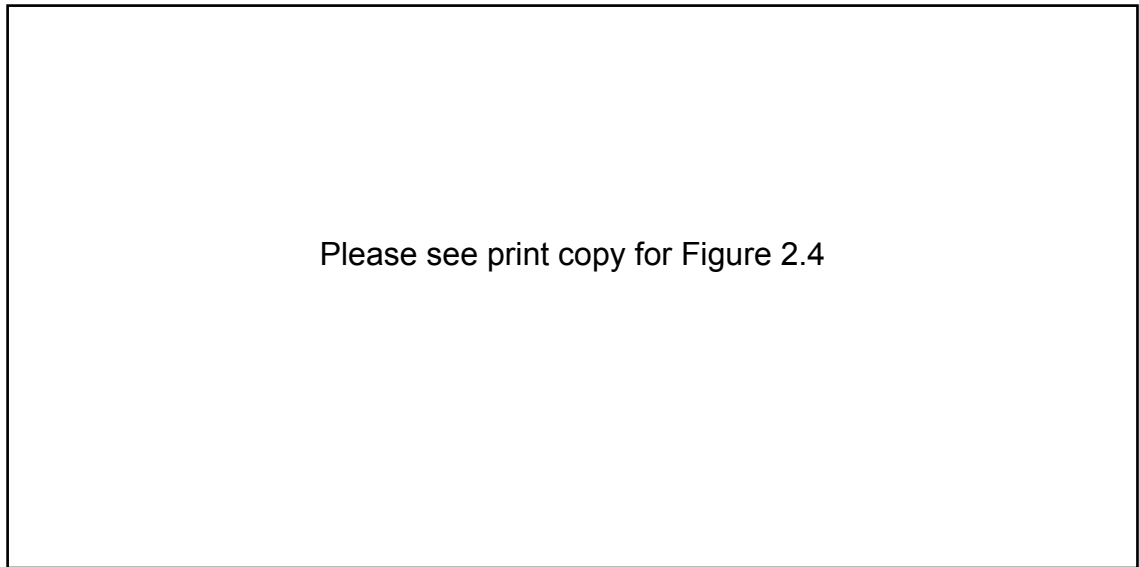


Figure 2.4 SEM images of (a) Mg and (b) B powders [24].

MgB_2 /Fe conductor was fabricated by the *in situ* PIT process. The detailed procedures for making wires have been reported elsewhere [23, 24, and 47]. Magnesium (Mg, 99%) and boron (B, 99%) powders were used as starting materials with the composition of MgB_2 . The mixed powders were packed into an iron (Fe) tube with a length of 140 mm. The Fe tube had an outer diameter (O.D.) of 10 mm and an inner diameter of 8 mm. The composites were drawn to an O.D. of 1.42 mm. To make flat tape, the round wire samples were then rolled to a thickness of 0.5 mm. The thickness of flat tape was decreased by thickness reductions of 0.1 mm, from 1.4 mm to 0.5 mm. The fabricated conductors were sintered at a range of temperatures from 650°C to 1000°C for 30 min

under high purity argon (Ar) gas and then cooled in the furnace. The heating rate was $5^{\circ}\text{Cmin}^{-1}$. Figure 2.4 shows SEM images of the (a) Mg and (b) B powders that were used.

2.2.4 Phase transformation and crystal structure of MgB_2

To decide the sintering range of the MgB_2/Fe wire, differential thermal analysis (DTA) results for MgB_2/Fe wire and bare Fe were evaluated, as can be seen in Figure 2.5. The heating rate used was $5^{\circ}\text{C min}^{-1}$ in Ar gas in order to maintain the same sintering conditions as the bulk samples. For the MgB_2/Fe ($\text{Mg}+2\text{B}+\text{Fe}$) sample, there were two

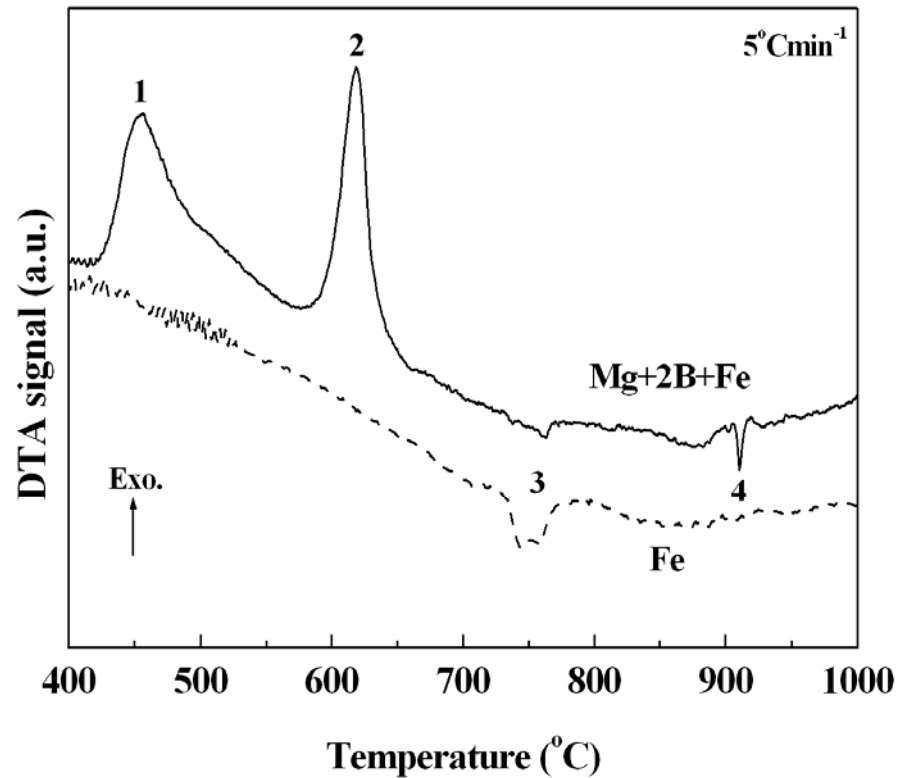


Figure 2.5 Differential Thermal Analysis (DTA) for MgB_2/Fe wire and bare Fe.

exothermal peaks and two endothermal peaks, while the Fe had only one endothermal peak. In the case of the first exothermal peak (peak 1 in the figure), this is related to the reaction between melting B_2O_3 and Mg, i.e, Mg reacts with B_2O_3 to form MgO. The

reason for the existence of B_2O_3 is because the surface of the commercial B powder has partially oxidized. From x-ray diffraction (XRD) (not shown), it was observed that there were B_2O_3 peaks ($2\theta \approx 14.6^\circ$ and 27.8°) in the B powder. The second exothermal peak (peak 2) could be associated with MgB_2 formation [48-51]. On the other hand, the broadened endothermal peak (indicated by 3) at around $750^\circ C$ for Fe is probably related to the Curie temperature of bare Fe. The second endothermal peak (indicated by 4) at around $910^\circ C$ is due to the formation of Fe_2B at the interface between the core and the sheath. It can be understood that the MgO formation starts from $425^\circ C$, that MgB_2 phase starts to form at $575^\circ C$ and then finishes at $640^\circ C$, and that the Fe_2B phase forms above $910^\circ C$ when a heating rate of $5^\circ Cmin^{-1}$ is used. As a result, it was concluded that the appropriate sintering range should be $650^\circ C$ to $900^\circ C$ for MgB_2/Fe conductor.

Please see print copy for Figure 2.6

Figure 2.6 X-ray diffraction (XRD) patterns for un-doped MgB_2/Fe wires sintered at different temperatures. The XRD was performed on the ground MgB_2 cores [23].

The XRD patterns for MgB_2 as a function of sintering temperature are shown in Figure 2.6. The XRD was performed on the ground MgB_2 cores. As can be seen in the Figure, all samples sintered at 650°C to 900°C seem to be well developed MgB_2 with a small amount of MgO. However, the sample sintered at 1000°C was observed to contain Fe_2B as a second phase, as mentioned above. The Fe_2B could be associated with a direct reaction in the interfacial layer between the MgB_2 core and the Fe sheath [52-54]. This can be explained by the formation temperature of MgB_2 , which is relatively lower than that of Fe_2B .

Figure 2.7 shows (a) the lattice parameters and (b) the weight fractions of MgB_2 and MgO made at different sintering temperatures. It was observed that the lattice parameters did not change within the sintering temperature range of 650°C to 900°C within the accuracy of error. That is, the XRD spectra did not show any peak shifting in the samples. It is to be noted that the weight fraction of MgO also remained constant, ~10%, regardless of the different sintering temperatures. The lattice parameters did not change within the sintering temperature range.

2.2.5 Formation of MgO within MgB_2

Intergranular connection between the grains may be locally limited by the presence of secondary phases such as MgO at the grain boundary, resulting in depression of superconductivity [5]. However, Jiang *et al.* reported the effect of MgO addition on the J_c of MgB_2 tape [55]. They found that light doping with nano-MgO (< 2.5wt%) could increase the J_c of MgB_2 tapes through enhancing the grain connectivity and core density. The nanoparticles could enhance the flux pinning effect according to two-gap superconductivity theory. Since the $\xi^{ab}(0)$ of MgB_2 is approximately 6-7 nm, partial inclusion of nanosized particles within grains could result in strong flux pinning centres [12]. However, the presence of excess oxide phases or large-sized particles (~20 nm) at

the grain boundaries could result in degradation of grain connectivity. For superconductivity, therefore, oxygen-rich secondary phases, especially MgO, will be of great importance and yield a positive or negative effect on the J_c . To study the effects

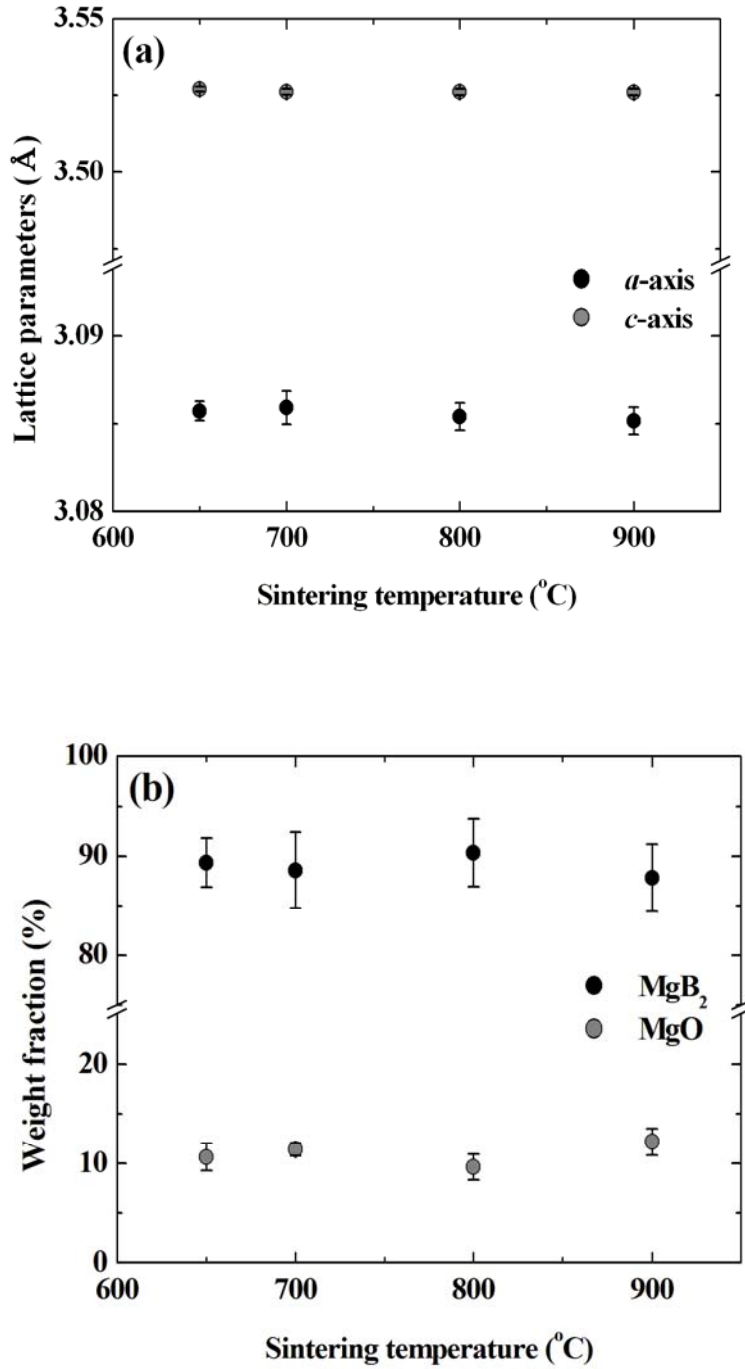
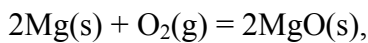


Figure 2.7 (a) Lattice parameters and (b) weight fractions of MgB₂ and MgO for samples made at different sintering temperatures [23].

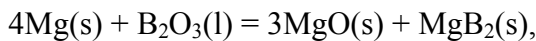
of MgO phase on the MgB₂ superconductivity, first, the fraction of MgO was calculated from the relative intensity of the (220) peak by using equation (2.1):

$$R_{MgO} (\%) = \frac{I_{MgO(220)}}{\sum I_{MgB_2(hkl)} + I_{MgO(220)}} \times 100 \quad (2.1)$$

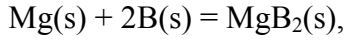
From equation (2.1), the calculated values were estimated to be 4.4%, 4.4%, 4.6%, 3.5%, and 4.6% for samples with sintering temperatures of 650°C, 700°C, 800°C, 900°C, and 1000°C, respectively [24]. Within the calculation error, these values were almost independent of the sintering temperature. This indicates that most MgO may be coming from the starting material. That is, Mg is a very active material that is very easy to oxidize in air. Formation possibilities for MgO within MgB₂ can be attributed to both of these factors: (i) A small amount of MgO is already present in the starting materials, because Mg can act as a potential oxygen (O) getter in air or be oxidised during sintering due to gaseous O. (ii) During sintering, existing B₂O₃ impurity in the B powder is in the liquid state due to its low melting point (~ 450°C), which allows it to react with Mg to form MgO. Based on this hypothesis, it can be proposed that the following reactions given by equations (4.2) - (4.4) may take place during the formation of MgB₂ phase [56, 57]:



$$\Delta G_1^0 = -1202460 + 215.18T \text{ (Jmol}^{-1}\text{)} \quad (2.2)$$



$$\Delta G_2^0 = -666940 + 123.19T \text{ (Jmol}^{-1}\text{)} \quad (2.3)$$



$$\Delta G_3^0 = -92050 + 10.64T \quad (\text{Jmol}^{-1}) \quad (2.4)$$

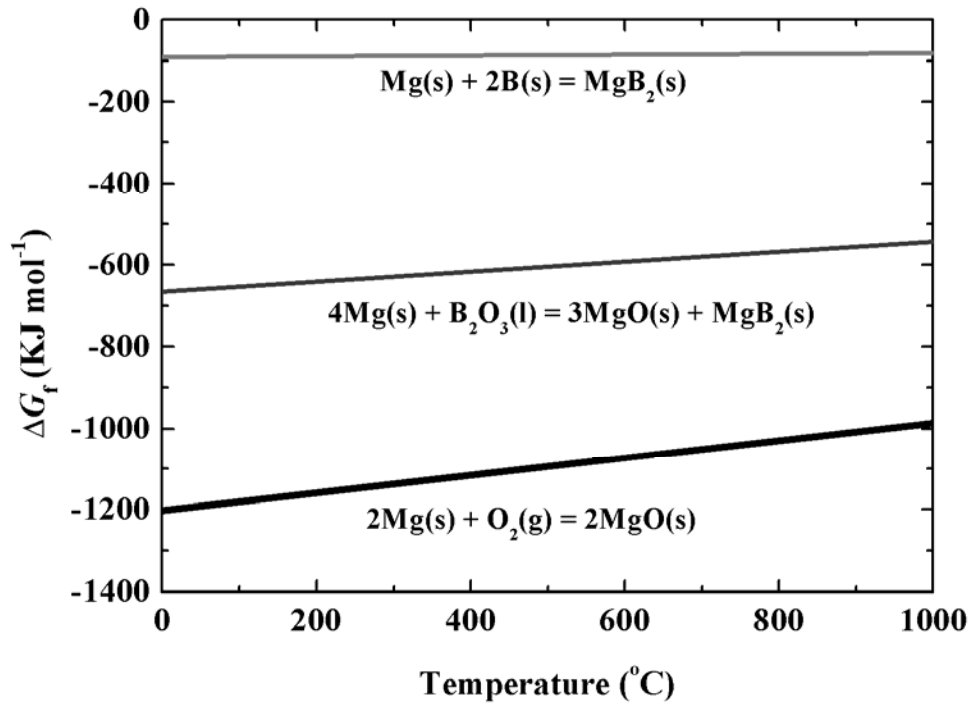


Figure 2.8 Standard Gibbs free energy (ΔG) of $2\text{Mg(s)} + \text{O}_2\text{(g)} = 2\text{MgO(s)}$; $4\text{Mg(s)} + \text{B}_2\text{O}_3\text{(l)} = 3\text{MgO(s)} + \text{MgB}_2\text{(s)}$; and $\text{Mg(s)} + 2\text{B(s)} = \text{MgB}_2\text{(s)}$ as a function of temperature.

where ΔG_i^0 ($i=1,2,3$) is the standard Gibbs free energy and T is the temperature. ΔG is a thermodynamic quantity which can be used to determine if a reaction is spontaneous or not. For example, a negative value for ΔG indicates that a reaction can proceed spontaneously without external inputs, while a positive value indicates that it will not. It can be clearly seen that ΔG of all the reactions has a negative value, which means that all reactions are theoretically possible from the thermodynamical point of view. However among them, ΔG_1^0 and ΔG_2^0 are more negative relative to ΔG_3^0 with temperature,

as can be seen in Figure 2.8, i.e., formation of MgO occurs more easily than that of MgB₂. It is expected that reaction (2) is responsible for the main oxidation product according to the above reaction equations. As a result, MgO formation could easily take place before MgB₂ is formed. Reducing exposure to O plays an important role in this system, because formation of the oxide phase can result in secondary phases.

2.2.6 Superconductivity and microstructures of MgB₂

From further Rietveld refinement, the grain size and lattice strain were also estimated for all samples [23]. The lattice strain versus average grain size (from measured results) as a function of sintering temperature is shown in Figure 2.9. It was observed that the full width at half maximum (FWHM) of the (110) peak decreased as the sintering temperature increased. The calculated values were 0.566°, 0.524°, 0.484°, 0.428°, and 0.376° for sintering temperatures of 650°C, 700°C, 800°C, 900°C, and 1000°C, respectively. This behaviour of the MgB₂ samples as a function of sintering temperature can be explained by the improvement of crystallinity with temperature, resulting in increasing grain size. Improvement of crystallinity is also associated with the grain connectivity of MgB₂ grains, resulting in increased density of the MgB₂. In order to confirm the effects of density, the geometric density was estimated for all samples. The corresponding values were 1.29gcm⁻³, 1.23gcm⁻³, 1.35gcm⁻³, 1.38gcm⁻³, and 1.40gcm⁻³, respectively. Even though these densities were not close to the theoretical density (2.62gcm⁻³) of pure MgB₂, as mentioned above, there was a small densification effect with increasing sintering temperature. As a result, MgO formation did not affect the lattice strain of the MgB₂ structure.

On the other hand, the degradation of crystallinity for MgB₂ can arise from a disordered crystal lattice, which is caused by various lattice defects associated with Mg deficiency

and intragranular precipitates such as secondary phases. In a recent publication, Yamamoto *et al.* [58] reported a correlation between the FWHM and H_{irr} in MgB_2 . The H_{irr} was enhanced by degradation of the FWHM of a sample, that is, a low temperature solid-solid reaction was effective for producing low crystallinity. In addition, Eom *et al.* [59] made a dirty film with $FWHM > 1^\circ$. They induced a larger FWHM to improve H_{c2} (~ 50 T). On the other hand, Lee *et al.* [60] reported that clean single crystals with $FWHM \approx 0.06^\circ$ had low H_{c2} (~ 20 T). These results indicate that degradation of crystallinity is a guiding principle for high H_{irr} . This is because a low sintering temperature can introduce a small average grain size, which could be act as a source of grain boundary pinning for MgB_2 superconductor.

Please see print copy for Figure 2.9

Figure 2.9 Lattice strain versus average grain size (from measured results) as a function of sintering temperature [23].

These observations can be further supported by the FEG-SEM images [23]. Figure 2.10 shows FEG-SEM images of the fractured core surface for samples sintered at 650°C, 800°C, and 1000°C. To obtain the images, the Fe sheath was removed by a mechanical method.

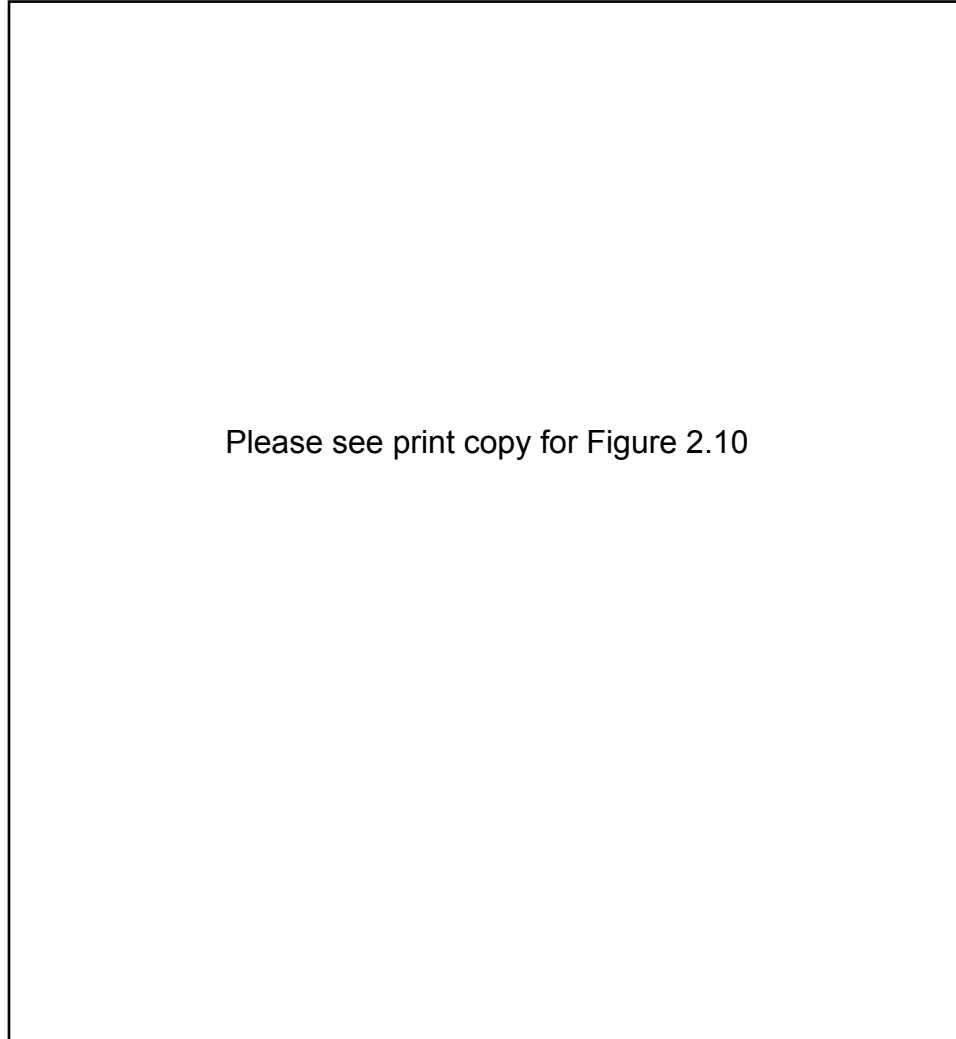


Figure 2.10 Field emission gun-scanning electron microscopy (FEG-SEM) images of core surface for samples sintered at 650°C ((a) and (b)), 800°C ((c) and (d)), and 1000°C ((e) and (d)) [24].

It was observed that the average grain size increased as the sintering temperature increased. The grain connectivity also became stronger as the sintering temperature increased. For example, the sample sintered at 650°C consisted of MgB_2 with 50 – 150 nm grains, while the sample sintered at 1000°C consisted of 1 – 3 μm grains. Specifically, the low sintering temperature sample, 650°C, seems to have a granular

microstructure. On the other hand, grains of the high sintering temperature sample (1000°C) have become inhomogeneous. This may be attributed to a reaction layer such as Fe_2B , which affects the chemical heterogeneity. In addition, this observation can be attributed to chemically sintered grain boundaries due to the high sintering temperature (Figure 2.10(f)).

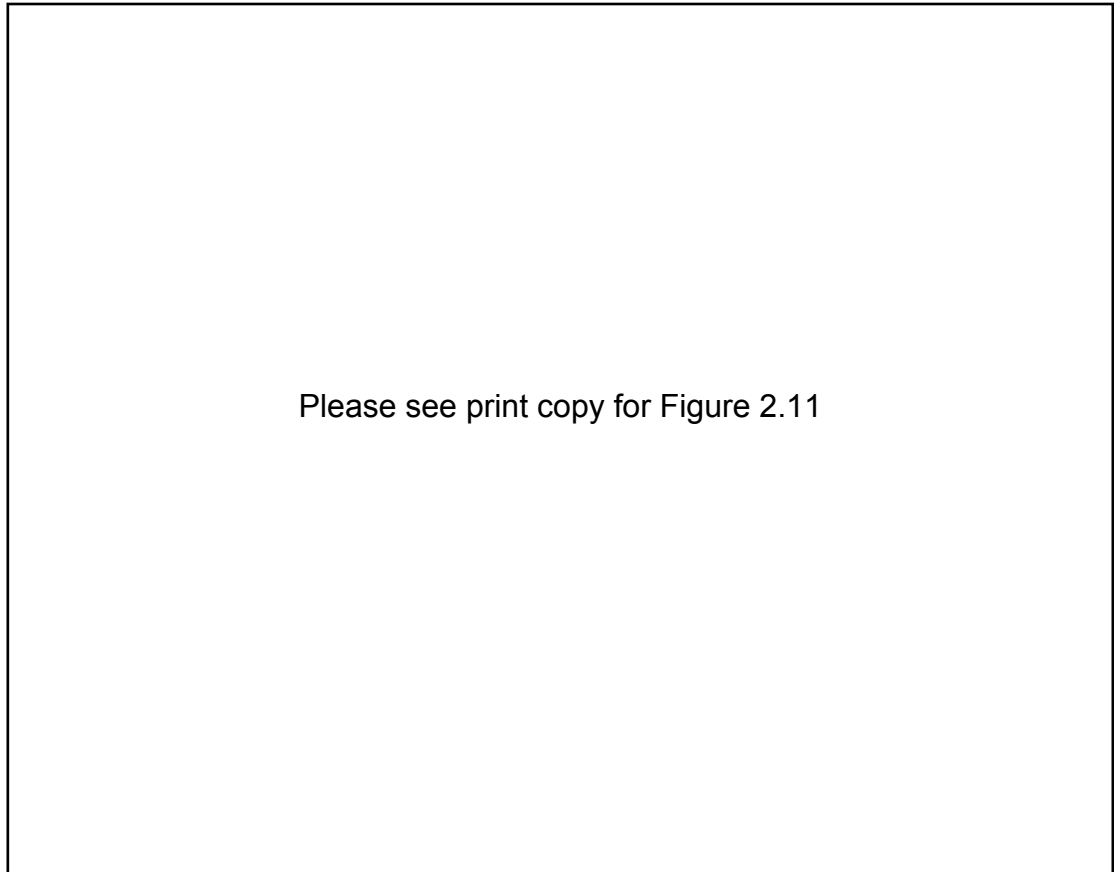


Figure 2.11 Critical current density (J_c) of all MgB_2/Fe wire samples at 4.2 K and 10 T. Magnetic fields were applied parallel to the wire axis of the MgB_2 wire. Inset shows the $J_c(B)$ of all samples as a function of sintering temperature [24].

Figure 2.11 shows the J_c of all the wire samples at 4.2 K and 10 T. Magnetic fields were applied perpendicular to the wire axis of the MgB_2 conductor [24]. It was observed that the $J_c(B)$ decreased with increasing sintering temperature. Specifically, the J_c of the sample sintered at 650°C for 30 min was estimated to be 4200 Acm^{-2} . Low J_c under high field despite good grain connectivity in the high sintering temperature sample is believed to be due to the large grains. From the results, grain boundaries for

MgB₂ could be acting as the predominant pinning centres, while grain growth corresponds to reduction of effective pinning. However, self-field J_c in the high sintering temperature sample should be better than that in the low sintering temperature sample. This is because the higher sintering temperature samples had better crystallinity and grain connectivity.

Please see print copy for Figure 2.12

Figure 2.12 Resistivity (ρ) of MgB₂/Fe wires as a function of temperature for three samples sintered at different temperatures. Transport measurements for ρ were done using a standard ac four probe method. The inset shows an enlargement of the temperature range around T_c [24].

Figure 2.12 shows the zero field resistivity (ρ) of MgB₂/Fe wires as a function of sintering temperature. To measure ρ , the Fe sheath material was removed. It was observed that the onset T_c dropped from 38.7 K to 37.3 K as the sintering temperature decreased. What is interesting is that ΔT_c for the sample sintered at 800°C is slightly smaller than that for the one sintered at 1000°C. This is because there was a reaction

layer of Fe₂B on the surface of the MgB₂ core as mentioned above. It should also be noted that the ΔT_c in all samples was less than 1 K. With increasing sintering temperature, the ΔT_c decreased, due to improvement of the interaction between grains. It is well known that the relatively low ρ near 300 K for samples sintered at high temperature may be related to higher density and better intergranular connection between grains. On the other hand, ρ behaviour near T_c is probably related to intragranular defects, because the phonon contribution to ρ decreases as the temperature decreases.

To further analyse intergranular connection, $\Delta\rho(\rho_{300\text{ K}} - \rho_{40\text{ K}})$ was calculated for all samples. The estimated values were 35.5 $\mu\Omega\cdot\text{cm}$, 29.1 $\mu\Omega\cdot\text{cm}$, and 34.5 $\mu\Omega\cdot\text{cm}$ for the 650°C, 800°C, and 1000°C samples, respectively. It is well known that a lower value of $\Delta\rho$ indicates good connectivity between grains [23]. Based on these results, large-sized grains with good connectivity due to grain growth are formed as the sintering temperature increases. However, this accompanies a decrease in the number of grains, resulting in depression of J_c . In addition, the residual resistivity ratio (RRR) defined by $\rho(300\text{ K})/\rho(40\text{ K})$ was also estimated. The corresponding RRR values were 1.85, 2.06, and 2.99, respectively. These had the same trends as $\Delta\rho$. It should be noted that if low sintering temperature samples show lack of crystallinity and grain connectivity, then J_c should be depressed. However, such a trend did not exist for these samples. Furthermore, even though density and T_c were also relatively lower, these samples had good J_c in the high field regime (Figure 2.11). Based on these results, improvement of J_c under high field is dominated by improvement of the grain boundary contribution. Small size grains can improve the effective pinning.

Please see print copy for Figure 2.13

Figure 2.13 FEG-SEM images of polished core surfaces for samples sintered at (a) 650°C, (b) 800°C, and (c) 1000°C [24].

Figure 2.13 shows field emission gun-SEM (FEG-SEM) images of polished core surfaces for samples sintered at 650°C, 800°C, and 1000°C. As can be seen in the images, connectivity between grains remained the same, regardless of sintering temperature. This phenomenon occurs because melted Mg at around 650°C starts to diffuse into solid amorphous B.

The temperature dependence of H_{irr} and H_{c2} for all un-doped samples sintered at temperatures from 650°C to 1000°C is shown in Figure 2.14. As can be seen in the figure, the values of H_{c2} and H_{irr} were depressed systematically as the sintering temperature increased to 1000°C. These properties showed the a same trends as $J_c(B)$. Again, this indicates that degradation of crystallinity is the guiding principle for high H_{irr} and H_{c2} . In addition, the $H_{c2}-T$ curves of all samples show similar behaviour to those of $H_{irr}-T$. For example, the curves showed a positive curvature very near T_c ,

while the curve was linear except for this region. The positive curvature of H_{c2} at $T \approx T_c$ indicates that the diffusivity in the σ bands is suppressed compared to that in the π bands [61].

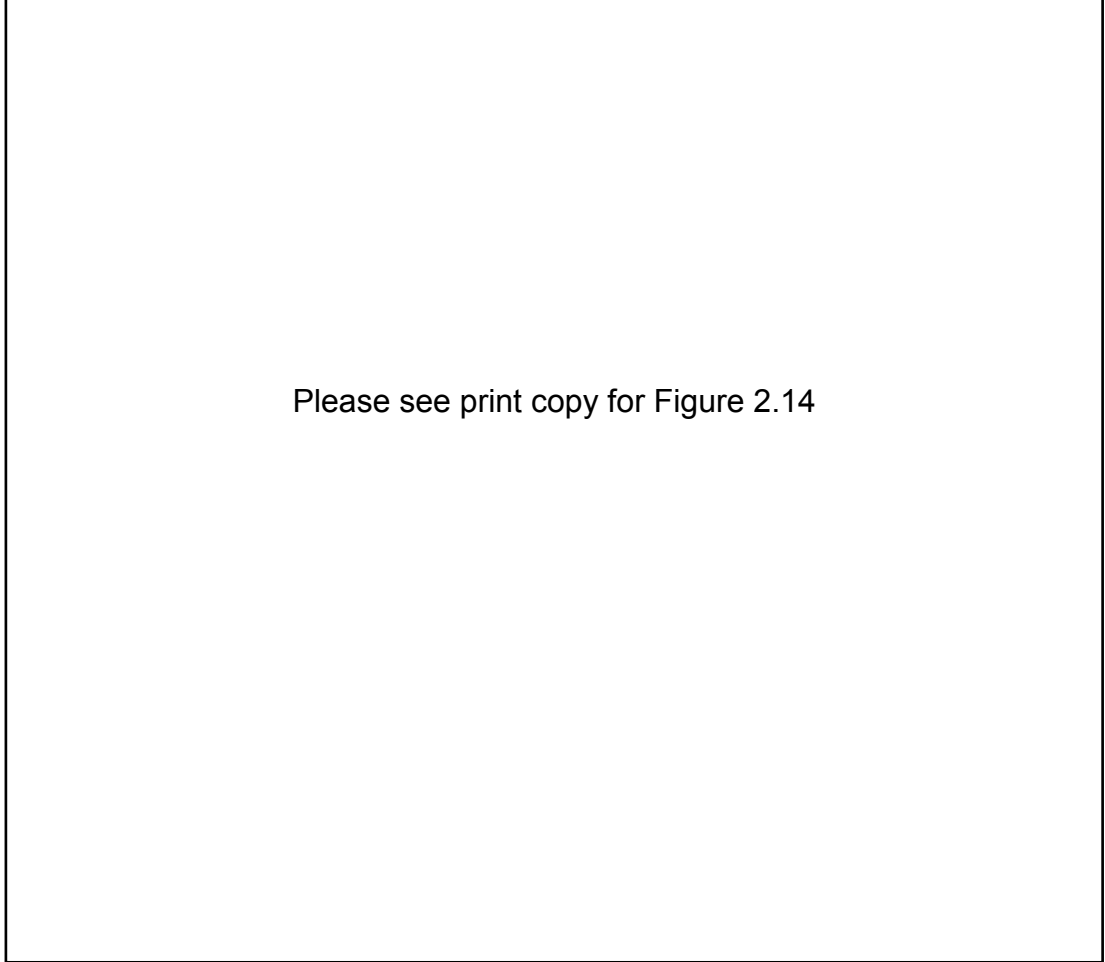


Figure 2.14 Temperature dependence of irreversibility field (H_{irr}) and upper critical field (H_{c2}) for MgB_2/Fe wires sintered at various sintering temperatures for 30 min [24].

2.2.7 Comparison between wire and tape

Figure 2.15(a) shows transport J_c for round wires and flat tapes at 4.2 K. The inset to the figure shows the J_c behaviour of reference wire samples at 4.2 K and 10 T as a function of sintering temperature. It can be observed that the $J_c(B)$ for pristine MgB_2 wire decreased with increasing sintering temperature up to 1000°C. From previous works [23, 24, 42], this is because grain boundaries for MgB_2 could be acting as the predominant pinning centres, while grain growth corresponds to reduction of effective pinning. For

example, J_c of the sample sintered at 650°C for 30 min was estimated to be 4200 Acm⁻² at 4.2 K and 10 T, while the corresponding value for the sample sintered at 1000°C for 30 min was 630 Acm⁻². This is why all samples were sintered at lower sintering temperature up to 700°C in further work. As can be seen in the figure, both round wire and flat tape samples sintered at 650°C showed a better, higher J_c at 4.2 K and 12 T. This can be attributed to the grain boundary pinning due to smaller grain size, as mentioned above. Interestingly, J_c values (1130 Acm⁻²) of round wires were slightly higher than those (880 Acm⁻²) of flat tape under the same conditions of 4.2 K and 12 T. On the other hand, J_c values at 7 T for flat tapes were similar to those for round wires. J_c values for round wire and flat tape were 26800 Acm⁻² and 27800 Acm⁻², respectively at 4.2 K and 7 T. This indicates that there is still much room to increase J_c at lower field. In the measurements, the magnetic field is all parallel to tape length direction. That is, the flat tape can achieve significantly higher J_c values in the low field regime compared to round wire, mostly as a consequence of the higher deformation pressure of the rollers in comparison to drawing.

These observations can be further supported by the Kramer plot (F_K), as can be seen in Figure 2.15(b). Pinning force strength, $J_c^{1/2}B^{1/4}$, is expected to be a linear function of magnetic field (B). The characteristic irreversibility field, at which extrapolated F_K reaches zero, was 15.2 T and 14.7 T, respectively, for round wire and flat tape. However, the F_K is not really linear, in particular at low J_c , where it is observed to have a curvature. This is might be due to percolation paths, which in fact give a transport J_c that is always lower than the value extracted from magnetic loops [62].

Please see print copy for Figure 2.15

Figure 2.15 (a) Transport J_c for round wires and flat tapes at 4.2 K. Inset figure shows the J_c behaviour of referenced wire samples at 4.2 K and 10 T as a function of sintering temperature. (b) Kramer plot (F_K), $J_c^{1/2} \times B^{1/4}$ vs. B , for round wires and flat tapes at 4.2 K [23].



Please see print copy for Figure 2.16

Figure 2.16 SEM images of polished cross-sections for round wire ((a) and (b)) and flat tape ((c) and (d)) [64].

Figure 2.16 shows the SEM images of polished cross-sections for round wire ((a) and (b)) and flat tape ((c) and (d)) [64]. In the case of both samples, it was observed that there was considerable porosity. This normal phenomenon occurs when melted Mg at around 650°C starts to diffuse into solid amorphous B. That is to say, the theoretical volume of the Mg and B powders is larger than the volume of the reacted MgB_2 . Volatile Mg during sintering can also be responsible for volume shrinkage and porosity. So an excess amount of Mg is often provided to compensate for Mg losses during sintering of *in situ* processed material. In the flat tape, the relative amount of porosity decreased due to the rolling load, which resulted in an increase in the core densification, even under the same sintering conditions. As a result, it was speculated that the rolling further promoted the grain connectivity, due to the high pressure applied to the sample and, thus, resulted in a high J_c . However, a too large reduction can result in an

inhomogeneous deformation. Therefore, the mechanical deformation should be optimised by considering the pressure effects, thickness effects, and sausage effects. Recently, Yamada *et al.* reported that flat tape prepared by hot pressing was significantly improved [63]. The higher J_c in hot pressed tapes results from the improvement due to denser MgB_2 structures with fewer voids and better linkage among grains.

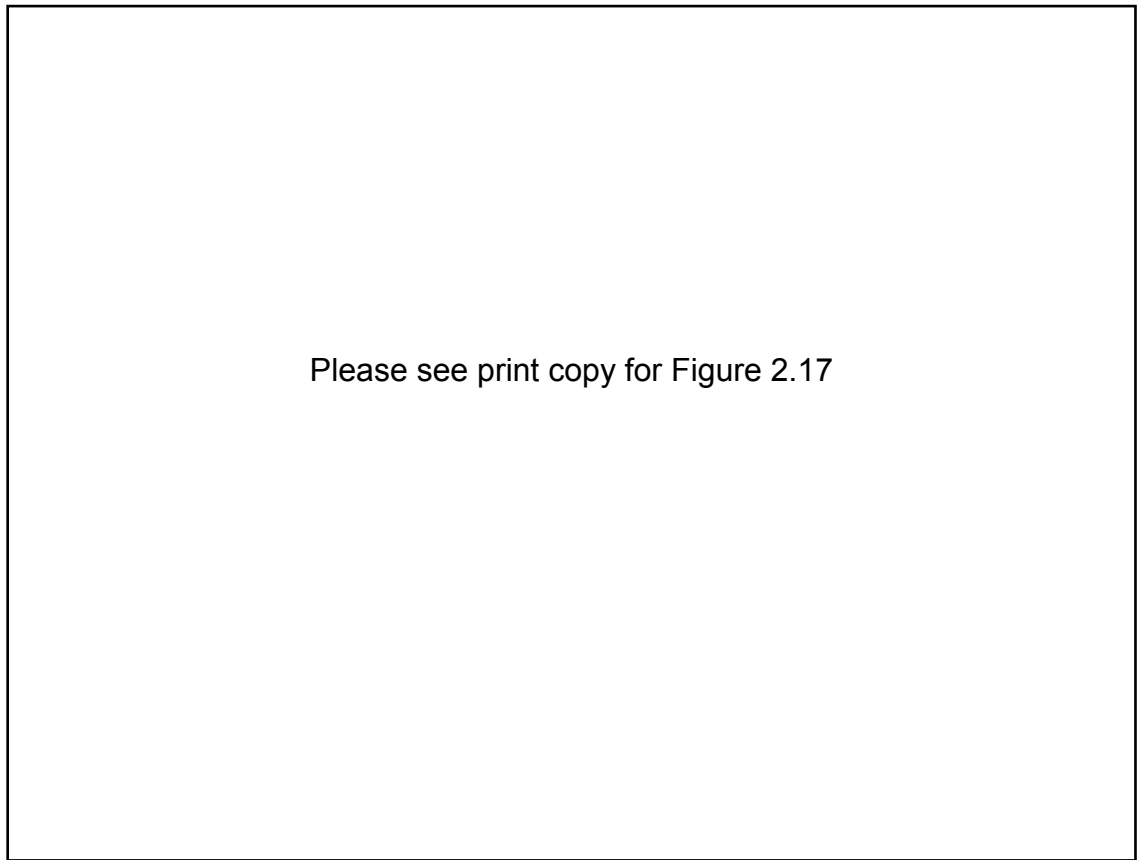


Figure 2.17 SEM image of cross-section of a flat tape. There were cracks in the middle of the core (indicated by white arrows) [64].

Figure 2.17 shows an SEM image of a cross-section of flat tape. As can be seen in the figure, the interface between the Fe sheath and the MgB_2 core appears dense, but on the other hand, there is considerable porosity in the central area. The densification is due to the hardness of the Fe sheath. It should be noted that there were no reaction layers between the MgB_2 core and the Fe sheath because of the low sintering temperature of 650°C . Sheath materials such as Fe are found to be less reactive with B, compared to

copper (Cu) and aluminium (Al). However, there were micro- and macro-cracks in the middle of the core (indicated by white arrows). This can be attributed to the high ratio of thickness reduction. According to our experimental conditions, the thickness of flat tapes was decreased by a thickness reduction of 0.1 mm, from 1.4 mm to 0.5 mm.

2.2.8 Comparison between *in situ* and *ex situ* processing

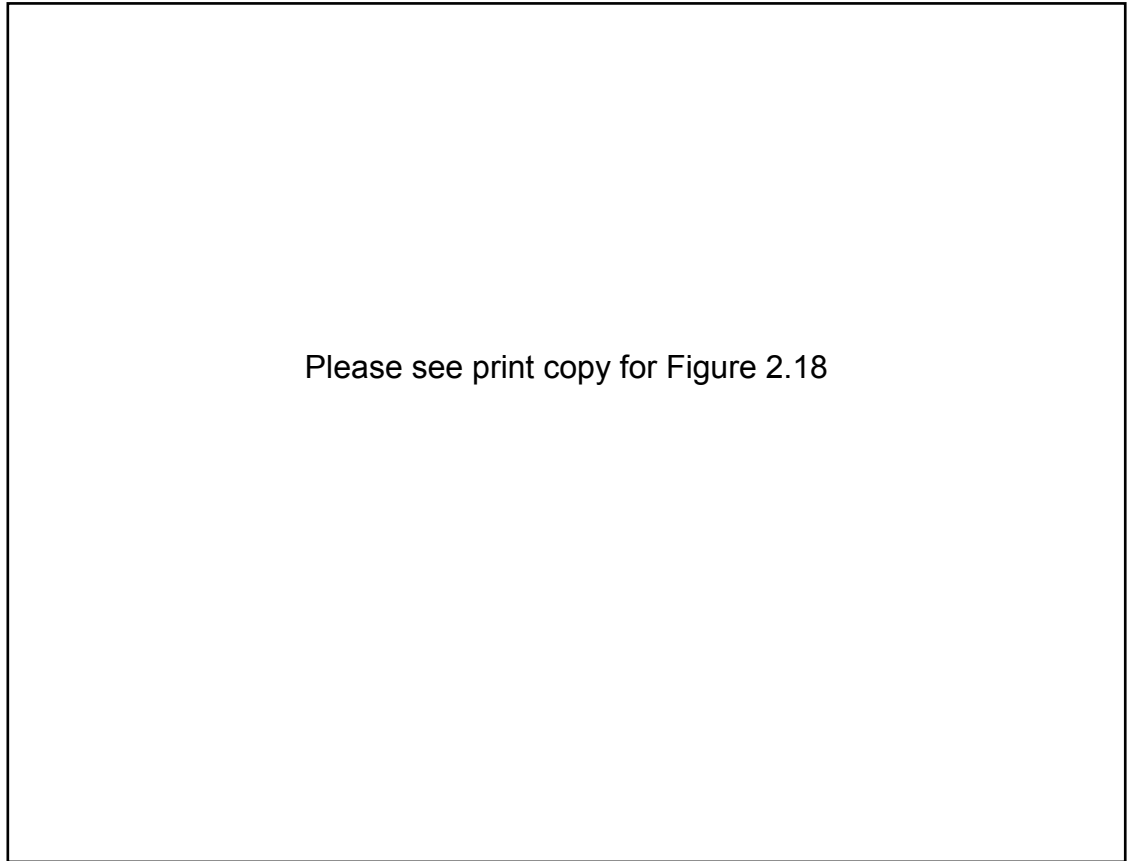


Figure 2.18 $J_c(B)$ behaviour of *in situ* processed flat tape compared to commercial and modified *ex situ* processed flat tapes [64].

Figure 2.18 plots the $J_c(B)$ behaviour of *in situ* processed flat tape compared to commercial and modified *ex situ* processed flat tapes. It was observed that J_c for *in situ* tape was significantly higher than for commercial *ex situ* tapes in both the low and high field regimes. The main reason is because *in situ* processing can introduce better connectivity and smaller grains. The smaller grains could be acting as strong flux pinning centres under high field. Recently, Nakane *et al.* reported that J_c of a modified *ex situ* tape reached 3600 Acm^{-2} at 4.2 K and 10 T [64]. This result is very comparable

with *in situ* samples. Note that self-field J_c of both *ex situ* processed flat tapes showed poor values in the low field regime, even though the high field J_c of the modified *ex situ* tape showed significant enhancement. This is expected, showing the need for improvement in connectivity. However, the results show a potential way to enhance pinning. It is expected that J_c can be further improved by better connectivity through optimizing the fabrication procedures and sintering conditions.

2.3 Effect of Boron powder purity on MgB₂

2.3.1 Characteristics of Boron (B)

Boron is a chemical element with atomic number 5 and the chemical symbol B. Boron is never found as a free element in nature. Several allotropes of boron exist: amorphous boron is a brown powder, though crystalline boron is black, hard, and a weak conductor at room temperature. Boron compounds play important roles as light structural materials, non-toxic insecticides and preservatives, and reagents for chemical synthesis. Brown amorphous boron is a product of certain chemical reactions. It contains boron atoms randomly bonded to each other without long range order. Crystalline boron, a very hard black material with a high melting point (2076 °C), exists in many polymorphs. Also, boron is the least electronegative non-metal, meaning that it is usually oxidized (loses electrons) in reactions. Boron is also similar to carbon in its capability to form stable covalently bonded molecular networks. Pure elemental boron is not easy to prepare. The earliest methods used involve reduction of boric oxide with metals such as magnesium. However the product is almost always contaminated with metal borides [94].

2.3.2 Market trends

Estimated global consumption of boron rose to a record 1.8 million tones of B₂O₃ in 2005 following a period of strong growth in demand from Asia, Europe, and North America. Boron mining and refining capacities are considered to be adequate to meet expected levels of growth through the next decade.

Chinese boron producers have been unable to meet rapidly growing demand for high quality borates. In particular, pure (99%) amorphous boron powder is about 10 times more expensive than the low-grade (96%, 92%) amorphous powders.

Roskill Consulting Group has forecast that world demand for boron will grow by 3.4% per year to reach 21 million tones by 2010. The highest growth in demand is expected to be in Asia where demand could rise by an average 5.7% per year [95].

2.3.3 Influence of Boron Precursor Powders

In 2005, C. K. Chen [67] studied the influence of the nature of the boron precursor on the superconducting properties of polycrystalline MgB_2 .

Table 2.1 presents the properties of four boron precursor powders: the crystalline boron contains large particles tens of microns in size, whereas the amorphous powders have particle sizes of $\sim 0.5 \mu\text{m}$. The reactivity of the amorphous powders is much greater than that of the crystalline powders, and the reduced particle size further enhances the reaction rate.

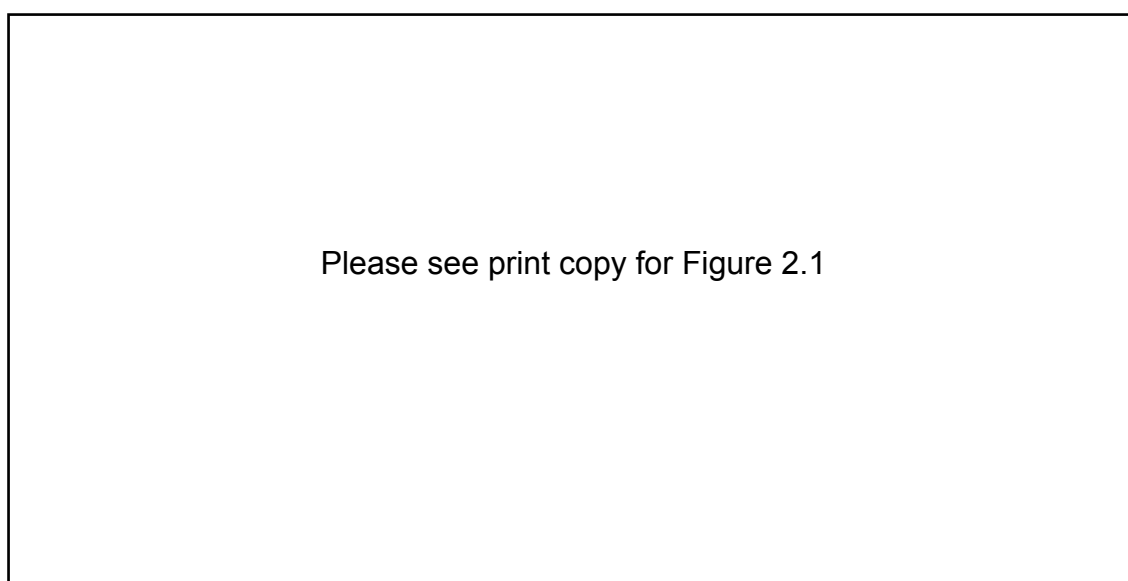


Table 2.1 Source, form, and purity of the different boron powders with their particle size distribution [67].

Typical SEM images of samples of the four different powders are shown in Figure 2.19. The larger grains of the crystalline samples (few hundred nm in size) compared to the amorphous samples (~100 nm and less) are consistent with the measured particle sizes of the precursor boron powders of Table 2.1. The A9999 sample had the finest and most uniform grain size.

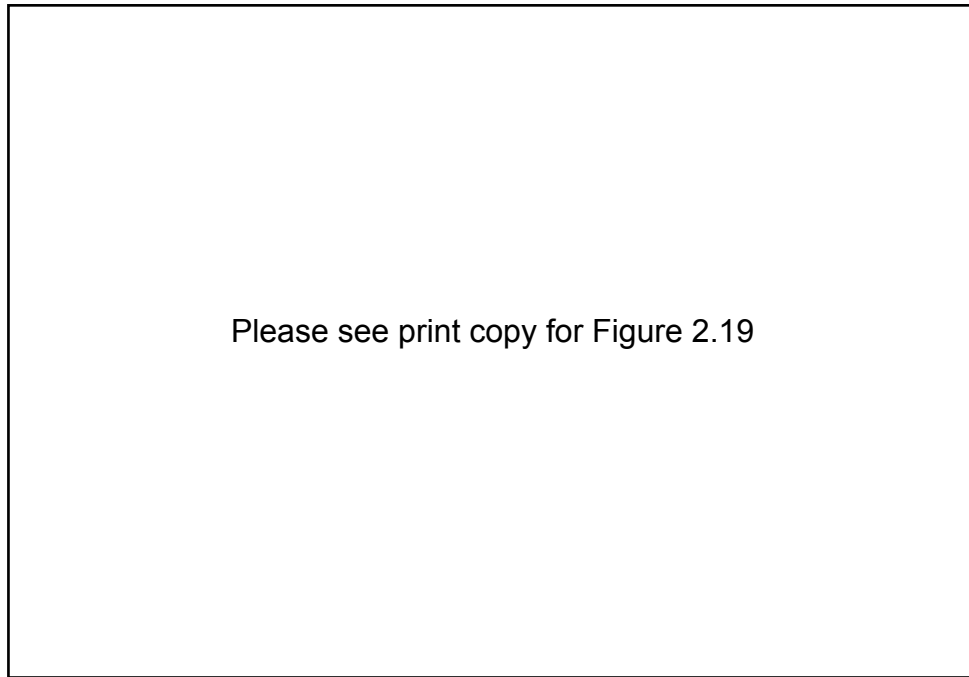


Figure 2.19 FEG-SEM images of samples (a) C98, (b) C99, (c) A9597, and (d) A9999 [67].

The critical current densities (J_c) for MgB_2 made from high purity amorphous boron are at least a factor of three higher than typical values measured for standard MgB_2 samples made from amorphous precursors. This is shown in Figure 2.20. Samples made from crystalline boron precursors contain more oxide impurities, and the $J_c(H)$ behavior can be explained in terms of a reduced effective cross-sectional area.

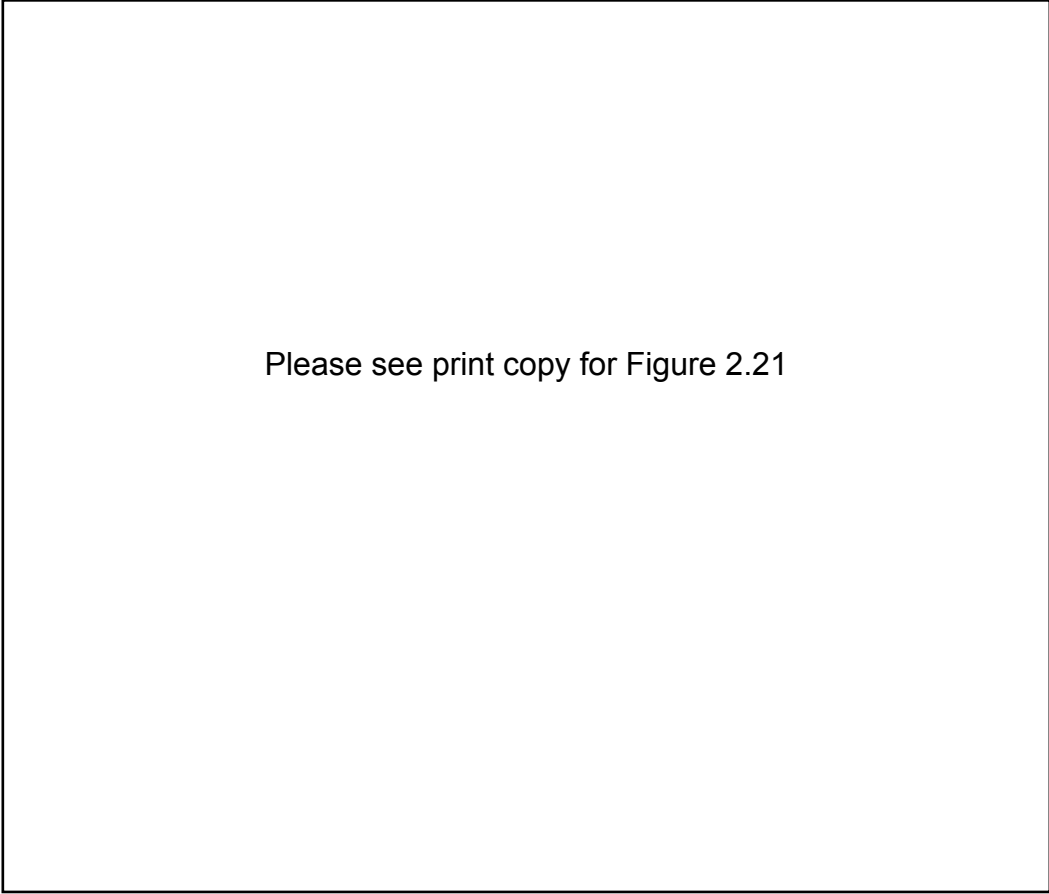
Please see print copy for Figure 2.20

Figure 2.20 Magnetic critical current densities versus applied magnetic field at 6 K and 20 K [67].

2.3.4 Purification of low-grade boron powders -- acid leaching process

Dou's group tried to purify the low-grade boron powders using an acid leaching process, to study the effects of boron powder purity and process parameters on the superconducting properties of MgB_2 . They also investigated the effects of intrinsic impurities in MgB_2 on the superconducting properties, which will open another window to investigate the doping process for MgB_2 [68].

A mixture of 5 g low-grade boron powder and 10 mL ethanol was ball milled in a tungsten carbide jar for 30 mins, put into the solution of concentrated hydrochloric acid (50 mL) and de-ionised (DI) water (50 mL) for 60 mins, and boiled slowly on a hotplate with magnetic stirring, then cooled to room temperature. The sample was filtered in a centrifugal separator, washed in DI water with a swing motor and filtered again with the centrifugal separator; finally, the sample was dried in a vacuum furnace at 110°C for 12 hours. The procedure is shown in Figure 2.21. Boron powders of different purities (amorphous, irregular shaped, 99%, 96%, 92%) and purified (96%, 92%) boron powders made by a simple chemical process were characterised by [Scanning Electron Microscopy](#) (SEM), and Brunauer Emmett Teller (BET) methods. MgB₂ samples were prepared by reacting Mg and B by solid state reaction, using crystalline magnesium powder (99.8%, 325 mesh) and five different types of boron powders (pure 99%, original 96%, original 92%, purified 96%, purified 92%, with the MgB₂ samples named after these abbreviations). Mg and B were mixed in the atomic ratio of 1:2, followed by hand milling (above 30 minutes). The mixture powder was then pressed into pellets about 13 mm in diameter and 3 mm in thickness using a hydraulic press with an applied load of 8 tones. The pellets were placed inside a tube furnace and sintered at different temperatures (700 °C for 30 minutes, 3 hours, 6 hours, 825 °C for 30 minutes, 3 hours, respectively) under the protection of a high purity argon atmosphere. The heating rate was 10 °C/min, with natural cooling down to room temperature.



Please see print copy for Figure 2.21

Figure 2.21 Acid leaching process [68].

The pellets were cut into small bar shaped pieces with dimensions of $2 \times 2 \times 3 \text{ mm}^3$. X-ray diffraction patterns in the $\theta - 2\theta$ step-scanning mode with 0.02° increments, 2 degrees/min, were recorded in a Philips PW1730 diffractometer with a $\text{Cu-K}\alpha$ radiation source. In order to observe uniformity of grain size, SEM images were collected. The superconducting transition temperature (T_c) was obtained using a commercial Quantum Design Magnetic Properties Measurement System (MPMS) by first cooling the sample in zero field and then measuring the magnetic moment as the sample was warmed up in field. Magnetization hysteresis loops were collected on a commercial Quantum Design Physical Properties Measurement System (PPMS) with the magnetic field applied parallel to the longest dimension of the sample. Magnetic critical current density J_c was estimated based on Bean's model.

It can be seen that after leaching, the purity of the 92% boron was increased to above 95%, while the purity of the 96% powder was only slightly increased to 96.6%. As the oxygen impurities are mainly from B_2O_3 in the starting powders, that means B_2O_3 can be removed by ethanol.

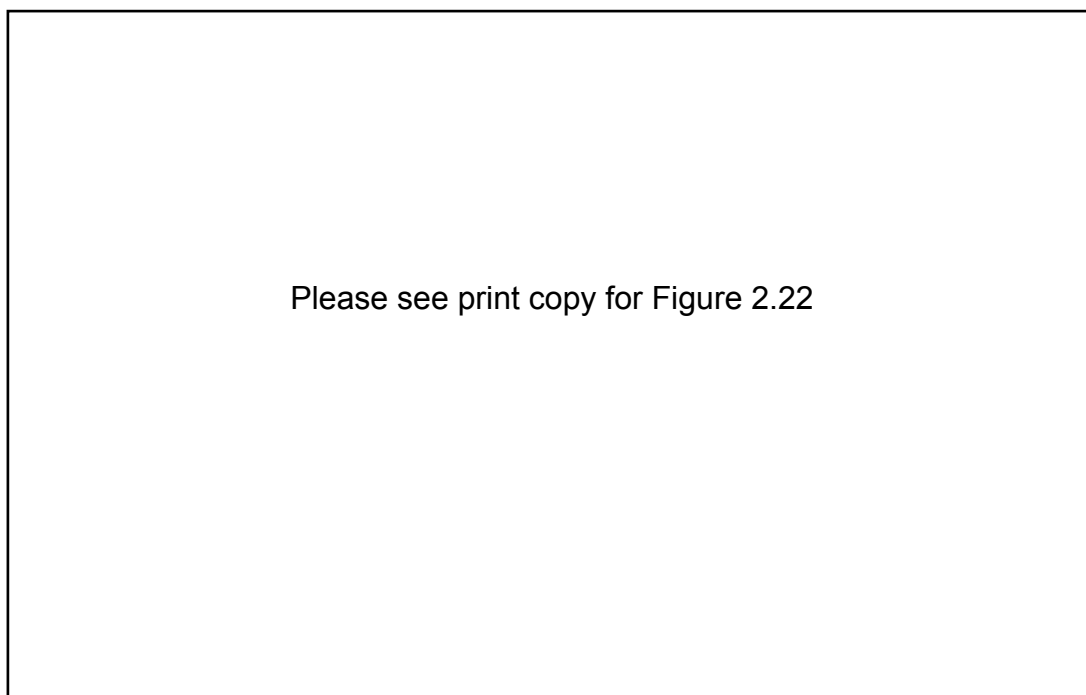


Figure 2.22 BET results for different B powders [68].

Figure 2.22 shows the BET results for the specific surface areas of different B powders. The 99% B powder has a very high specific surface area ($31.5\text{m}^2/\text{g}$). The leaching process shows little effect on the specific surface area (from $12.94\text{ m}^2/\text{g}$ to $13.51\text{ m}^2/\text{g}$, and from $10.84\text{ m}^2/\text{g}$ to $10.44\text{ m}^2/\text{g}$ for the 92% and the 96% boron, respectively).

SEM images for the powders are shown in Figure 2.23. As can be seen from the pictures, the 99% boron powders show smaller grain size and better grain homogeneity than the impure and purified powders. The particle sizes of 92% and 96% boron powders are not changed by the leaching process.

Please see print copy for Figure 2.23

Figure 2.23 SEM images of different Boron powders [68]

Please see print copy for Figure 2.24a

Figure 2.24a X-ray powder diffraction patterns of MgB_2 samples made from pure 99% B powder [68]

Please see print copy for Figure 2.24b

Figure 2.24b X-ray powder diffraction patterns of MgB₂ samples made from 96% B powder [68]

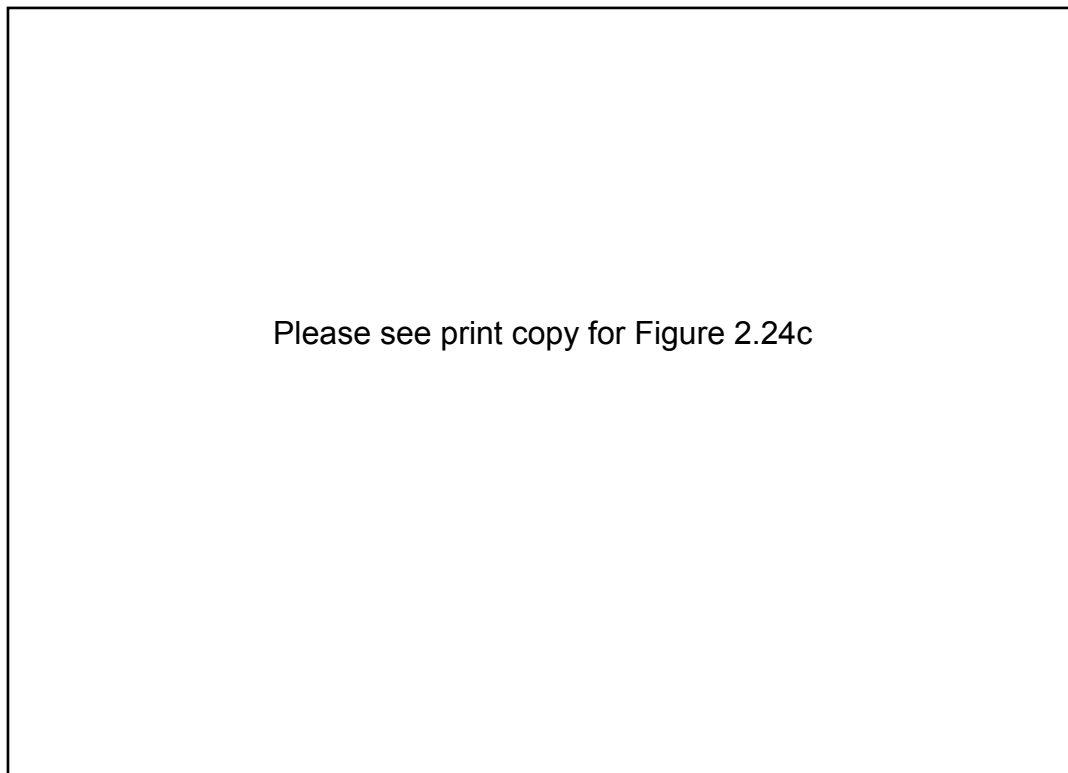


Figure 2.24c X-ray powder diffraction patterns of MgB₂ samples made from purified 92% B powder [68]

The X-ray diffraction patterns for MgB₂ samples sintered under different conditions from 99%, 96% and purified 92% starting boron powders are shown in Figure 2.23(a), (b), and (c), respectively. As can be seen from Figure 2.23(a), no remnant Mg is observed for the 99% samples sintered at 700 °C for only 30 minutes, indicating that the boron powder has reacted completely with Mg. However, for the purified samples, remnant Mg is always observed. The diffraction peak of MgO is higher for the longer sintering time, this is because the argon protective atmosphere is not kept pure enough for the longer sintering time, so the longer the sintering time, the higher the risk of oxidation, which is in agreement with the reported results [67].

Figure 2.25 contains $J_c(H)$ curves for the MgB_2 samples (original 96%, purified 96%, purified 92%, and pure 99%). It can be seen from the figure that the purifying process has a strong effect on the superconducting properties of MgB_2 superconductors. At 20K, compared to the original 96% sample, the purified 96% sample shows enhanced $J_c(H)$ performance at high field close to the irreversibility field, and the irreversibility field is increased from 4.1 T to 4.8 T (using $J_c = 100 \text{ A/cm}^2$ as the criterion for the irreversibility field). What is more interesting is the result on the purified 92% sample, as its critical current density is much better than that of the purified 96% sample. The reason is probably that the grain homogeneity of the purified 96% is not as good as that of the purified 92% sample, as can be seen from the SEM images shown in Figure 2.23. The critical current density of the purified 92% sample is even better than that of the pure 99% sample at high field close to the irreversibility field, and therefore results in a slightly increased irreversibility field.

Compared to the pure 99% sample, the J_c of the purified 92% sample decreases somewhat more slowly with increasing magnetic field, indicating that some of the remaining impurities in the purified 92% sample might be acting as pinning centers. However, over the wide magnetic field range below 4.5 T, the critical current density of the purified 92% sample is obviously lower than that of the pure 99% sample. From the XRD, SEM, and BET results, it can be seen that the purified powder still demonstrates more oxide impurities, lower surface reactivity, less uniform grain distributions, and larger grain size.

Please see print copy for Figure 2.25

Figure 2.25 J_c of samples made from different B powders [68].

2.3.5 Mechanical alloying effect on MgB₂

The effect of the initial powder particle size on the transport J_c values of ex situ MgB₂ tapes was first studied by Suo et al. [69], who reduced the average size by ball milling. The commercial MgB₂ powder, of a purity of 98%, was furnished by Alfa-Aesar and contained a large number of agglomerated grains, with a wide size distribution centred at around 60 μm . The original MgB₂ powder particles were submitted to ball milling using an agate mortar and agate balls, varying both milling time and energy, in order to obtain different particle sizes and to study their influence on J_c . Ball milling times from 2 to 100 h were chosen, thus yielding the particle sizes represented in Fig. 2.26. The various powder sizes in this figure are the peak values in the size distribution obtained by granulometry. For distinction, the powder (a), milled for 2 h, will be denoted as 3/30 μm and similarly, powder (b), (c) and (d) milled 3, 14 and 100 h, respectively, will be called 1.5/10 μm , 1/7 μm and 1 μm .

Please see print copy for Figure 2.26

Figure 2.26 Granulometry for different ball milled MgB_2 powders: (a) 2 h, distribution peaks 3/30 μm ; (b) 3 h, distribution peaks 1.5/10 μm ; (c) 14 h, distribution peaks 1/7 μm ; and (d) 100 h, distribution peak 1 μm [69].

Fig. 2.27 presents the J_c values for tapes based on the powders (a)–(d) as well as for the as-purchased powder after annealing at 950 °C. The tape with powder (a) 3/30 μm was found to exhibit the highest J_c value at 4.2 K (104 A/cm² at 6.5 T), which extrapolates to values close to 1 MA/cm² for B(0). With further reduction of the particle size, J_c decreases again; the lowest J_c values being observed in the tape fabricated using the finest powder particles (d), of size 1 μm . The particle size reduction by ball milling first causes an enhancement of J_c and H_{irr} (Fig. 2.28) up to a maximum value (3/30 μm particle size), followed by a decrease for the finest powders. The decrease of J_c for the latter is attributed to impurities diffusing at the grain surfaces. The powders with the smallest particle sizes are ball milled for much longer times, thus enhancing the chances of absorption of impurities at the grain surfaces. Milling must be performed under wet conditions, in order to avoid particle agglomeration. So far, no way has been found to perform the drying process under sufficiently clean conditions, in order to avoid the

impurities that affect the grain boundaries during the subsequent heat treatment, and contribute to a lowering of J_c . It follows that an improvement of the drying process is required for a further optimization of J_c for ex situ as well as for in situ MgB_2 tapes.

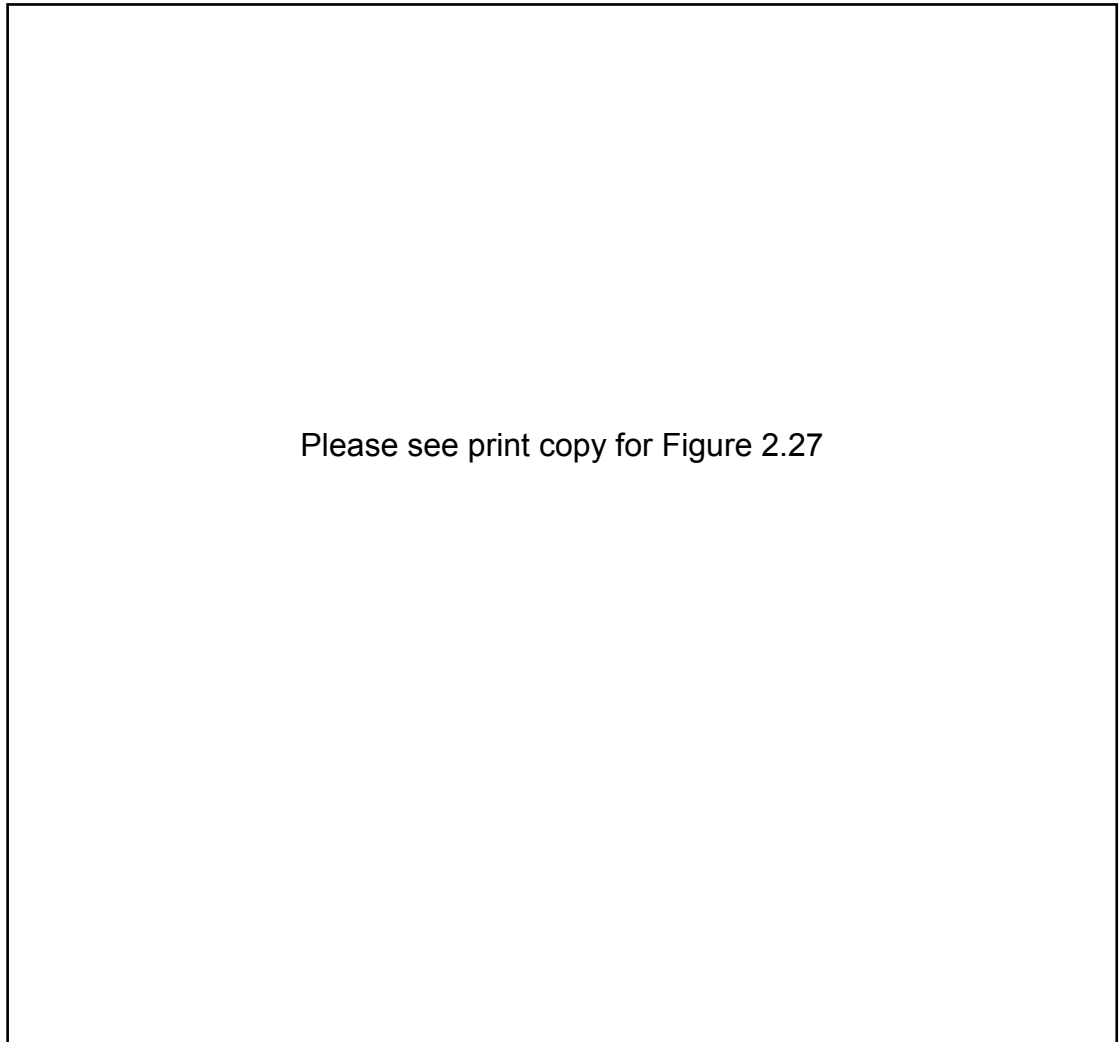


Figure 2.27 Transport and inductive measurements of the irreversibility field H_{irr} , for MgB_2/Fe tapes prepared with commercial and ball milled powders[69].

The Häbeler group investigated the influence of the quality of the boron precursor powder on the microstructure and superconducting properties of MgB_2 bulk samples and tapes [70].

Please see print copy for Table 2.2

Table 2.2 Nominal purity, impurities, grain size, and crystallinity of boron precursor powders from different suppliers [70].

They determined the impurities, the grain size and the crystallinity, in comparison with the nominal purity specified by the suppliers, of three different boron precursor powders B-a to B-c, as summarized in Table 2.2. Mg is the most frequent impurity, probably in the form of MgO, followed by alkalis and alkaline earth metals such as Na, K, Ca, and Si. Oxygen and carbon were found to be the main non-metallic impurities. The oxygen content of the boron precursor powder with the highest nominal purity, B-a, is higher than in B-c, which has a nominal purity of only 95–97%. It is very important that the non-metallic impurities are also taken into account to correctly correlate the precursor powder purity with the material properties.

The grain sizes of the boron precursor powders were estimated from the SEM images and confirmed by TEM imaging and EDX microanalysis in SEM. TEM was used to qualitatively identify the impurities in the boron powders. Mainly Mg and O, but also some K, Ca, and F impurities, were detected in the nanocrystalline grains. Relatively fewer impurities were found in the crystalline grains.

Bulk samples S-a, S-b, and S-c were prepared using different mechanically alloyed powders by hot pressing at 700°C and 640 MPa for 10 min. During hot pressing, Mg

and B nearly completely reacted to form MgB_2 , which was sintered to about 90% of the theoretical density. A comparison of the microstructure and superconducting properties of these samples is given in Table 2.3. The grain size in the MgB_2 bulk samples was found to be small because of the mechanical alloying. The bulk samples prepared from B-a contain the largest MgB_2 phase fraction and show the highest J_c of $4.7 \times 10^5 \text{ A cm}^{-2}$ at 20 K and 1 T. Boron precursor powders like B-a, with smaller grain size and fewer metallic impurities, are the most appropriate for the synthesis of bulk MgB_2 samples by hot pressing.

Please see print copy for Table 2.3

Table 2.3 Synthesis parameters, structural analysis by x-ray diffraction, microstructure analysis by SEM-EDX and superconducting properties of hot pressed bulk samples [70].

As the first step of the PIT-processing of tapes, rods of the precursor powder were prepared by cold isostatic pressing at 350 MPa. The rods were placed inside Fe tubes

with 10 mm outer and 6 mm inner diameter, which were deformed by shape rolling, drawing, and flat rolling to mono-filamentary tapes of about 0.35 mm thickness and 3.5 mm width. The tapes, which were embedded in an oxygen gettering foil, were heat treated at temperatures between 500 and 650°C for 3 h under Ar atmosphere.

Please see print copy for Table 2.4	
-------------------------------------	--

Table 2.4 Synthesis parameters, microstructure analysis by SEM-EDX and superconducting properties of tapes [70].

The differences in the microstructure and the superconducting properties of the tapes are summarized in Table 2.5. The enhanced J_c of $5.0 \times 10^4 \text{ A cm}^{-2}$ (at 20 K, 3 T) of the tapes investigated in this work was significantly higher and highlights the benefits of mechanical alloying for enhancing the J_c of MgB_2 superconductors. The main advantage is the higher reactivity, because compact tapes can be formed at about 500 °C. However, oxygen is introduced during synthesis of tapes, resulting in a significantly reduced T_c .

In 2008, the Häbler group further improved the the critical current density of MgB_2 tapes with nanocarbon-doped mechanically alloyed (MA) precursor [97], and the J_c results are shown in Figure 2.28. The dependence of the critical current density on the

parallel field was significantly higher at 4.2 K. The highest values were found for tapes annealed at 625°C for 3 hours in Ar, with $J_c \approx 10^4 \text{ A cm}^{-2}$ at 16.4 T and 4.2 K.

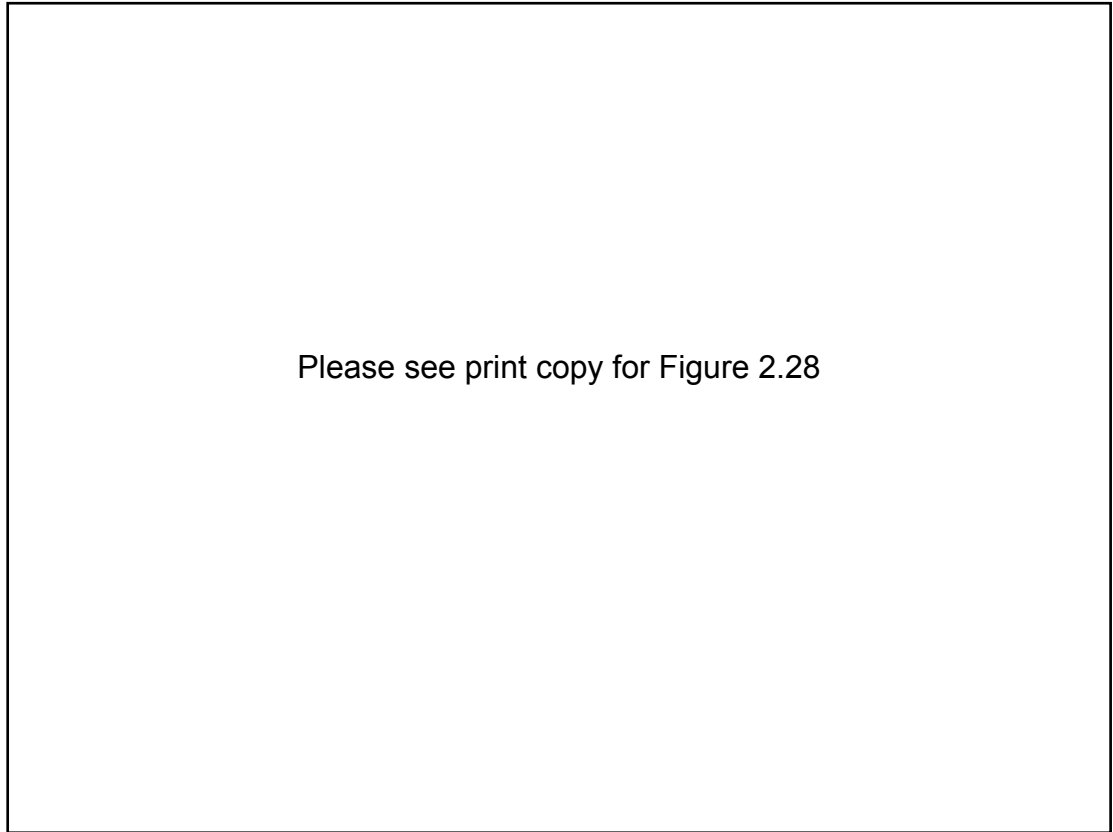


Figure 2.28 Dependence of the critical current density on the parallel field for CuNi/Nb double-sheathed tapes with nanocarbon-doped MA precursor annealed at different temperatures [97].

2.4 Effects of Mg Precursor Powder on MgB₂ Superconductivity

It is well known that Mg is highly volatile at high temperatures. Therefore, Mg is easily lost during the preparation of samples. As a result, prepared MgB₂ samples usually show Mg deficiency. Mg powder has a large surface area, and it oxidizes easily during the powder preparation processing. The effects of MgO on MgB₂ superconducting properties should be studied to facilitate the production of MgB₂ on an industrial scale.

2.4.1 Mg powder

All of the studies on Mg precursor have only focused on the Mg stoichiometry effect, while there has been no detailed report on the effect of the purity of the Mg on the critical current density and transition temperature [98-102]. All the reports on the effect on the critical temperature so far vary significantly, which is most probably due to different preparation conditions and starting precursors. However, Mg deficiency samples show a degraded critical temperature [102—108].

Very recently, K. S. Tan investigated the influence of magnesium precursor powders and annealing temperatures on the transition temperatures (T_c) and critical current densities (J_c) of *in situ* MgB₂/Fe wires [109]. Three types of magnesium powder, with particle sizes of 44 μ m (Alfa Aesar), 12–17 μ m (Tangshan Weihao) and 4–6 μ m (Tangshan Weihao), and boron powder (Tangshan Weihao), with 95–97% purity and particle size of less than 1 μ m, were used as starting precursor powders, as shown in Figure 2.29.

Please see print copy for Figure 2.29

Figure 2.29 SEM images of the magnesium powders with a particle size of (a) 44 μm (Alfa Aesar), (b) 12–17 μm (TangshanWeihao), (c) 4–6 μm (TangshanWeihao), and (d) boron powder with 95–97% purity from TangshanWeihao [109].

The mixed powders were packed into Fe tubes and then drawn to about 1.7 mm in diameter using the standard powder in-tube (PIT) method. The samples were labeled as W5, W6, and W7, from highest to lowest Mg particle size. Figure 2.30 compares the critical current density, J_c , for samples W5, W6, and W7, which were heat-treated at 700 °C for 30 min. The sample with the smallest particle size of the magnesium powder, W7, shows the highest J_c value among the three samples. When using a magnesium powder with small particle size as the precursor, the magnesium is expected to react more uniformly and quickly, leading to the formation of MgB_2 with a small grain size. Therefore, this increases the grain boundary pinning, which in turn improves the J_c of the wire.

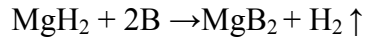
Please see print copy for Figure 2.30

Figure 2.30 Comparison of critical current density, J_c , as a function of magnetic field at 5 and 20 K for samples W5, W6, and W7 annealed at 700 °C for 30 min [109].

Yamada *et al.* has proved that the transport J_c values of un-doped and 10 mol% SiC doped tapes prepared with nanometre-size Mg powder reached 90 and 250 A/mm² at 4.2 K and 10 T, respectively. These values were about five times higher than those of the tapes prepared with commercial Mg powder [110,111]. The use of an ultra-fine Mg and B powder mixture prepared by ball milling also effectively improved the grain connections and enhanced the J_c values [75, 79].

2.4.2 MgH₂ powder instead of Mg powder

Kumakura's group has systematically studied the effect of the Mg on the critical current density. They achieved twice as large a J_c by using MgH₂ as the Mg source in the same way as for samples prepared using the mixture of Mg + B powders [112]. During the heat treatment, the reaction occurs as follows:



At the same time, the $\text{MgH}_2 + \text{B}$ mixture was effective in obtaining a high density of the core layer, due to the formation of MgB_2 in preference to Fe_xB , which competes with it. This reaction reduced the formation of Fe_xB . On the other hand, the surface of the starting Mg powders is likely to be contaminated with oxygen in $\text{Mg} + \text{B}$ processing, which causes a decrease in the reactivity of Mg with B. Thus, the slow reaction between Mg and B causes non-negligible formation of Fe_xB .

2.5 Chemical Doping Effects

“Pure” MgB_2 is not so good for applications due to the poor flux pinning and low J_c , H_{c2} , and H_{irr} values. A significant enhancement of critical current density (J_c) in MgB_2 can be achieved through chemical doping with various kinds of materials. Chemical doping is a simple and readily scalable technique. A significant enhancement of critical current density (J_c) in MgB_2 can be achieved through chemical doping with carbon (C) containing composites or compounds, such as SiC, C, B_4C , carbon nanotubes (CNT), hydrocarbons, carbohydrates, etc. The C can enter the MgB_2 structure by substituting into boron (B) sites, and thus J_c and H_{c2} are significantly enhanced due to the increased impurity scattering in the two-band MgB_2 [78, 84-88, 91, 113-117].

2.5.1 Dual reaction model and dopant categories

In 2007, Dou *et al.* [83] proposed a dual reaction model based on the following factors to explain the mechanism behind the enhanced electromagnetic properties from SiC and C doping. They demonstrated that

- There is a dual reaction model in which the C substitution due to nano-SiC doping and MgB_2 formation take place simultaneously at the MgB_2 formation temperature.
- C substitution induces highly localised fluctuations in structure and T_c , which are responsible for the enhancement in J_c , H_{irr} , and H_{c2} by SiC doping.
- The dual reaction model can explain the effects of the known dopants and predicts efficient dopants. This has significant ramifications for a wider range of materials, which are shown in Table 2.6.

- Disorder created by all means has a universal influence on the electromagnetic properties of MgB_2 .
- Free and reactive C is the key to searching for better dopants.

Please see print copy for Table 2.5

Table 2.5 Ranking of dopants by Dual Reaction Model [Dou, 2007-EUCAS].

2.5.2 Carbohydrate Doping

The merits of carbohydrate doping [44-46, 118-123]:

- Carbohydrates dissolve in a solvent, and after drying, the carbohydrate is coated onto the B powder surface to form a highly uniform mixture.
- The carbohydrates in the mixture melt and decompose at temperatures below the formation temperature of MgB_2 , hence producing highly reactive and free carbon on the atomic scale.
- A reducing reagent, carbon or carbon monoxide, is created, which may convert boron oxide to B, reducing impurities in the B powder.
- The C substitution for B can take place at the same temperature as the formation temperature of MgB_2 . The simultaneous dual reactions promote C substitution for B and defects within the grains, resulting in the enhancement of J_c , H_{irr} , and H_{c2} .
- Carbohydrate doping is cheaper than for other dopants, easy to process, and does not need to use expensive nanoscale materials, because solution coating is on the atomic scale.

The disadvantage of carbohydrates, for example, malic acid ($\text{C}_4\text{H}_6\text{O}_5$), is that they normally consist of carbon (C), oxygen (O), and hydrogen (H), so that the O can easily react with Mg to form MgO, which may enhance the vortex pinning, but also strongly degrades the connectivity if present between MgB_2 grains, as seen in O-contaminated MgB_2 . Our group has continued to suggest a different hydrocarbon, pyrene ($\text{C}_{16}\text{H}_{10}$), without any oxygen content, as the C source, and the details will be in Chapter 8. The doping effect of home-made submicron-sized carbon spheres (CS) will also be discussed in Chapter 9.

2.6 Large-scale application with MgB₂

In comparison with other superconducting wires, the production cost of MgB₂ is said to be only partially related to the raw material costs. This would give to any producer a larger margin of possibility to reduce its cost by a strong optimization of the manufacturing plant and by improving work organization. There is a remarkable improvement in the production time by a reduction of a factor of two using the same basic equipment. Columbus Superconductors is now building new pilot plant facility with new equipment being able to further reduce its production costs quite substantially. A direct comparison with the current price of the NbTi wires in the low field region is still difficult because it is not straightforward to estimate the real benefit for an end user to switch to MgB₂, due to the higher nominal operating temperature, which reduces the cooling costs significantly. On the contrary, in the liquid helium region it is not difficult to compare the MgB₂ cost with the Nb₃Sn and BSCCO-2212 and BSCCO-2223 wire and realize that it will be possible in the near future to become competitive with these alternative solutions[184].

ASG Superconductors started to design an open MRI magnet based on the use of MgB₂ conductors well in advance compared with the expected industrialization of the conductor. Several times during the engineering study, the design was changed to follow the evolution of the conductor. On the other hand, this gave the possibility to start winding the first double pancake composing the magnet just few weeks after the production of the conductor by Columbus Superconductors in its first real and usable length. The magnet (shown in Figure 2.31) was finally assembled and the tests were already started with positive results.



Please see print copy for Figure 2.31

Figure 2.31 The ASG MRI 0.5 T cryogenic-free magnet [184].

In general it was confirmed that the 18 km of conductor used to wind the coils are satisfying the requirements of this MRI system. The magnet reached its nominal current of 90 A and the central field of 0.5 T without any training. The 12 double pancakes are electrically connected to each other in series with optimized but still resistive joints, as the superconducting joint technology was not yet successfully developed in ASG Superconductors at that time. The plan for this product is to put it on the MRI market as soon as the tests and the full industrialization will be successfully completed. When this will happen, the first large scale commercial application of MgB_2 superconductor will be already out in the market [184].

From 2006, several MgB_2 FCL prototypes (Figure. 2.31) were built in the framework of the LIMSAT Italian project. The test results of them were in sufficient agreement with what expected from the transport properties of the conductor: the non-inductive winding has reached a critical current in the order of 600 A. These non-inductive windings were

tested with AC transport currents both in liquid He and in liquid Ne at different frequencies (from 2 to 500 Hz) and different peak to peak currents up to several times the I_c [184].

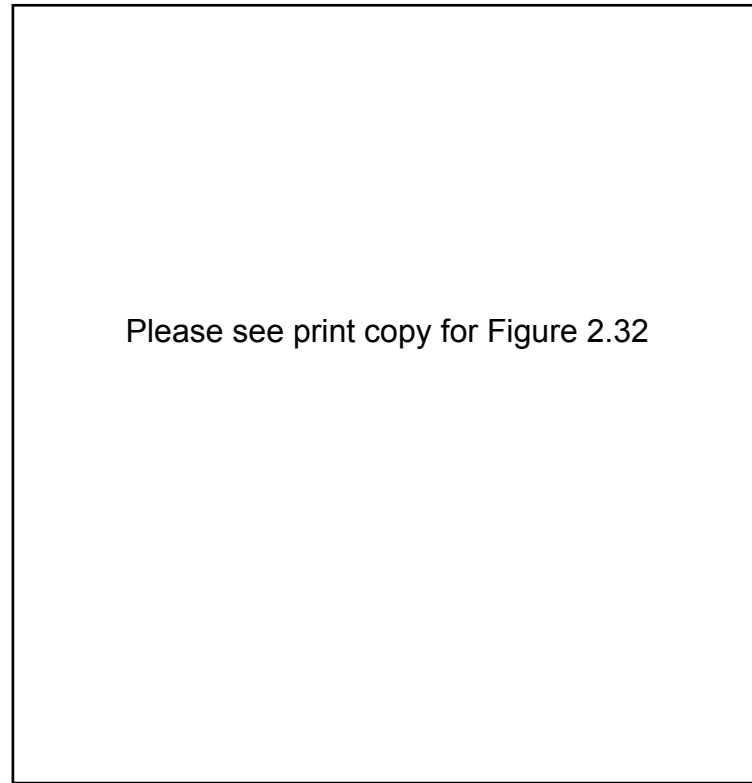


Figure 2.32 Three of the five FCL prototypes produced [184]

Several prototype solenoids were realized with different conductors and different winding technique, producing a central magnetic field up to 5 T. The possibility to wind an already reacted conductor in a relative small diameter without any degradation is demonstrated with the test of one solenoid R&W magnet wound on 135 mm ID.

The solenoid made with 0.5 km of multifilament MgB_2 tape reached about the short sample limit at 20 K without any training. This magnet reached a central field of 1 T at an operating temperature of 16 K[184].

In the past two years, the MgB_2 has demonstrated the potential to approach a solid industrial development. Several long lengths of conductor were already produced and

delivered to customers by different manufacturers. If the possibility to perform superconducting joints could be demonstrated, it will indicate that MgB_2 will become one of the primary actors in the future market of superconducting materials.

2.7 References

1. K. Vinod, R. G. Abhilash Kumar, and U. Syamaprasad, *Supercond. Sci. Technol.* **20** R1-13, (2007).
2. A. Stenvall, A. Korpela, R. Mikkonen, and G. Grasso, *Supercond. Sci. Technol.* **19** 184-189, (2006).
3. M. D. Sumption, M. Bhatia, F. Buta, S. Bohnenstiehl, M. Tomic, M. Rindfleisch, J. Yue, J. Phillips, S. Kawabata, and E. W. Collings, *Supercond. Sci. Technol.* **18** 961-965, (2005).
4. H. Kumakura, A. Matsumoto, T. Nakane, and H. Kitaguchi, *Physica C*, **456** 196 - 202, (2007).
5. J. M. Rowell, *Supercond. Sci. Technol.* **16** R17-27 (2003).
6. A. V. Pogrebnyakov, J. M. Redwing, J. E. Jones, X. X. Xi, S. Y. Xu, Q. Li, V. Vaityanathan, and D. G. Schlom, *Appl. Phys. Lett.* **82** 4319-4321, (2003).
7. M. Tomic, M. Rindfleisch, J. Yue, K. McFadden, J. Phillips, M. Sumption, M. Bhatia, S. Bohnenstiehl, and E. W. Collings, *Physica C* **456** 203-208, (2007).
8. S. Hata, T. Yoshidome, H. Sosiati, Y. Tomokiyo, N. Kuwano, A. Matsumoto, H. Kitaguchi, H. Kumakura, *Supercond. Sci. Technol.* **19** 161-168, (2006).
9. H. Fang, Y.Y. Xue, Y.X. Zhou, A. Baikalov, and K. Salama, *Supercond. Sci. Technol.* **17** L27-29 (2004).
10. C. F. Liu, G. Yan, S. J. Du, W. Xi, Y. Feng, P. X. Zhang, X. Z. Wu, and L. Zhou, *Physica C* **386** 603-606 (2003).
11. Y. Zhu, L. Wu, V. Volkov, Q. Li, G. Gu, A. R. Moodenbaugh, M. Malac, M. Suenaga, and J. Tranquada, *Physica C* **356** 239-253, (2001).
12. D. Eyidi, O. Eibl, T. Wenzel, K. G. Nickel, M. Giovannini, and A. Saccone, *Micro n* **34** 85-96, (2003).
13. D. C. Larbalestier et al., *Nature*, **410** 186-189, (2001).
14. H. Kim, W. N. Kang, E. Choi, M. Kim, K. H. P. Kim, and S. Lee, *Phys. Rev. Lett.* **87** 087002, (2001).
15. M. Kim, C. U. Jung, M. Park, S. Y. Lee, K. H. P. Kim, W. N. Kang, and S. Lee, *Phys. Rev. B*. **64** 012511, (2001).
16. M. J. Qin, X. L. Wang, H. K. Liu, and S. X. Dou, *Phys. Rev. B*. **65** 132508, (2002).

17. M. Eisterer, M. Zehetmayer, and H. W. Weber, *Phys. Rev. Lett.* **90** 247002, (2003).
18. S. Y. Xu, Q. Li, E. Wertz, Y. F. Hu, A. V. Pogrebnyakov, X. H. Zeng, X. X. Xi, and J. M. Redwing, *Phys. Rev. B* **68** 224501, (2003).
19. H. Kitaguchi, A. Matsumoto, H. Kumakura, T. Doi, H. Yamamoto, K. Saitoh, H. Sosiati, and S. Hata, *Appl. Phys. Lett.* **85** 2842-2844, (2004).
20. S. X. Dou et al, *arxiv:/cond-mat/0701391*.
21. Z. X. Shi, A. K. Pradhan, M. Tokunaga, K. Yamazaki, T. Tamegai, Y. Takano, K. Togano, H. Kito, and H. Ihara, *Phys. Rev. B* **68** 104514, (2003).
22. Z. X. Shi, J. Wang, H. Lv, and T. Tamegai, *Physica C* **449**, 104-108 (2006).
23. J. H. Kim, S. X. Dou, J. L. Wang, D. Shi, X. Xu, M. S. A. Hossain, W. K. Yeoh, S. Choi, and T. Kiyoshi, *Supercond. Sci. Tech.* **20** 448-451, (2007).
24. J. H. Kim, S. X. Dou, D. Q. Shi, M. Rindfleisch, and M. Tomsic, *Supercond. Sci. Technol.* **20** 1026-1031, (2007).
25. J. Nagamatsu, N. Nakagawa, T. Muranaka, Y. Zenitani, and J. Akimitsu, *Nature* **410** 63-64, (2001).
26. L. H. He, L. Hu, P.L. Zhang, and Q.W. Yan, *Chin. Phys.* **10** 343-344, (2001).
27. G. Y. Sung, S. H. Kim, J. H. Kim, D. C. Yoo, J. W. Lee, J. H. Lee, C. H. Jung, M. S. Park, W. N. Kang, Z. L. Du, and S. I. Lee, *Supercond. Sci. Technol.* **14** 880-883, (2001).
28. S. Margadonna, T. Muranaka, K. Prassides, I. Maurin, K. Brigatti, R. M. Ibberson, M. Arai, M. Takata, and J. Akimitsu, *J. Phys.:Condens. Matter.* **13** L795-802, (2001).
29. R. C. Yu, S. C. Li, Y. Q. Wang, X. Kong, J. L. Zhu, F. Y. Li, Z. X. Liu, X. F. Duan, Z. Zhang, and C. Q. Jin, *Physica C* **363** 184-188, (2001).
30. J. Kortus, I. I. Mazin, K. D. Belashchenko, V. P. Antropov, and L. L. Boyer, *Phys. Rev. Lett.* **86** 4656-4659, (2001).
31. J. M. An and W. E. Pickett, *Phys. Rev. Lett.* **86** 4366-4369, (2001).
32. S. L. Bud'ko, G. Lapertot, C. Petrovic, C. E. Cunningham, N. Anderson, and P. C. Canfield, *Phys. Rev. Lett.* **86** 1877-1880, (2001).
33. A. Sharoni, I. Felner, and O. Millo, *Phys. Rev. B* **63** 2205081-2205084, (2001).
34. H. Kotegawa, K. Ishida, Y. Kitaoka, T. Muranaka, and J. Akimitsu, *Phys. Rev. Lett.* **87** 127001-127004, (2001).

35. H. L. Suo, C. Beneduce, M. Dhallé, N. Musolino, J. Y. Genoud, and R. Flükiger, *Appl. Phys. Lett.* **79** 3116-3118, (2001).
36. H. Kumakura, A. Matsumoto, H. Fujii, and K. Togano, *Appl. Phys. Lett.* **79**, 2435-2437, (2001).
37. G. Grasso, A. Malagoli, C. Ferdeghini, S. Roncallo, V. Braccini, A. S. Siri, and M. R. Cimberle, *Appl. Phys. Lett.* **79** 230-232, (2001).
38. A. Serquis, L. Civale, D. L. Hammon, J. Y. Coulter, X. Z. Liao, Y. T. Zhu, D. E. Peterson, and F. M. Mueller, *Appl. Phys. Lett.* **82** 1754-1756, (2003).
39. Q. Feng, C. Chen, J. Xu, L. Kong, X. Chen, Y. Wang, Y. Zhang, and Z. Gao, *Physica C*, **411** 41-46, (2004).
40. T. Nakane, H. Takeya, H. Fujii, and H. Kumakura, *Supercond. Sci. Technol.* **18**, 521-525 (2005).
41. J. H. Kim, W. K. Yeoh, M.J. Qin, X. Xu, and S. X. Dou, *J. Appl. Phys.* **100** 013908, (2006).
42. J. H. Kim, W. K. Yeoh, M. J. Qin, X. Xu, and S. X. Dou, P. Munroe, H. Kumakura, T. Nakane, and C. H. Jiang, *Appl. Phys. Lett.* **89** 122510 (2006).
43. S. X. Dou, S. Soltanian, J. Horvat, X. L. Wang, S. H. Zhou, M. Ionescu, H. K. Liu, P. Munroe, and M. Tomsic, *Appl. Phys. Lett.* **81** 3419-3421, (2002).
44. J. H. Kim, S. Zhou, M.S.A. Hossain, A.V. Pan, and S. X. Dou, *Appl. Phys. Lett.* **89**, 142505, (2006).
45. J. H. Kim, S. X. Dou, M. S. A. Hossain, X. Xu, J. L. Wang, D. Q. Shi, T. Nakane, and H. Kumakura, *Supercond. Sci. Technol.* **20** 715-719, (2007).
46. M. S. A. Hossain, J. H. Kim, X. Xu, X.L. Wang, M. Rindfleisch, M. Tomsic, M. D. Sumption, E. W. Collings, and S. X. Dou, *Supercond. Sci. Technol.*, **20** L51-54, (2007).
47. J. H. Kim, W. K. Yeoh, X. Xu, S. X. Dou, P. Munroe, M. Rindfleisch, and M. Tomsic, *Physica C* **449** 133-138, (2006).
48. S. Yan, Y. Lu, G. Liu, G. Yan, and L. Zhou, *J. Alloys Compd.* **443** 161-165, (2007).
49. S. C. Yan, G. Yan, C. F. Liu, Y. F. Lu, and L. Zhou, *J. Alloys Compd.* **437** 298-301, (2007).
50. S. Bohnenstiehl, S. A. Dregia, M. D. Sumption, and E. W. Collings, *IEEE Trans. Appl. Supercond.* **17** 2754-2756, (2007).

51. M. Bhatia, M. D. Sumption, S. Bohnenstiehl, S. A. Dregia, E. W. Collings, M. Tomsic, and M. Rindfleisch, *IEEE Trans. Appl. Supercond.* **17** 2750-2753, (2007).
52. B. Q. Fu, Y. Feng, G. Yan, C. F. Liu, L. Zhou, L. Z. Cao, K. R. Ruan, and X. G. Li, *Physica C* **392-396** 1035-1038, (2003).
53. W. Goldacker, S. I. Schlachter, B. Obst, B. Liu, J. Reiner, and S. Zimmer, *Supercond. Sci. Technol.* **17** S363-368, (2004).
54. H. L. Xu, Y. Feng, Z. Xu, C. S. Li, G. Yan, E. Mossang, and A. Sulpice, *Physica C* **419** 94-100, (2005).
55. C. H. Jiang, H. Hatakeyama, and H. Kumakura, *Physica C* **423**, 45-50, (2005).
56. Z. K. Liu, Y. Zhong, D. G. Schlom, Q. Li, and X. X. Xi, *CALPHAD: Comput. Coupling Phase Diagrams Thermochem.* **25** 299, (2001).
57. Y. J. Liang, and Y. C. Che, *Data Handbook of Mineral Thermodynamics*, China: Northeastern University Press, (1993).
58. A. Yamamoto, J. Shimoyama, S. Ueda, Y. Katsura, I. Iwayama, S. Horii, and K. Kishio, *Appl. Phys. Lett.* **86** 212502-1-212502-3, (2005).
59. C. B. Eom et al., *Nature* **411** 558-560, (2001).
60. S. Lee, T. Masui, H. Mori, Y. Eltsev, A. Yamamoto, and S. Tajima, *Supercond. Sci. Technol.* **16** 213-220, (2003).
61. A. Gurevich, *Phys. Rev. B.* **67** 184515, (2003).
62. V. Braccini, L. D. Cooley, S. Patnaik, D. C. Larbalestier, P. Manfrinetti, A. Palenzona, and A. S. Siri, *Appl. Phys. Lett.* **81** 4577-4579, (2002).
63. Y. Yamada, M. Nakatsuka, A. Nitta, K. Tachikawa, and H. Kumakura, *IEEE Trans. Appl. Supercond.* **17** 2911-2914, (2007).
64. T. Nakane, H. Kitaguchi, and H. Kumakura, *Appl. Phys. Lett.* **88** 022513, (2006).
65. R. A. Ribeiro, S. L. Bud'ko, C. Petrovic, and P. C. Canfield, *Physica C* **385** 16, (2003).
66. S. H. Zhou, A. V. Pan, J. Horvat, M. J. Qin, and H. K. Liu, *Supercond. Sci. Technol.* **17** S528, (2004).
67. S. K. Chen, K. A. Yates, M. G. Blamire, and J. L. MacManus-Driscoll, *Supercond. Sci. Technol.* **18** 1473, (2005).
68. X. Xu, M. J. Qin, K. Konstantinov, Dayse I dos Santos, W. K. Yeoh, J. H. Kim, and S. X. Dou, *Supercond. Sci. Technol.* **19** 466, (2006).

69. R. Flukiger, H. L. Suo, N. Musolino, C. Beneduce, P. Toulemonde, and P. Lezza, *Physica C* **385** 286, (2003).
70. W. Häßler, B. Birajdar, W. Gruner, M. Herrmann, O. Perner, C. Rodig, M. Schubert, B. Holzapfel, O. Eibl, and L. Schultz, *Supercond. Sci. Technol.* **19** 512, (2006).
71. A. Gümbel, J. Eckert, G. Fuchs, K. Nenkov, K. H. Müller, and L. Schultz, *Appl. Phys. Lett.* **80** 2725, (2002).
72. A. Gümbel, O. Perner, J. Eckert, G. Fuchs, K. Nenkov, K. H. Müller, and L. Schultz, *IEEE Trans. Appl. Supercond.* **13** 3064, (2003).
73. H. Abe, M. Naito, K. Nogi, M. Matsuda, M. Miyake, S. Ohara, A. Kondo, and T. Fukui, *Physica C* **391** 211, (2003).
74. W. Hassler, C. Rodig, C. Fischer, B. Holzapfel, O. Perner, J. Eckert, K. Nenkov, and G. Fuchs, *Supercond. Sci. Technol.* **16** 281, (2003).
75. C. Fischer, C. Rodig, W. Hassler, O. Perner, J. Eckert, K. Nenkov, G. Fuchs, H. Wendrock, B. Holzapfel, and L. Schultz, *Appl. Phys. Lett.* **83** 1803, (2003).
76. O. Perner, W. Hassler, C. Fischer, G. Fuchs, B. Holzapfel, L. Schultz, and J. Eckert, *IEEE Trans. Appl. Supercond.* **15** 3192, (2005).
77. Y. D. Gao, J. Ding, G. V. S. Rao, B. V. R. Chowdari, W. X. Sun, and Z. X. Shen, *Phys. Status Solid. A* **191** 548, (2002).
78. B. J. Senkowicz, J. E. Giencke, S. Patnaik, C. B. Eom, E. E. Hellstrom, and D. C. Larbalestier, *Appl. Phys. Lett.* **86**, 202502 (2005).
79. H. Fang, S. Padmanabhan, Y. X. Zhou, and K. Salama, *Appl. Phys. Lett.* **82** 4113, (2003).
80. A. Matsumoto, H. Kumakura, H. Kitaguchi, H. Hatakeyama, H. Yamada, and M. Hirakawa, *IEEE Transactions On Applied Supercond.* **15**(2) 3333, (2005).
81. M. Herrmann, W. Haessler, C. Mickel, W. Gruner, B. Holzapfel, and L. Schultz, *Supercond. Sci. Technol.* **20** 1108, (2006).
82. M. Herrmann, W. Haessler, C. Rodig, W. Gruner, B. Holzapfel, and L. Schultz, *Appl. Phys. Lett.* **91** 082507, (2007).
83. S. X. Dou, O. Shcherbakova, W. K. Yeoh, J. H. Kim, S. Soltanian, X. L. Wang, C.

- Senatore, R. Flukiger, M. Dhalles, O. Hušnjak, and E. Babić, *Phys. Rev. Lett.* **98**, 139902 (2007).
84. S. X. Dou, S. Soltanian, J. Horvat, X. L. Wang, S. H. Zhou, M. Ionescu, H. K. Liu, P. Munroe, and M. Tomsic, *Appl. Phys. Lett.* **81** 3419, (2002).
 85. S. X. Dou, W. K. Yeoh, J. Horvat, and M. Ionescu, *Appl. Phys. Lett.* **83** 4996, (2003).
 86. H. Kumakura et al., *Appl. Phys. Lett.* **84** 3669, (2004).
 87. M. D. Sumption, M. Bhatia, M. Rindfleisch, M. Tomsic, S. Soltanian, S. X. Dou, and E. W. Collings, *Appl. Phys. Lett.* **86** 092507, (2005).
 88. S. X. Dou, V. Braccini, S. Soltanian, R. Klie, Y. Zhu, S. Li, X. L. Wang, and D. Larbalestier, *J. Appl. Phys.* **96** 7549, (2004).
 89. J. H. Kim et al., *Appl. Phys. Lett.* **92** 042506, (2008).
 90. X. L. Wang, Z. X. Cheng, and S. X. Dou, *Appl. Phys. Lett.* **90** 042501, (2007).
 91. R. H. T. Wilke, S. L. Bud'ko, P. C. Canfield, D. K. Finnemore, R. J. Suplinskas, and S. T. Hannahs, *Phys. Rev. Lett.* **92** 217003, (2004).
 92. P. Lezza, C. Senatore, and R. Flukiger, *Supercond. Sci. Technol.* **19** 1030, (2006).
 93. A. Matsumoto, H. Kumakura, H. Kitaguchi, B.J. Senkowicz, M.C. Jewell, E.E. Hellstrom, Y. Zhu, P.M. Voyles, and D.C. Larbalestier, *Appl. Phys. Lett.* **89** 132508, (2006).
 94. G. Serrano et al., *J. Appl. Phys.* **103** 023907, (2008).
 95. <http://www.webelements.com/boron/>
 96. <http://www.roskill.com/reports/prePublication/prepubboron>
 97. W. Häßler, M. Herrmann, C. Rodig, M. Schubert, K. Nenkov, and B. Holzapfel, *Supercond. Sci. Technol.* **21** 062001, (2008).
 98. R. A. Ribeiro, S. L. Bud'ko, C. Petrovic, and P. C. Canfield, *Physica C* **384** 227, (2003).
 99. H. Xiao, W. Peng, W. H. Song, R. C. Ma, J. J. Du, and Y. P. Sun, *Physica C* **386** 648, (2003).
 100. C. M. Franco, B. Ferreira, C. A. M. dos Santos, L. Ghivelder, H. J. I. Filho, and A. J. S. Machado, *Physica C* **408–410** 130, (2004).
 101. R. Ribeiro, S. L. Bud'ko, C. Petrovic, and P.C. Canfield, *Physica C* **382** 194, (2002).

102. S. H. Zhou, A. V. Pan, J. Horvat, M. J. Qin, and H. K. Liu, *Supercond. Sci. Technol.* **17** S528, (2004).
103. P. A. Sharma, N. Hur, Y. Horibe, C. H. Chen, B. G. Kim, S. Guha, Marta Z. Cieplak, and S-W. Cheong, *Phys. Rev. Lett.* **89**, 167003 (2002).
104. Y. G. Zhao, X. P. Zhang, P. T. Qiao, X. L. Wang, and B. L. Gu, *Physica C* **366** 1, (2001).
105. A. Serquis, Y. T. Zhu, E. J. Peterson, J. Y. Coulter, D. E. Peterson, and F. M. Mueller, *Appl. Phys. Lett.* **79** 4399, (2001).
106. R. A. Ribeiro, S. L. Budko, C. Petrovic, and P. C. Canfield, *Physica C* **382** 194, (2002).
107. C. Buzeal, and T. Yamashita, *Supercond. Sci. Technol.* **14** R115, (2002).
108. P. Lezza, V. Abacherli, N. Clayton, C. Senatore, D. Uglietti, H. L. Suo, and R. Flukiger, *Physica C* **401** 305, (2004).
109. K. S. Tan, N. K. Kim, Y. J. Kim, B. H. Jun, and C. J. Kim, *Supercond. Sci. Technol.* **21** 015015, (2008).
110. H. Yamada, M. Hirakawa, H. Kumakura, A. Matsumoto, and H. Kitaguchi, *Appl. Phys. Lett.* **84** 1728, (2004).
111. H. Yamada, M. Hirakawa, H. Kumakura, A. Matsumoto, and H. Kitaguchi, *IEEE Trans. Appl. Supercond.* **15** 3337, (2005).
112. H. Fujii, K. Togano, and H. Kumakura, *Supercond. Sci. Technol.* **15** 1571, (2002).
113. S. Soltanian et al., *Physica C* **390** 185, (2003).
114. V. Braccini, et al, *Phys. Rev. B* **71** 012504-4, (2004).
115. A. Yamamoto, J. Shimoyama, S. Ueda, I. Iwayama, S. Horii, and K. Kishio, *Supercond. Sci. Technol.* **18**, 1323, (2005).
116. S. X. Dou, W. K. Yeoh, O. Shcherbakova, Y. Li, Z. M. Ren, D. Wexler, P. Munroe, S. K. Chen, K. S. Tan, B. A. Glowacki, and J. L. MacManus-Driscoll, *Adv. Mater.* **18** 785, (2006).
117. S. K. Chen, K. S. Tan, B. A. Glowacki, W. K. Yeoh, S. Soltanian, J. Horvat, S. X. Dou, *Appl. Phys. Lett.* **87** 182504, (2005).
118. S. H. Zhou, A.V. Pan, S.X. Dou, and D. Wexler, *Adv. Mater.* **19** 13, (2007).
119. Z. S. Gao, Y. W. Ma, X. P. Zhang, D. L. Wang, Z. G. Yu, K. Watanabe, H. Yang, and H. H. Wen, *Supercond. Sci. Technol.* **20** 485-489, (2007).

120. Z. S. Gao, Y. W. Ma, X. P. Zhang, D. L. Wang, Z. G. Yu, K. Watanabe, H. Yang, E. Mossang, *J. Appl. Phys.* **102** 013914, (2007).
121. M. S. A. Hossain, J. H. Kim, X. L. Wang, X. Xu, G. Peleckis, and S X Dou, *Supercond. Sci. Technol.* **20** 112-116, (2007).
122. B. H. Jun, and C. J. Kim, *Supercond. Sci. Technol.* **20** 980–985, (2007).
123. Z. S. Gao, Y. W. Ma, X. P. Zhang, and D. L. Wang, *Appl. Phys. Lett* **91** 162504, (2007).
124. H. Yamada, M. Hirakawa, H. Kumakura, and H. Kitaguchi, *Supercond. Sci. Technol.* **19** 175, (2006).
125. H. Yamada, N. Uchiyama, H. Kumakura, H. Kitaguchi, and A. Matsumoto, *IEEE Trans. Appl. Supercond.* **17** 2850-2853, (2007).
126. H. Yamada, N. Uchiyama, A. Matsumoto, H. Kitaguchi, and H. Kumakura, *Supercond. Sci. Technol.* **20** L30–L33, (2007).
127. W. Mickelson, J. Cumings, E.Q. Han, and A. Zettl, *Phys. Rev. B* **65** 0525051 (2002).
128. Z. Hol’anov, J. Kačmarčík a, P. Szabő, P. Samuely, I. Sheikin, R. A. Ribeiro, S. L. Bud’ko, and P. C. Canfield, *Physica C* **404**, 195, (2004).
129. A. Yamamoto, J. Shimoyama, S. Ueda, Y. Katsura, S. Horii, and K. Kishio, *IEEE Trans. Appl. Supercond.* **15** 3292, (2005).
130. S. Ueda, J. Shimoyama, A. Yamamoto, Y. Katsura, I. Iwayama, S. Horii, and K. Kishio, *Physica C* **426–431** 1225, (2005).
131. T. Takenobu, T. Ito, D.H. Chi, K. Prassides, and Y. Iwasa, *Phys. Rev. B* **64** 134513, (2001).
132. M. Paranthaman, J. F. Thompson, and D. K. Christen, *Physica C* **355** 1, (2001).
133. J. S. Ahn, E. J. Choi, Preprint, *cond-mat/0103169*, (2001).
134. M. J. Mehl, D. A. Papaconstantopoulos, and D. J. Singh, *Phys. Rev. B* **64** 1405091, (2001).
135. Maurin, S. Margadonna, K. Prassides, T. Takenobu, Y. Iwasa, and A.N. Fitch, *Chem. Mater.* **14** 3894, (2002).
136. Maurin, S. Margadonna, K. Prassides, T. Takenobu, T. Ito, D. H. Chi, Y. Iwasa, and A. Fitch, *Physica B* **318** 392, (2002).
137. Bharathi, S. J. Balaselvi, S. Kalavathi, G. L.N. Reddy, V. S. Sastry, Y. Haritharan,

138. Y. Yan and M. M. Al-Jassim, *J. Appl. Phys.* **92** 7687, (2002).
139. S. Lee, T. Masui, A. Yamamoto, H. Uchiyama, and S. Takama, *Physica C* **397** 7, (2003).
140. P. Samuely, Z. Holanová, P. Szabo, J. Kacmarčík, R. A. Ribeiro, S. L. Budko, and P. C. Canfield, *Phys. Rev. B* **68** 020505, (2003).
141. H. Schmidt, K. E. Gray, D. G. Hinks, J. F. Zasadzinski, M. Avdeev, J. D. Jorgensen, and J. C. Burley, *Phys. Rev. B* **68** 060508, (2003).
142. M. Avdeev, J. D. Jorgensen, R. A. Ribeiro, S. L. Budko, and P. C. Canfield, *Physica C* **387** 301, (2003).
143. P. P. Singh, *Solid State Commun.* **127** 271, (2003).
144. A. Papangelis, J. Arvanitidis, I. Margiolaki, K. Brigatti, K. Prassides, A. Schenck, A. Lappas, A. Amato, Y. Iwasa, and T. Takenobu, *Physica B* **326** 346, (2003).
145. W. K. Yeoh, J. H. Kim, J. Horvat, X. Xu, M. J. Qin, S. X. Dou, C. H. Jiang, T. Nakane, H. Kumakura, and P. Munroe, *Supercond. Sci. Technol.* **19** 596, (2006).
146. Y. Ma, X. Zhang, G. Nishijima, K. Watanabe, S. Awaji, and X. Bai, *Appl. Phys. Lett.* **88** 07250, (2006).
147. J. Wei, Y. Li, C. Xu, B. Wei, and D. Wu, *Mater. Chem. Phys.* **78** 785, (2003).
148. W. K. Yeoh, J. Horvat, S. X. Dou, and V. Keast, *Supercond. Sci. Technol.* **17** S572, (2004).
149. J. H. Kim, W. K. Yeoh, M. J. Qin, X. Xu, S. X. Dou, P. Munroe, H. Kumakura, T. Nakane, and C. H. Jiang, *Appl. Phys. Lett.* **89** 122520, (2006).
150. W. K. Yeoh, J. Horvat, S. X. Dou, and P. Munroe, *IEEE Trans. Appl. Supercond.* **15** 3284, (2005).
151. W. K. Yeoh, J. H. Kim, J. Horvat, S. X. Dou, P. Munroe, *Supercond. Sci. Technol.* **19** L5, (2006).
152. B. Q. Wei, R. Vajtai, and P. M. Ajayan, *Appl. Phys. Lett.* **79** 1172, (2001).
153. P. Kim, L. Shi, A. Majumdar, and P. L. McEuen, *Phys. Rev. Lett.* **87** 215502, (2001).
154. M. M. J. Treacy, T. W. Ebbesen, and J. M. Gibson, *Nature* **381** 678, (1996).
155. Y. Zhao, C. H. Cheng, X. F. Rui, H. Zhang, P. Munroe, H. M. Zeng, N. Koshizuka, and M. Murakami, *Appl. Phys. Lett.* **83** 2916, (2003).

156. Vajpayee, H. Huhtinen, V. P. S. Awana, A. Gupta, R. Rawat, N. P. Lalla, H. Kishan, R. Laiho, I. Felner, and A. V. Narlikar, *Supercond. Sci. Technol.* **20** S155-158, (2007).
157. H. Cheng, H. Zhang, Y. Zhao, Y. Feng, X. F. Rui, P. Munroe, H. M. Zeng, N. Kohizu, and M. Murakami, *Supercond. Sci. Technol.* **16** 1182–1186, (2003).
158. H. L. Xu, Y. Feng, Z. Xu, G. Yan, L. Z. Cao, and X. G. Li, *Chin. Phys. Lett.* **21** 2511, (2004).
159. P. Kovac, I. Husek, V. Skakalova, J. Meyer, E. Dobrocka, M. Hirscher, and S. Roth, *Supercond. Sci. Technol.* **20** 105–111, (2007).
160. X. L. Wang, S. H. Zhou, M. J. Qin, P. R. Munroe, S. Soltanian, H. K. Liu, and S. X. Dou, *Physica C* **385** 461-465, (2003).
161. K. M. Elsabawy et al., *Solid State Communications* **123(1-2)** 1-6, (2002).
162. S. H. Zhou, H. K. Liu, J. Horvat, and S. X. Dou, *J. Low Temp. Phys.* **131** 687, (2003).
163. D. K. Finnemore, W. E. Straszheim, S. L. Budko, P. C. Canfield, Jr. N. E. Anderson, and R. J. Suplinskas, *Physica C* **385**, 278 (2003).
164. P. Kováč, I. Husek, T. Melisek, C. R. M. Grovenor, S. Haigh, and H. Jones, *Supercond. Sci. Technol.* **17** 1225, (2004).
165. G. Yan, Y. Feng, Y. F. Lu, L. Zhou, W. X. Jing, and H. H. Wen, *Physica C* **445–448** 466, (2006).
166. S. Xu, Y. Moritomo, K. Kato, and A. Nakamura, *J. of the Phys. Soc. of Japan* **70** (7) 1889-1891, (2001).
167. Matsumoto, H. Kumakura, H. Kitaguchi, and H. Hatakeyama, *Supercond. Sci. Technol.* **16** 926, (2003).
168. X. F. Rui, Y. Zhao, Y. Y. Xu, L. Zhang, X. F. Sun, Y. Z. Wang, and H. Zhang, *Supercond. Sci. Technol.* **17** 689, (2004).
169. Perner, W. Häßler, J. Eckert, C. Fischer, C. Mickel, G. Fuchs, B. Holzapfel, and L. Schultz, *Physica C* **432** 15, (2005)
170. Y. Wang, A. Bugoslavsky, L. Berenov, A. D. Cowey, Caplin, L. F. Cohen, J. L. MacManus-Driscoll, L. D. Cooley, X. Song and D. C. Larbalestier, *Appl. Phys. Lett.* **81** 2026, (2002)
171. Y. Ma, H. Kumakura, A. Matsumoto and K. Togano, *Appl. Phys. Lett.* **83** 1181, (2003).

172. C. H. Jiang, T. Nakane, and H. Kumakura, *Supercond. Sci. Technol.* **18** 902, (2005).
173. C. H. Jiang, T. Nakane, and H. Kumakura, *Physica C* **436** 118, (2006).
174. Y. Ma, H. Kumakura, A. Matsumoto, H. Takeya, and K. Togano, *Physica C* **408–410** 138, (2004).
175. M. Bhatia, M. D. Sumption, E. W. Collings, and S. Dregia, *Appl. Phys. Lett.* **87** 04 2505, (2005).
176. X. Zhang, Z. Gao, D. Wang, Z. Yu, Y. Ma, S. Awaji, and K. Watanabe, *Appl. Phys. Lett.* **89** 132510, (2006).
177. P. Kováč, I. Husek, T. Melisek, J. C. Grivel, W. Pachla, V. Strbík, R. Diduszko, J. Homeyer, and N. H. Andersen, *Supercond. Sci. Technol.* **17** L41, (2004).
178. X. Z. Liao, A. Serquis, Y. T. Zhu, J. Y. Huang, L. Civale, D. E. Peterson, F. M. Mueller, and H. F. Xu, *J. Appl. Phys.* **93** 6208, (2003).
179. Y. Moritomo, and S. Xu, *cond-matt*/**0104568**, (2001).
180. E. J. Kuzmann, Z. Homonnay, Z. Klencsar, M. Kuhberger, A. Vertes, and G. Gritznér, *Supercond. Sci. & Technol.* **15(11)** 1479-1485, (2002).
181. P. Kovac, I. Husek, T. Melisek, C. R. M. Grovenor, S. Haigh, and H. Jones, *Supercond. Sci. Technol.* **17** 1225, (2004).
182. C. Shekhar, Rajiv. Giri, R. S. Tiwari, O. N. Srivastava, and S. K. Malik, *J. Appl. Phys.* **101**, 043906 (2007).
183. D. W. Gu, Y. M. Cai, J. K. F. Yau, Y. G. Cui, T. Wu, G. K. Yuan, L. J. Shen, and X. Jin, *Physica C* **386** 643-647, (2003).
184. V. Braccini, D. Nardelli, R. Penco, and G. Grasso, *Physica C* **456** 209, (2007).

Chapter 3: Experimental Techniques

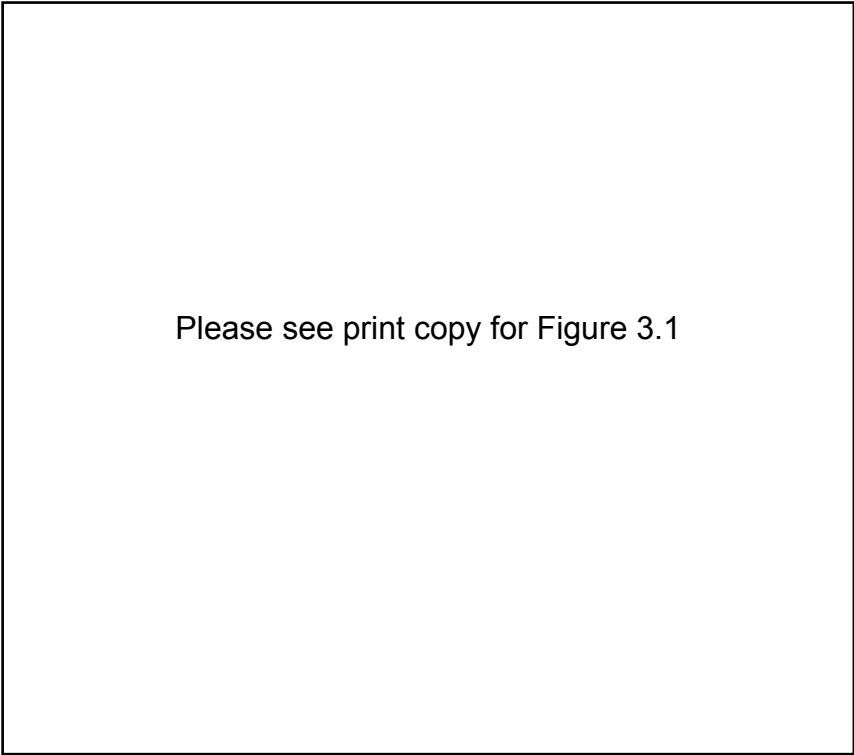
3.1 Sample Preparation and Processing Conditions

3.1.1 Planetary Ball-milling

Planetary ball mills have long been a popular tool for the finest comminuting of powders down to the micrometer range. Figure 3.1 is showing its working principles [8]. In the planetary mill, grinding bowls rotate on their own axis while simultaneously rotating through an arc around the central axis. The grinding bowls and material are thus subjected to centrifugal forces which constantly change in direction and intensity resulting in efficient, fast grinding processes. The geometries and speed ratios allow optimum movement of the grinding balls. The grinding balls rotate against the inside wall of the bowl until under specific conditions they break away from this. After being thrown across the grinding bowl, the grinding material and the balls are impacted against the opposite wall.

General effects of milling powders [1-7]:

1. Collisions plastically deform the atomic structure:
 - Introduces dislocations, vacancies, stacking faults, atomic disorder...
 - Increases strain, which is relieved by grain refinement (i.e. fracture).
More energetic milling reduces the grain size.
 - The stored energy of cold work introduced into the sample has been known to be up to 50% of enthalpy of fusion of a material



Please see print copy for Figure 3.1

Figure 3.1 planetary Ball-milling working principles [8]

2. Effect of temperature:
 - More energetic milling increases the temperature of the powder
 - Vacancy density and fracture decrease as temperature increase
 - Higher macroscopic/microscopic temperatures promote recovery from disordered state and promote diffusion
3. Greater Ball to Powder Ratio (BPR) generally only increases the collision frequency (decreases the time it takes for powders to evolve)
4. Filling the pot above 50% reduces the milling efficiency
5. Heavier milling balls increase the impact energy of collisions
6. Source of contamination is from pot/balls:
 - Less “foreign” material tends to be introduced if sample/milling media are dissimilar materials.

- *Effect* of contamination tends to be more serious if sample/milling media are dissimilar materials
- Using milling media that are of the same material as the sample is the solution if contamination critical, but compensation to retain balance of alloy may be required.

Due to different conditions, ball-milling details will be described in each of the following chapter 2 and chapter 4-7.

3.1.2 Preparation of bulk and wire samples

The samples discussed later are pure and doped MgB_2 bulks and wire samples, which is either prepared from Mg and B via in situ reaction or from commercially available MgB_2 (ex situ powder). Because of variation in the annealing process, details will be expatiated in each of the following chapter 4-9.

3.2 Sample characterization

3.2.1 Particle Size Analysis

Particle size distribution was determined using a Particle Size Analyser; Figure 3.2 was shown the working principle: Particle size within the range 100nm – 1000µm can be measured with an accuracy of $\pm 1\%$. The equipment was calibrated before the subsequent measurement to reduce the background spectrum. This is crucial because the scattering pattern of the incident laser beam can be influenced by impurities within the dispersant, on the windows and optics and also electrical noise. This background signal is then subtracted from the scattering pattern measured with the sample. To ensure reliable data acquisition, about 50mg of powder was ultrasonically dispersed in acetone or ethanol to avoid agglomeration of powder particles.

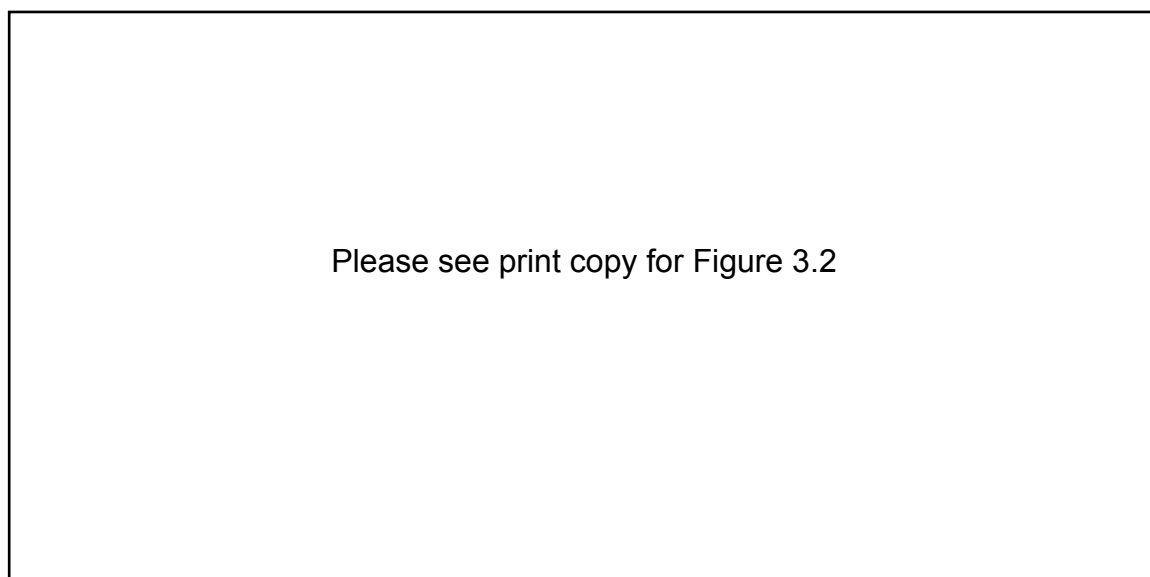


Figure 3.2 Principle about determination of the powder particle size [10]

During the measurement, a focused laser beam is passed through the particles which scatter light at an angle is inversely proportional with the powder size. The light

scattered at different angular intensity will then be caught by a series of photosensitive detectors. So, it is possible to calculate the particle size distribution based on the recorded intensity of scattered light as a function of angle. The map of scattering intensity versus angle is the primary source of information used to calculate the particle sizes. The average particle size of the powder could also be obtained [9, 10].

In this study, we measure the Boron powder in different place with different machine in Korean (Mastersizer 2000), and China (JL-1166 Laser Particle Sizer).

3.2.2 X-ray Diffraction (XRD)

X-ray diffraction was performed in the step-scanning mode $\theta - 2\theta$ by using a Philips PW1730 diffract meter with Cu-K α radiation source ($\lambda = 1.5418 \text{ \AA}$). Typically, diffraction data was collected from $10^\circ - 105^\circ$ in a step width of 1° and counting time per minute. The incident x-rays are reflected by the crystal plane at angle θ with respect to the incident ray. Consequently, a reflected ray is generated at an angle 2θ from the incident beam. In the $\theta - 2\theta$ configuration, the x-ray tube is fixed, the sample is moved by θ while the collector is moved by 2θ simultaneously as shown in Figure 3.3 below.

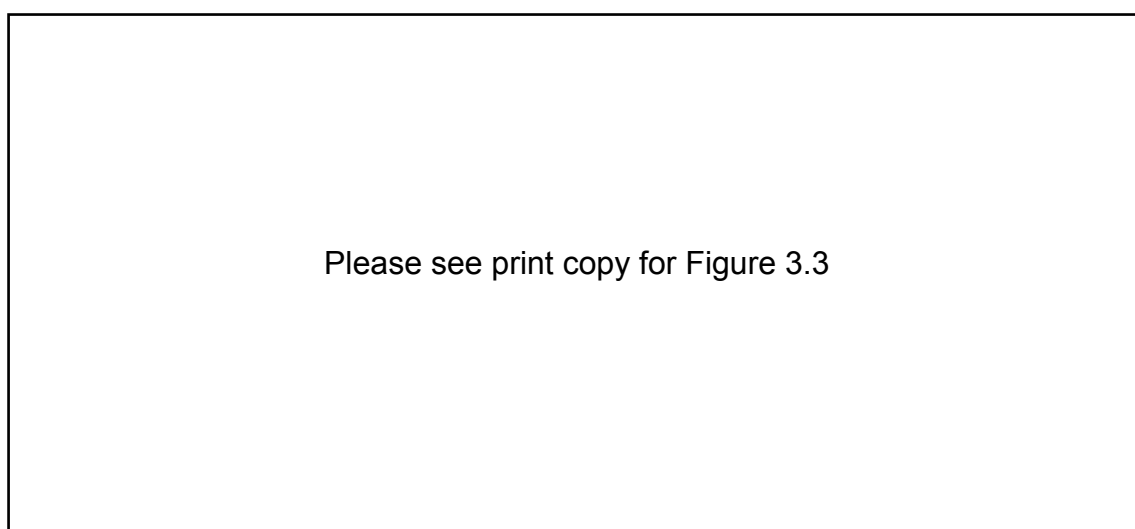


Figure 3.3 X-ray diffract meter in $\theta - 2\theta$ configuration taken from reference [11]

Diffraction will occur whenever the Bragg's Law is satisfied

$$n\lambda = 2d\sin\theta \quad (3.1)$$

n = integer, λ = wavelength, d = lattice spacing, θ = angle.

Rietveld refinement analysis was used to obtain the cell parameters with the estimated errors. Semi-quantitative phase analysis was carried out by using TRACES™ software; Profit to obtain information of peak position (2θ), intensity, full width half maximum (FWHM) and integral breadth. On the basis of Lorentzian peak profile, the contribution of grain size, L and micro strain, ε to the peak broadening can be estimated from the Williamson-Hall plot [12]:

$$\beta\cos\theta = 4\varepsilon\sin\theta + \lambda/L \quad (3.2)$$

in which β is FWHM in radians and λ is the wavelength. For a particular sample, L and ε can be obtained from the corresponding y -axis intercept and slope respectively by performing least-square fitting to a $\beta\cos\theta$ versus $\sin\theta$ plot.

According to Avdeev *et al*, results [13], the level of C substitution, x in the formula $\text{Mg}(\text{B}_{1-x}\text{C}_x)_2$, can be estimated as:

$$x = 7.5 \times \Delta(c/a) \quad (3.3)$$

where $\Delta(c/a)$ is the change in c/a compared to a pure sample, because it tends to be independent from diffractometer calibration errors.

3.2.3 Differential Thermal Analysis (DTA)

Differential Thermal Analysis (DTA) is defined formally as a technique for recording the difference in temperature between a substance and a reference material against

either time or temperature as the two specimens are subjected to identical temperature regimes

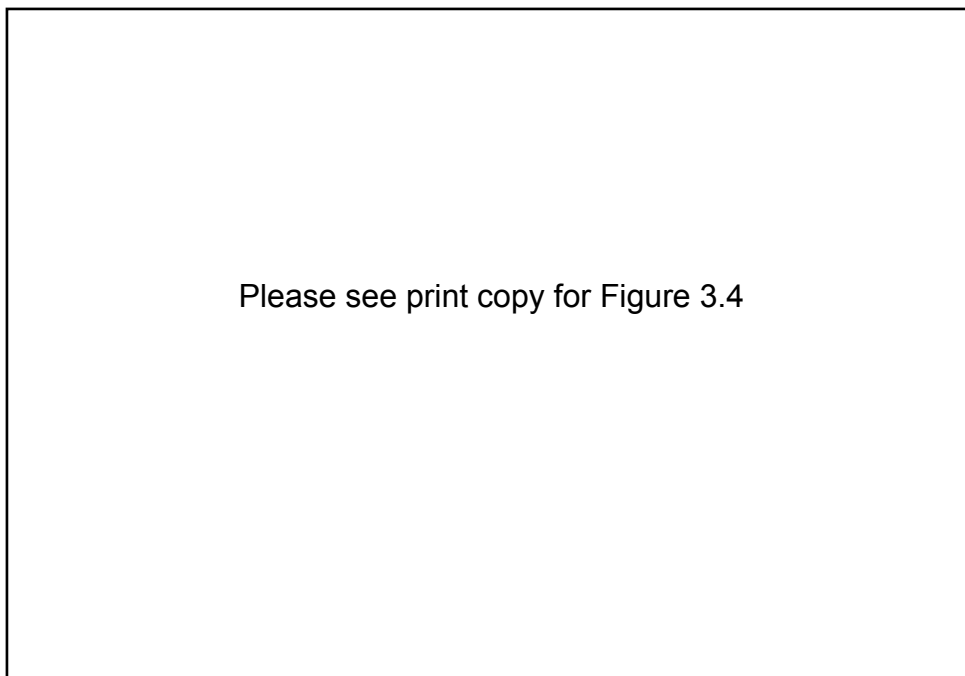


Figure 3.4 Schematic illustration of a DTA cell [14].

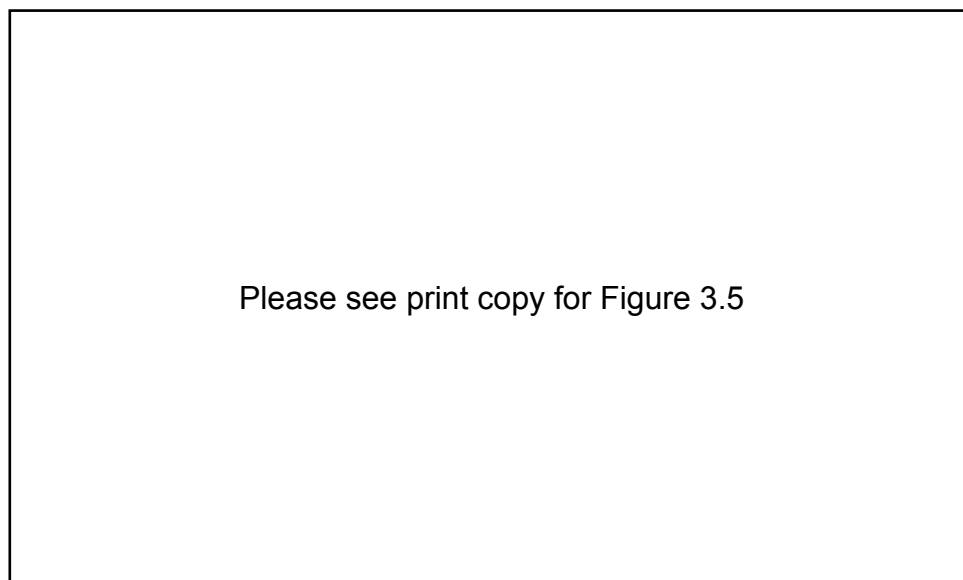


Figure 3.5 A typical DTA result of a sample with endothermic and exothermic reactions [14].

in an environment heated or cooled at a controlled rate. It involves heating or cooling a test sample and an inert reference under identical conditions, while recording any temperature difference between the sample and reference. This differential temperature

is then plotted against temperature. Changes in the sample which lead to the absorption (endothermic) or evolution (exothermic) heat can be detected relative to the inert reference. Image is shown in Figure 3.4. From DTA, the martial composing temperature and time can be computed. The crucibles used were alumina, and the sample mass was in the range of 50 mg. The system has a temperature ramp rate range of 0.1 to 50°C/min. Argon gas was used for all the results presented with a constant flow rate of 50 ml/min.

The baseline of the DTA curve should then exhibit discontinuities at the transition or reaction temperatures as shown in Figure 3.5 and the slope of the curve at any point will depend on the microstructure at that temperature. If the reaction proceeds at a rate varying with temperature, the position of the peak varies with the heating rate if other experimental conditions are maintained fixed.

3.2.4 Scanning electron microscopy (SEM), Energy dispersive X-ray spectrometry (EDS), and Transmission electron microscopy (TEM)

In this work, two kinds of facilities were used: JOEL 2011 analytical electron microscope with JOEL EDS system at University of Wollongong, Australia and Phillips CM 200 Field Emission Gun Transmission Electron Microscope at University of New South Wales, Australia .

3.2.5 Brunauer-Emmett-Teller (BET)

The surface area and pore structure of Boron powder were analysed by NOVA 1000 high-speed gas desorption analyser using BET method [17]. The data calculated were based on nitrogen desorption isotherm at liquid nitrogen temperatures and the software provided by NOVA.

3.2.6 Measurements of T_c , J_c , H_{c2} , H_{irr}

3.2.6.1 Critical temperature (T_c)

T_c of the superconducting materials can be determined by using a) the resistance measurement, or b) the magnetic AC susceptibility measurement. Both of the measurements were carried by a Quantum Design Physical Property Measurement Systems (PPMS).

- a) The resistance measurement requires the sample to be contacted with four leads. The two outer leads are for current and the two inner leads are for voltage, which also can determine the resistivity of MgB_2 samples from room temperature to superconducting temperature by using this method with sensitivity up to $1\mu\Omega$.
- b) On the second way, that T_c was defined as the onset of the diamagnetism by measuring the real part of the ac susceptibility with a sensitivity of up to 10^{-8} emu. the sample is located in a system consisting of a primary and secondary coil. The primary coils produce an excitation field set to amplitude of 0.1 Oe and frequency of 117 Hz. The sample is placed in the secondary pick-up coils, where the change of the induction voltage across the coils due to the superconducting shielding current can be measured by the Lock-In Amplifier.

3.2.6.2 Critical current density (J_c)

The critical current density (J_c) can be determined by a) the transport method (J_{ct}) or b) the DC magnetization measurement (J_{cm}).

a) the transport critical current density (J_{ct})

The critical current, I_c , was measured by a conventional four point-probe resistive method at 4.2 K in magnetic field below 12 T. Current leads and voltage taps is directly connected to the sheath materials of the wire. The maximum current of power supply was 1000 A and a nano-volt meter was used to detect the signal of sample. A magnetic field was applied parallel to the wire. The criterion of I_c definition was 1 μ V/cm. The transport critical current density, J_{ct} , was calculated by dividing I_c by the cross-sectional area of the MgB₂ core.

b) the magnetic critical current density (J_{cm})

DC magnetization is measured by using the Quantum Design Physical Property Measurement System (PPMS). The sample is moving in a constant magnetic field and the waveform signal from the sample is detected up by detection coil. The signal is then fitted with the known calibration waveform, where the magnetic moment of the sample is a fitting parameter. The magnetic hysteresis loop is measured over a temperature range of 5 to 30 K in a time-varying magnetic field with sweep rate 50Oe/s and from 0 to 8.5T. J_c can be calculated from the measured magnetic hysteresis loop based on the Bean Model [18], as shown below.

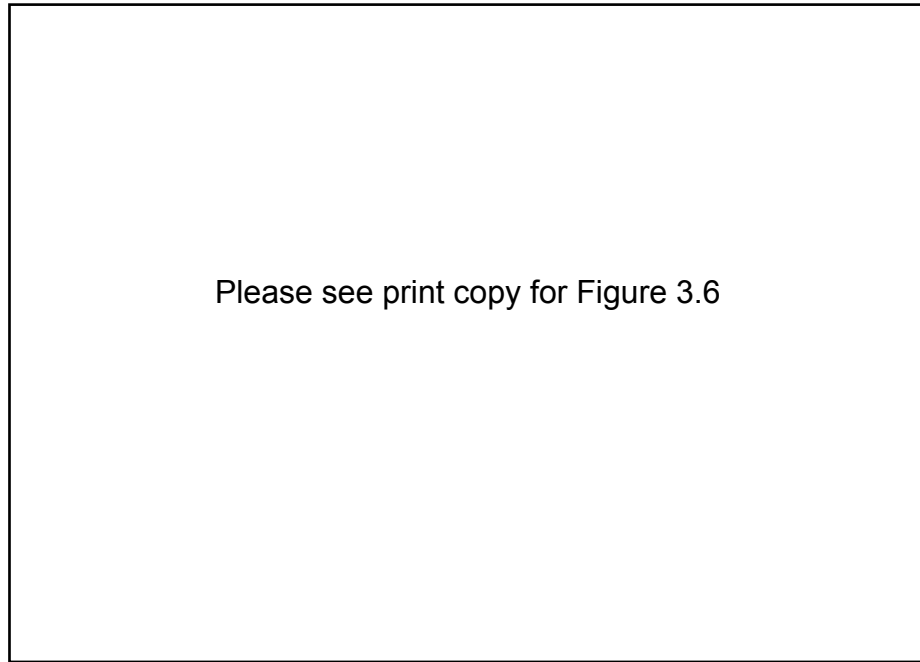
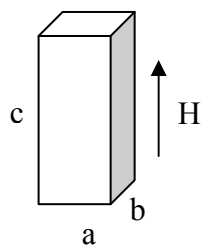


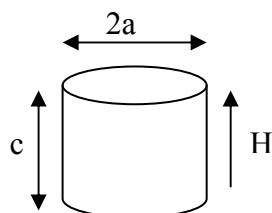
Figure 3.6 Schematic diagram of magnetic hysteresis loop of a superconductor showing the width of the magnetic hysteresis loop ΔM [18].

For bar shape ($b > a$)

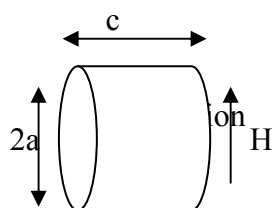


$$J_{cm} = 20 \Delta M / [a(1 - a/3b)]$$

For cylinder shape (diameter $2a$)



$B \parallel \text{axis}$
 $J_{cm} = 15 \Delta M / [a^3 c \pi]$



$B \perp \text{axis}$
 $J_{cm} = 15 \Delta M / [4a^3 c]$

Figure 3.7 Magnetic hysteresis measured on a bulk MgB_2 at 6K up to 7T. The flux jumping is due to thermomagnetic instabilities causing a sudden dissipative re-arrangement of magnetic flux lines [19].

With bar samples, a, b and c are the dimensions of sample in cm. J_{cm} and ΔM are in A/cm^2 and in emu/cm^3 , respectively. Bar shaped samples ($3 \times 2 \times 1 \text{ mm}^3$) and wire shaped samples ($c=200 \text{ mm}$, $a=0.8-0.9\text{mm}$) were cut from each pellet and peeled out from the wire for magnetic measurements. The low field J_{cm} below 10 K could not be measured due to flux jumping, which has shown in Figure 3.7.

3.2.6.3 Difference between J_{ct} and J_{cm}

- The transport critical current density (J_{ct}) is the real useful J_c that flows through the whole of the sample, the magnetic critical current density (J_{cm}) overestimate the real J_c at low fields, whereas they underestimate it at high fields[20].
- The difference between J_{cm} and J_{ct} in MgB_2 is related to the microstructure of the superconducting MgB_2 core. There are superconducting screening currents flowing on different length-scales due to sample porosity and agglomeration of superconducting crystals [21].
- Some simulations show that major defects in the superconducting core will affect on the difference of J_{cm} and J_{ct} [22], therefore, MgO as the main secondary phase will be great importance in negative effect for the J_{ct} .

3.2.6.4 The upper Critical field (H_{c2}) and the irreversibility Field (H_{irr})

H_{c2} and H_{irr} value is determined by using two methods: a) the resistivity versus temperature or b) the ac susceptibility versus temperature measurements. Both measurements are carried out by using Quantum Design PPMS system, with fields up to 8.7 T.

- a. For the resistivity method, H_{c2} and H_{irr} are estimated by measuring from the temperature at which the normal-state resistivity of the sample drops by 10% and 90% of its normal state value, respectively, as a particular field.
- b. For the magnetization measurements, the H_{c2} is estimated from the onset of diamagnetic screening for a particular field, and assume a criterion of $J_{cm} = 100 \text{ A cm}^{-2}$ to estimate the H_{irr} at particular measuring temperature.

3.3 References

1. M. Atzmon Atzmon, *Phys. Rev. Lett.* **64** 487-490, (1990).
2. P. P. Chattopadhyay, I. Manna, S. Talapatra, and S. K. Pabi, *Mater Chem Phys* **68** 84-94, (2001).
3. Y. S. Kwon, K. B. Gerasimov, and S. K. Yoon, *Journal of Alloys and Compounds* **346(1)** 276-281, (2002).
4. G. B. Schaffer, and J. S. Forrester, *Journal of Materials Science* **32** 3157-3162, (1997).
5. M. Simoneau, G. L'Esperance, M. L. Trudeau, and R. Schulz, *J. Mater. Res.* **9(3)** 535-540, (1994).
6. B. Q. Zhang, L. Lu, and M. O. Lai, *Physica B* **325** 120-129, (2003).
7. G. Ziegler, *Powder Metall Int* **10** 70-73, (1978).
8. <http://www.fritsch.de/en/sample-preparation/products/milling/planetary-mills/>
9. G. Mie, *Ann. d. Physik* **25** 377, (1908).
10. L. Kai, and A. d'Alessio, *Particle and Particle Systems Characterization* **12** 119-122, (1995).
11. B. D. Cullity, and S. R. Stock S R, *Elements of X-Ray Diffraction* **3rd ed** 187, (2001).
12. G. K. Williamson and W. H. Hall, *Acta Metall* **1** 22-31, (1953).
13. M. Avdeev, J. D. Jorgensen, R. A. Ribeiro, S. L. Bud'ko and P. C. Canfield *Physica C* **387** 301-6, (2003).
14. H. K. D. H. Bhadeshia, *Steels: Microstructure and Properties* **2nd ed** Lightning Source Inc., (1971).
15. S. Brunauer, P. H. Emmett, and E. Teller, *J. Am. Chem. Soc.* **60** 309, (1938).
16. C. P. Bean, *Rev. Mod. Phys.* **36** 31-36, (1964).
17. T. P. Sheahen, *Introduction to High-Temperature Superconductivity* New York: Plenum Press pp 359, (1994).
18. J. Horvat, W. K. Yeoh, J. H. Kim, and S. X. Dou, *Supercond. Sci. Technol.* **21** 065003, (2008).

19. J. Horvat, S. Soltanian, X. L. Wang, and S. X. Dou, *Appl. Phys. Lett.* **84** 3109, (2004).
20. E. Bartolome, F. Gömory X. Granados, T. Puig, and X. Obradors, *Supercond. Sci. Technol.* **18** 388, (2005).

Chapter 4: Different Media Effect for the MgB₂ Bulk Sample by Ball Milled High Purity Boron

4.1 Introduction

The discovery of the superconductivity of MgB₂ with a critical temperature of 39 K has offered the promise of important large-scale and electronic device applications at around 20 K [1]. A significant enhancement in the J_c of MgB₂ has been achieved through chemical doping with carbon (C) containing compounds, such SiC, C, B₄C, and carbon nanotubes (CNTs). However, the doping effects have been limited by the agglomeration of nanosized dopants and poor reactivity between boron (B) and C [2–7]. Moreover, the self-field and low-field J_c were depressed due to the decrease in the superconducting volume. To improve these properties, various methods have been reported. They include, for example, a ball-milling method [8, 9], a thermo-mechanical processing method [10], and the use of MgH₂ powder instead of Mg [11]. Among them, the ball-milling method is particularly interesting, as size control of the starting material may induce more effective pinning without any dopants. Specifically, the properties of the B powder, such as purity and size, may play an important role in determining the final properties of the MgB₂ [12]. This is because melting Mg can be diffused into B powder to form MgB₂ phases during sintering.

Fischer *et al* fabricated MgB₂ wires and bulks by a mechanical alloying method [10]. They obtained one of the highest J_c values without any other elements added. The very fine-grained nanocrystalline microstructure of the superconducting phase seems to be responsible for the excellent J_c values (1×10^5 A cm⁻² at 2.1 T and 20 K). Fang *et al*

fabricated MgB₂/Fe tapes via the powder-in-tube method using an ultra-fine Mg and B precursor mixture prepared by high-energy ball milling. The J_c was estimated to be $2.0 \times 10^5 \text{ A cm}^{-2}$ at 20 K and 0.6 T, and $1.1 \times 10^5 \text{ A cm}^{-2}$ at 1.5 T [8]. Kondo *et al* reported that the magnetic J_c of MgB₂ depended on the different inert gases, Ar and H₂, that were used during ball milling [9]. However, there has been no systematic study of the effects of different ball-milling media, such as acetone (C₃H₆O), ethanol (C₂H₆O), and toluene (C₇H₈). It is these liquid media that help to make mixing homogeneous. On the other hand, these media consist of carbon (C), oxygen (O), and hydrogen (H), so that the O can easily react with Mg and B to form MgO and B₂O₃ during the drying process after ball milling. In our study, therefore, we evaluated the effects of ball-milled B powders that were produced using different media, such as acetone, ethanol, and toluene, on the superconducting properties of MgB₂. The lattice parameters, J_c , T_c , and microstructure are presented in comparison with reference pure MgB₂.

4.2 Sample Preparations

MgB₂ pellets were prepared by an *in situ* reaction process. B powders (99%) were prepared in different ball-milling media, such as acetone, ethanol, and toluene (with the samples named after the corresponding medium). The ball-milling process was carried out for 4 h with a rotating speed of 160 rpm under air. These three kinds of B powders were mixed, ground, and pressed with Mg (99%) powder. All samples were sintered at 650 °C for 30 min under high-purity argon gas. The heating rate was 5 °C min⁻¹. A pure reference MgB₂ sample (referred to as pure) was also fabricated for comparison by applying the same process, except for the ball milling. All samples were characterized by x-ray diffraction (XRD) and scanning electron microscopy (SEM). The crystal structure was refined with the aid of the program FullProf[]. T_c was defined as the onset temperature at which diamagnetic properties were observed. The magnetization was measured at 5 and 20 K using a physical property measurement system (PPMS, Quantum Design) in a time-varying magnetic field with sweep rate 50 Oe s⁻¹ and amplitude 8.5 T. Since there is a large sample size effect on the magnetic J_c for MgB₂, all the samples for measurement were made to the same size (1 × 2 × 3 mm³) for comparison. The magnetic J_c was derived from the width of the magnetization loop using Bean's model [13]. J_c versus magnetic field was measured up to 8.5 T.

4.3 Phase Information and Lattice Properties

Table 4.1 shows the data measured for the pure reference MgB_2 and the ball-milled MgB_2 samples using different media. The value of the ratio of the lattice parameters c/a for all samples did not change within the limits of calculation error, suggesting that C could not substitute into B sites during ball milling. Even though the hydrocarbon media used contained C, there were no apparent substitution effects. However, it is to be noted those the a lattice parameter for the toluene sample is shorter than that of the other ball-milled samples, but according to Avdeev *et al*, results [14], the level of C substitution, x in the formula $\text{Mg}(\text{B}_{1-x}\text{C}_x)_2$, can be estimated as $x = 7.5 \times \Delta(c/a)$, where $\Delta(c/a)$ is the change in c/a compared to a pure sample, because it tends to be independent from diffractometer calibration errors. These observations were further explained by the FWHM values and refined grain sizes, to be discussed later.

Samples	FWHM (deg.)			Lattice constant		
	(100)	(110)	(002)	$a(\text{\AA})$	$c(\text{\AA})$	c/a
pure	0.4300	0.4860	0.4940	3.0848(1)	3.5298(1)	1.1442(1)
Toluene	0.4640	0.6800	0.6800	3.0812(4)	3.5244(2)	1.1438(3)
Ethanol	0.3620	0.4700	0.4700	3.0843(4)	3.5292(3)	1.1442(3)
Acetone	0.3440	0.4560	0.4960	3.0830(3)	3.5258(2)	1.1436(2)

Table 4.1 The full-width at half maximum (FWHM) of 3 main peak positions and lattice parameters for the MgB_2 samples made with and without ball milling in various media.

The XRD patterns for all samples are shown in Figure 4.1. The XRD measurements were performed on the ground MgB_2 pellets. It was observed that all samples seemed to be well developed MgB_2 with small amounts of MgO. There were no visible differences in this respect between the samples. From the XRD results, the FWHMs of the (100), (002),

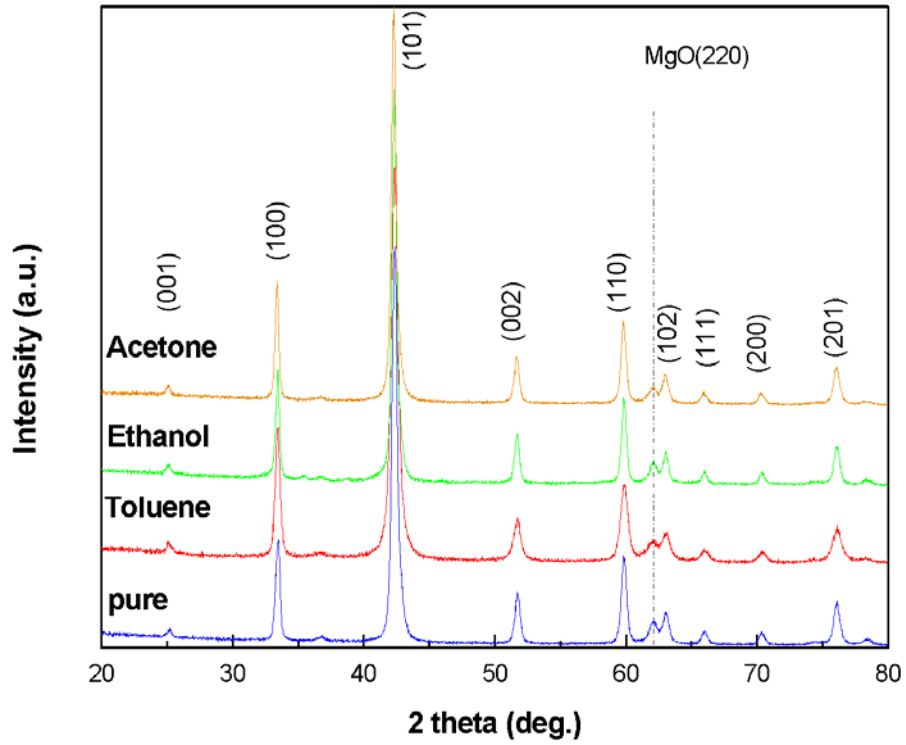


Figure 4.1 The X-ray diffraction patterns for the MgB_2 samples made with and without ball milling in various media.

and (110) peaks were evaluated as listed in Table 4.1. It is to be noted that the FWHMs of the 3 main peak positions for the toluene sample were much larger. This significant broadening of the (002) and (110) peaks can be explained by depression of crystallinity due to ball milling. According to the Scherrer equation, an increased FWHM value also indicates that the grain size has decreased as follows:

$$D_p = 0.94\lambda / \beta_{1/2} \cos \theta$$

where D_p is crystal size, λ is wavelength, $\beta_{1/2}$ is FWHM, and θ is peak position. From this equation, crystal size is easily calculated as a function of peak width (FWHM). This approach does, however, neglect the effect that strain can have on crystallite size [15]. As a result, broadening FWHM values may be due to ball milling with different media. Yamada *et al.* reported that a small MgB_2 grain size was effective in enhancing flux

pinning because the grain boundaries of MgB_2 represented effective pinning centers, as in the case of A15 metallic superconductors [16].

4.4 SEM Studies

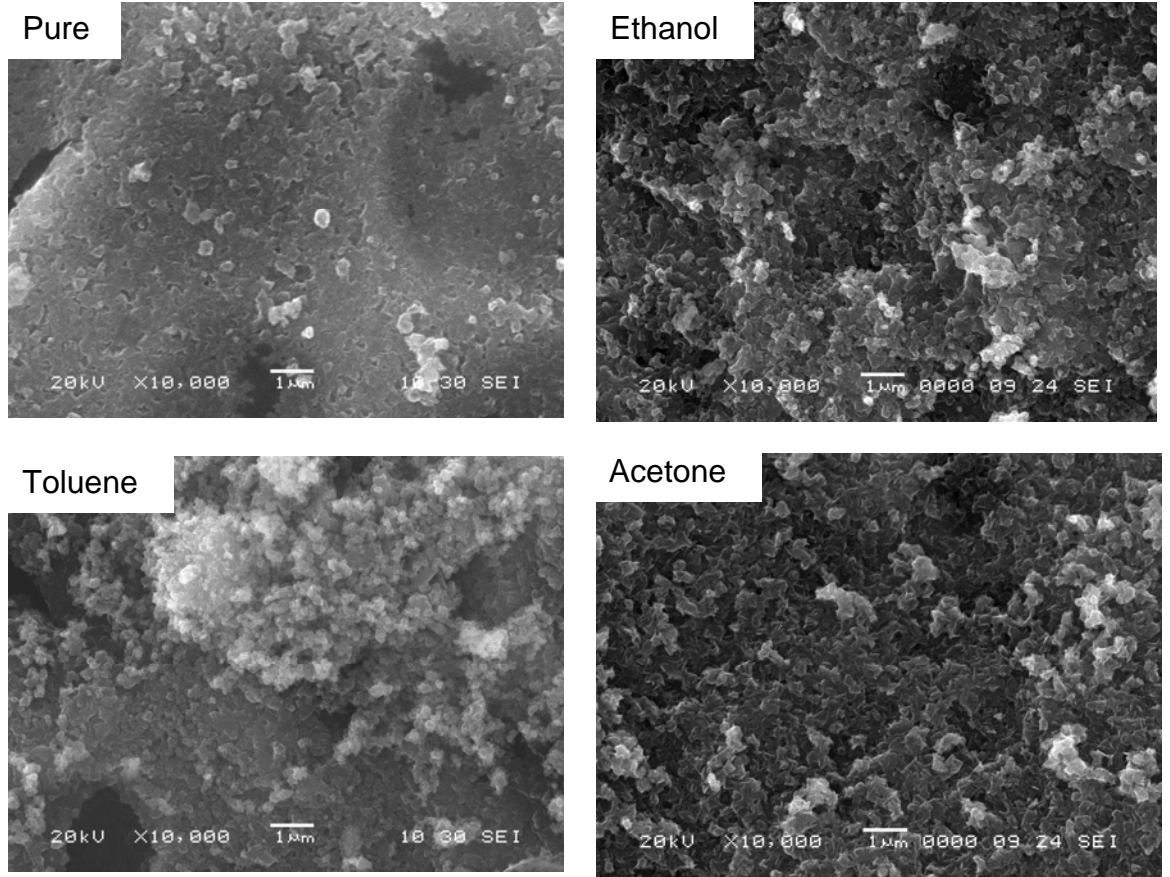


Figure 4.2 SEM images for the MgB_2 samples.

Figure 4.2 shows SEM images for all samples sintered at 650°C for 30 min. It was observed that the specimens consisted of quite well consolidated material. The grain size of the material is quite small, around 100-300 nm. Specifically, the grain sizes of the ethanol and acetone samples are larger than for the pure reference sample (~ 200 nm), while the grain size of the toluene sample was slightly smaller (~ 100 nm). It is to be noted that the reference sample has better grain homogeneity, but the toluene sample seems to have enhanced clumping of fine particles into coral-like agglomerates due to ball-milling effects. The different behaviours of $J_c(B)$ and T_c can be attributed to this

microstructural difference. Since melting Mg is diffused into B powder to form MgB_2 phases during sintering, $J_c(B)$ properties can be related to the B powder properties.

4.5 Inference on J_c and T_c

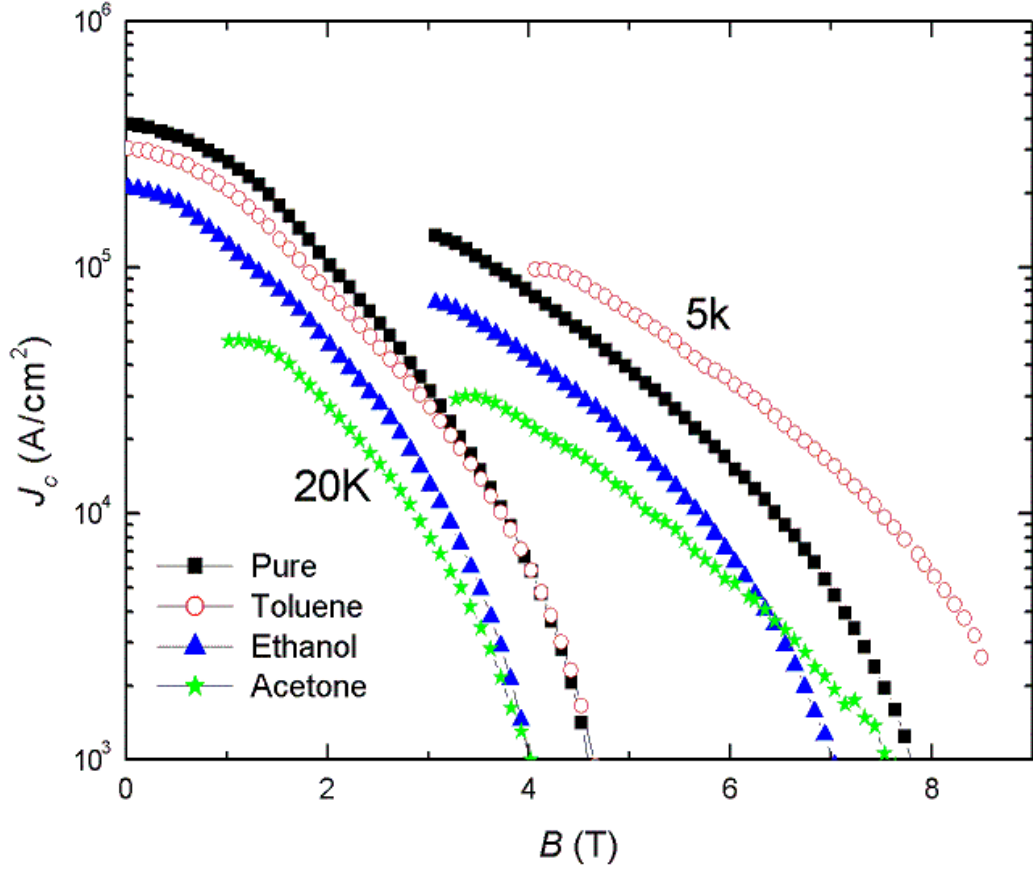


Figure 4.3 The magnetic critical current density J_c as a function of field for the MgB_2 samples.

Figure 4.3 shows the magnetic field dependence of J_c for all samples at 5 and 20 K. We observe that the J_c value of toluene sample was estimated to be $5 \times 10^3 \text{ A/cm}^2$ at 8 T and 5 K. This value is comparable to those of chemically doped samples under high field. The J_c value is much higher than that of the pure MgB_2 made without any ball-milling process, by a factor of 20. Using ball milled B with toluene as the ball-milling medium was a highly effective method to enhance the $J_c(B)$ performance under high field. This is because toluene can prevent the oxidation of B powder during ball milling, and the small grain size is effective for enhancing flux pinning at the grain boundaries, which

represent effective pinning centers. However, at 20K, the $J_c(B)$ performance of the toluene sample value is slightly lower than that of the reference MgB_2 sample. This is probably because the ball-milled sample had poor grain connectivity. This observation is further supported by the FWHM and SEM results (Table 4.1 and Figure 4.2).

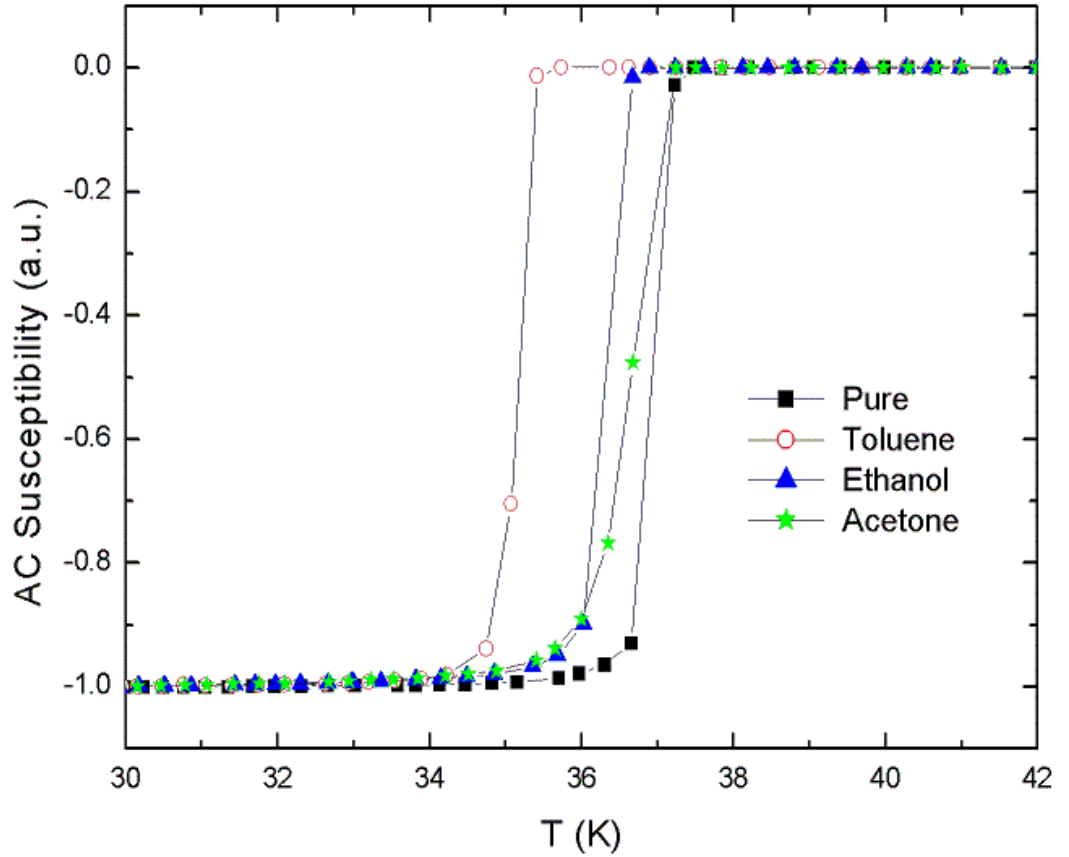


Figure 4.4 The T_c curves for the MgB_2 samples.

The critical temperature (T_c) for all samples is presented in Figure 4. T_c of the reference MgB_2 was higher than that of the ball-milled samples. This is related to the improvement of crystallinity of the MgB_2 superconductor. It is to be noted that the T_c variations of the ball-milled samples are significantly different for the different media. In addition, T_c of the toluene sample was slightly lower than for the acetone and ethanol samples. For example, the T_c value of the toluene sample was 35.7 K, while the corresponding values for the acetone and ethanol samples were 37.2 K and 36.8 K,

respectively. This depressed result for the toluene sample is considered to be due to its poor crystallinity, resulting in a significant amount of strain and crystal defects in the sample after ball milling.

4.6 Summary

We evaluated the effects of ball-milled B powders using different media, such as acetone, ethanol, and toluene, on the superconducting properties of MgB₂. It was observed that the a and c lattice parameters did not significantly change for any of the samples, suggesting that C could not substitute into B sites during ball milling. Specifically, ball-milled B using toluene leads to smaller MgB₂ grains, resulting in enhanced J_c under high field. The estimated J_c was 5×10^3 A/cm² at 8 T and 5 K. This value is much higher than that of the pure reference MgB₂, by a factor of 20. At 20K, however, the $J_c(B)$ performance of the toluene sample is slightly worse than for the pure sample. This depressed value is probably related to the poor crystallinity. Further studies on the ball-milling process promise to allow adjustment of the desired phase form, such as for MgB₂ made with low grade boron powder via solid state reaction for future applications.

4.7 References

16. J. Nagamatsu, *Nature* **410** 63-64, (2001).
17. S. X. Dou, S. Soltanian, J. Horvat, X.L. Wang, S.H. Zhou, M. Ionescu, H.K. Liu, P. Munroe, and M.Tomsic, *Appl. Phys. Lett.* **81** 3419, (2002).
18. J. H. Kim, W. K. Yeoh, M. J. Qin, X. Xu, and S. X. Dou, *J. Appl. Phys.* **100** 013908, (2006).
19. W. K. Yeoh, J. H. Kim, J. Horvat, X. Xu, M. J. Qin, and S. X. Dou, *Supercond. Sci. Technol.* **19** 596-599, (2006).
20. R. A. Ribeiro, S. L. Bud'ko, C. Petrovic, and P. C. Canfield 2003 *Physica C* **384** 227, (2003).
21. W. Mickelson, J. Cumings, W. Q. Han, and A. Zettl, *Phys. Rev. B* **65** 052505, (2002).
22. Akiyasu Yamamoto *et al.*, *Supercond. Sci. Technol.* **18** 1323-1328, (2005).
23. H. Fang, S. Padmanabhan, Y. X. Zhou, and K. Salama, *Appl. Phys. Lett.* **82** 4113-4116, (2003).
24. T. Kondo, P. Badica, Y. Nakamori, S. Orimo, K. Togano, G. Nishijima, and K. Watanabe, *Physica C* **426-431** 1231-1237, (2005).
25. C. Fischer, C. Rodig, W. Hassler, O. Perner, J. Eckert, K. Nenkov, G. Fuchs, H. Wendrock, B. Holzapfel, and L. Schultz, *Appl. Phys. Lett.* **83** 1803, (2003).
26. T.Nakane, H.Fujii, A.Matsumoto, H.Kitaguchi, and H.Kumakura, *Physica C* **426-431** 1238-43, (2005).
27. X. Xu, M. J. Qin, K. Konstantinov, D. Dos Santos, W. K. Yeoh, J. H. Kim and S. X. Dou, *Supercond.Sci.Technol.* **19** 466-469, (2006).

28. C. P. Bean, *Rev. Mod. Phys.* **36** 31, (1964).
29. M. Avdeev, J. D. Jorgensen, R. A. Ribeiro, S. L. Bud'ko and P. C. Canfield
Physica C **387** 301–6, (2003)
30. S. Calvin, M. M. Miller, R. Goswami, S. F. Cheng, S. P. Mulvaney, L. J. Whitman,
and V. G. Harris, *J. Appl. Phys.* **94** 778, (2003).
31. H. Yamada, M. Hirakawa, H. Kumakura and H. Kitaguchi, *Supercond.*
Sci.Technol. **19** 175-177, (2006).

Chapter 5: Influence of Ball-milled Low Purity Boron Powder on the Superconductivity of MgB₂ Bulk sample

5.1 Motivation and Scope

To further improve the J_c , the properties of the starting B powders, such as purity, particle size, etc., may also play an important role in determining the superconducting properties of MgB₂. It has been found that samples made from crystalline B powders have around an order of magnitude lower J_c than samples made from amorphous B [1]. Moreover, various methods have been reported to improve the self-field and low-field J_c , among them, the ball-milling method is particularly interesting, as size control of the starting material may induce more effective pinning without any dopants, as also in our previous work where we evaluated the effects of ball-milled B powders that were produced using different ball-milling media, such as acetone, ethanol, and toluene, on the superconducting properties of MgB₂ [2].

Furthermore, in practical applications, the cost of the materials must be considered. Pure (99%) amorphous B powder is about 10 times more expensive than low-grade 96% powders with crystalline phase. If the 96% B powders can be used to make MgB₂, the material cost could be decreased significantly.

In this work, we evaluated the particle size, which has effects on the superconducting properties of MgB₂, when we used 96% B powder with crystalline phase as a precursor after ball milling in a toluene medium. The lattice parameters, grain size, strain, J_c , and T_c are presented in comparison with reference MgB₂ made from commercial 96% B.

5.2 Experimental Detail

MgB₂ pellets were prepared by an *in-situ* reaction process. B powders (96% crystalline) were prepared by ball milling, using toluene as a medium. The ball-milling process was carried out for 4 hrs or 12 hrs with a rotation speed of 160 rpm under air, and then the powder was dried in a vacuum oven.

The three kinds of B powders (commercial 96% and the ball- milled 96% with different ball-milling times, 4hrs and 12hrs, identified as B96, BM4B96, and BM12B96, respectively) were measured by X-ray diffraction (XRD) and scanning electron microscopy (SEM).

Then these powders were mixed, ground, and pressed with Mg (99%) powder. Some MgB₂ using B96 was sintered at 800°C for 30min as a reference, and other MgB₂ samples using BM4B96 and BM12B96 were sintered at 650°C, 800°C and 900°C for 30 min under high purity argon gas. These MgB₂ samples are identified as B96S800, BM4B96S650, BM12B96S650, BM12B96S800, and BM12B96S900, respectively. The heating rate was 5°Cmin⁻¹. All samples were characterized by X-ray diffraction (XRD). The crystal structure was refined with the aid of the program Jade 5. T_c was defined as the onset temperature at which diamagnetic properties were observed. The magnetization was measured at 5 and 20 K using a Physical Properties Measurement System (PPMS, Quantum Design) in a time-varying magnetic field with sweep rate 50 Oe/s and amplitude 8.5 T. All the samples for measurement were made to the same size (1 x 2 x 3 mm³) for comparison. The magnetic J_c was derived from the width of the magnetization loop using Bean's model. J_c versus magnetic field was measured up to 8.5 T.

5.3 Phase Information and Microstructure of 96% Boron

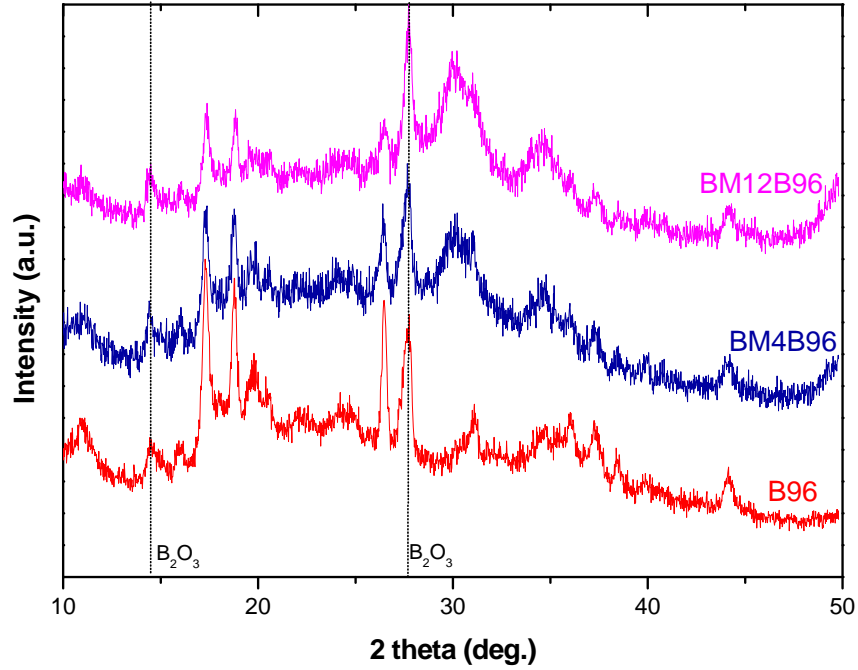


Figure 5.1 X-ray diffraction patterns for the different B powders.

Figure 5.1 shows the XRD patterns for commercial 96% and for the ball-milled 96% B powders. We observed that there were B_2O_3 peaks ($2\theta \sim 14.6^\circ$ and 27.8°) in all the powders. Even when we carried out the ball-milling process for 12 hr, the B_2O_3 still remained in the 96% B powder. There were no visible differences in the B_2O_3 intensity. Jiang et al. [3] have reported that B_2O_3 may wet the MgB_2 grain boundaries and react with Mg to form MgO , resulting in depression of the J_c . There was a particularly strong crystalline response in the as-supplied 96% B powders. This phase is believed to require high temperature for a full reaction between Mg and B, and this is why we selected the B96S800 as the best reference for comparison.

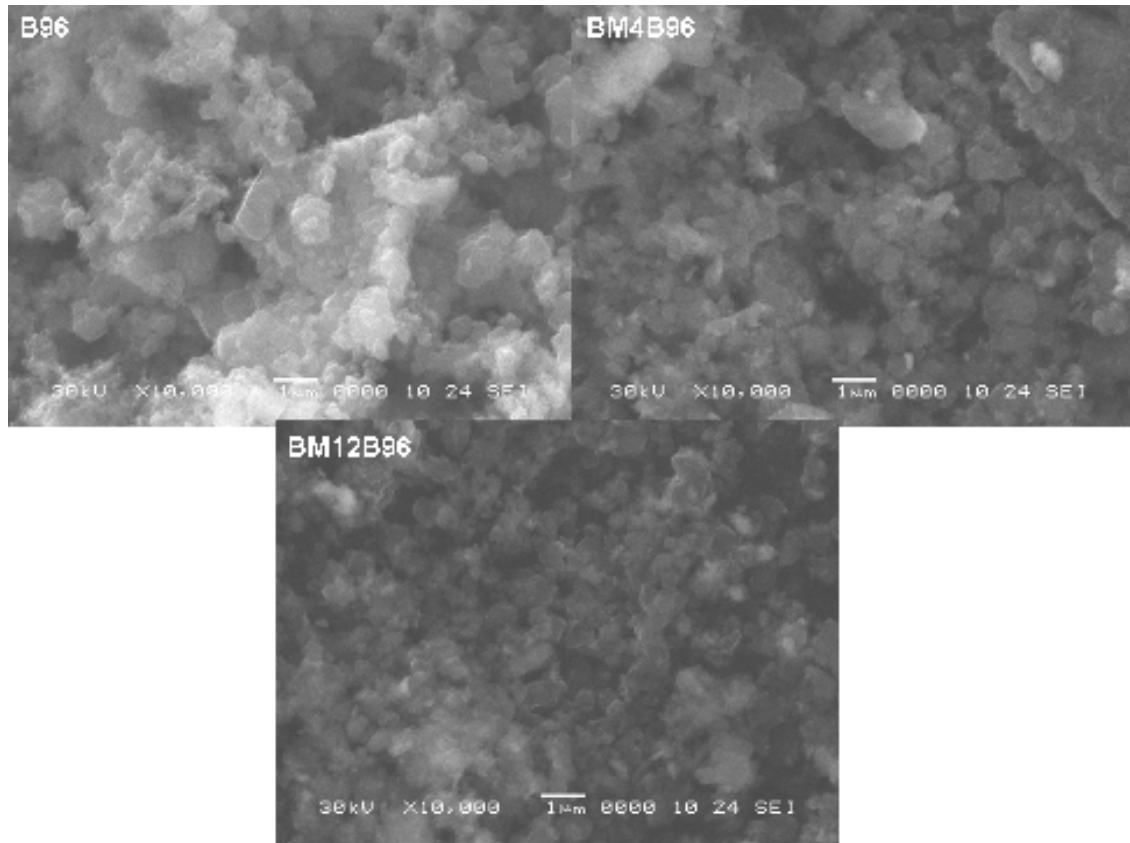


Figure 5.2 SEM images of the different B powders.

Figure 5.2 shows SEM images for (a) commercial 96% B, (b) 4 hrs ball-milled 96% B, and (c) 12 hrs ball-milled 96% B. It was observed that the particle size of the reference 96% B was approximately 1 μm . The BM12B96 powders show smaller grain size and better grain homogeneity than the original 96% B powders. The characteristics of the BM4B96 powders are between those of the original 96% and those of the BM12B96 powders. The small-sized particles are much more effective for enhancing the reaction between Mg and B. In particular, since partially melted Mg needs to diffuse into B powder to form MgB_2 phase, MgB_2 superconductivity probably depends on the B powder size as well as on the reaction between Mg and B. It is possible that miniaturization of MgB_2 grains acts to improve the grain boundary pinning[4-6], as we will discuss later.

5.4 Phase Information and Lattice Parameters

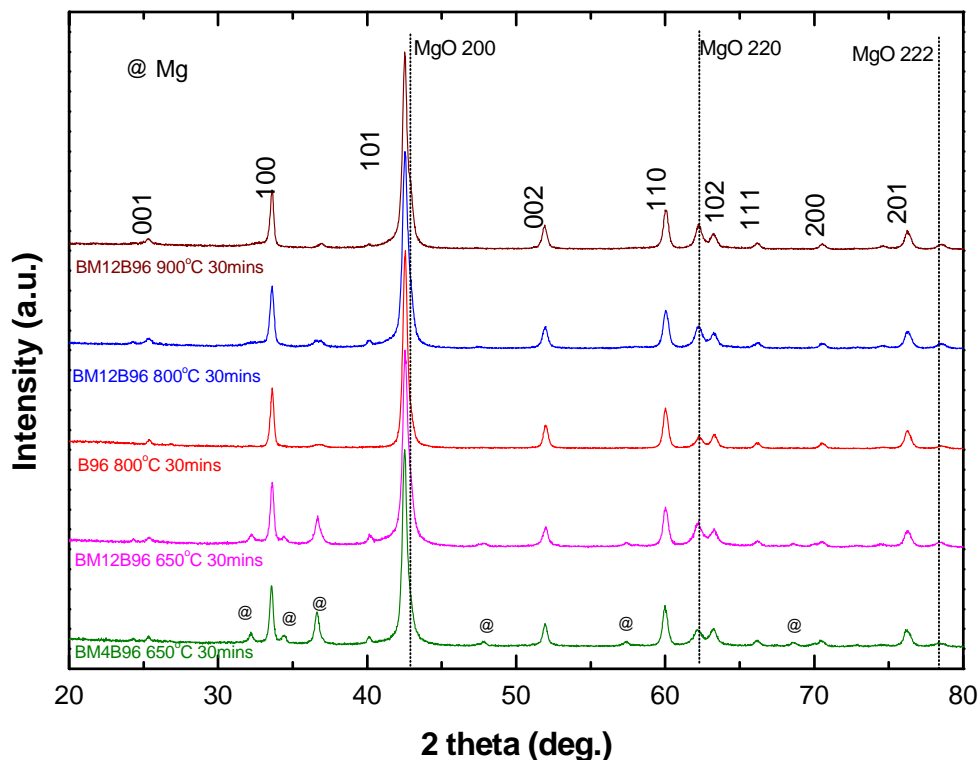


Figure 5.3 X-ray diffraction patterns for MgB_2 samples made with the different B powders

Figure 5.3 shows XRD patterns of the MgB_2 after sintering. The XRD measurements were performed on the ground MgB_2 pellets. We observed that the five kinds of samples all seemed to be well-developed MgB_2 with MgO . Specifically, the MgO intensity increased with the ball-milling time of the B sample. There is one possible reason for this: even though we used toluene as the medium during ball milling, B can react with O to form B_2O_3 in air. During sintering the B_2O_3 can react with Mg to form MgO at around 450°C . However, it is very difficult to calculate the exact quantity of B_2O_3 from the XRD data. We need to further study the effects of B_2O_3 and MgO on the MgB_2

superconductivity. From XRD results, we also observed that the FWHM of the ball-milled B sample showed greater broadening, which can be caused by both grain size and lattice strain. We calculated the grain size and lattice strain with a Williamson-Hall plot [7]. The strain value can be calculated from the slope and the grain size from the intercept in a plot of the $\text{FWHM} \times \cos \theta$ against $\sin \theta$. The θ is the angle of the XRD peak. We supposed that the strain was isotropic so used a Lorentzian profile to fit the all XRD curves. According to Serquis *et al.* [8], there are two possible reasons for the strain broadening: one is the MgO inside the MgB_2 grains and the other lattice defects based on Mg vacancies. So, we estimated the Mg and MgO content in the samples from the peak area ratio. At the lowest sintering temperature, that means at 650°C , several peaks representing un-reacted Mg phase are found in the ball-milled B samples. The remaining Mg is related to the amount of crystalline phase B, since sufficient time is needed for the full reaction. For the BM12B96 sample, as the sintering temperature increases, the MgO content becomes higher. The fitting process demands that the Residual Error of Fit parameter is near 5-7%, so that we can obtain a comparable crystallinity value. We also calculated the a and c lattice constants for all the samples. The calculated data and T_c values are listed above in Table 5.1 for comparison. The value of the ratio of the lattice parameters c/a for all samples did not change within the limits of calculation error, suggesting that C could not substitute into B sites during ball milling. Even though the hydrocarbon media used contained C, there were no apparent substitution effects. However, it should be noted that the a lattice parameter for the BM12B96S900 sample is shorter than that of the other ball-milled samples. Nevertheless, according to Avdeev *et al.*, [9], the level of C substitution, x in the formula $\text{Mg}(\text{B}_{1-x}\text{C}_x)_2$, can be estimated as $x = 7.5 \times \Delta(c/a)$, where $\Delta(c/a)$ is the change in c/a compared to a pure sample, because it tends to be independent from diffractometer

calibration errors. Within the limits of calculation error, the lattice constants for all samples were almost the same.

Sample id.	Lattice Constants			Grain Size	Strain (%)	Crystallinity (%)	Residual Error of Fit (%)	MgO (%)	Mg (%)	T_c (K)
	$a(\text{\AA})$	$c(\text{\AA})$	c/a							
				(nm)						
B96S800	3.0850(2)	3.5290(3)	1.1439(2)	282(1)	0.3030(6)	90.33	5.12	8.98	--	37.6
BM4B96S650	3.0853(6)	3.5232(9)	1.1419(5)	281(1)	0.3013(9)	70.36	6.27	19.64	15.00	37.0
BM12B96S650	3.0855(1)	3.5275(2)	1.1433(1)	223(1)	0.3735(10)	70.69	6.89	22.67	15.88	36.7
BM12B96S800	3.0854(3)	3.5255(5)	1.1426(3)	232(1)	0.3527(9)	76.11	5.89	24.28	2.92	36.4
BM12B96S900	3.0837(4)	3.5350(8)	1.1464(4)	280(1)	0.3037(10)	92.43	4.95	25.71	--	36.7

Table 5.1 The lattice constants and structural features for the MgB_2 samples made with the different B powders.

5.5 Comparison of T_c , J_c , and Pinning Force

T_c for all samples is presented in Table 5.1. The T_c value of the samples using ball-milled 96% B was estimated to be 36.4 K to 37K, while the value for the reference sample was slightly higher than that of the comparable ball-milled sample. This increased T_c is related to the higher crystallinity. On the other hand, depressed T_c for the sample using ball-milled 96% B is considered to be due to the large amount of MgO impurity phase, with its poor crystallinity resulting from a significant amount of strain and crystal defects.

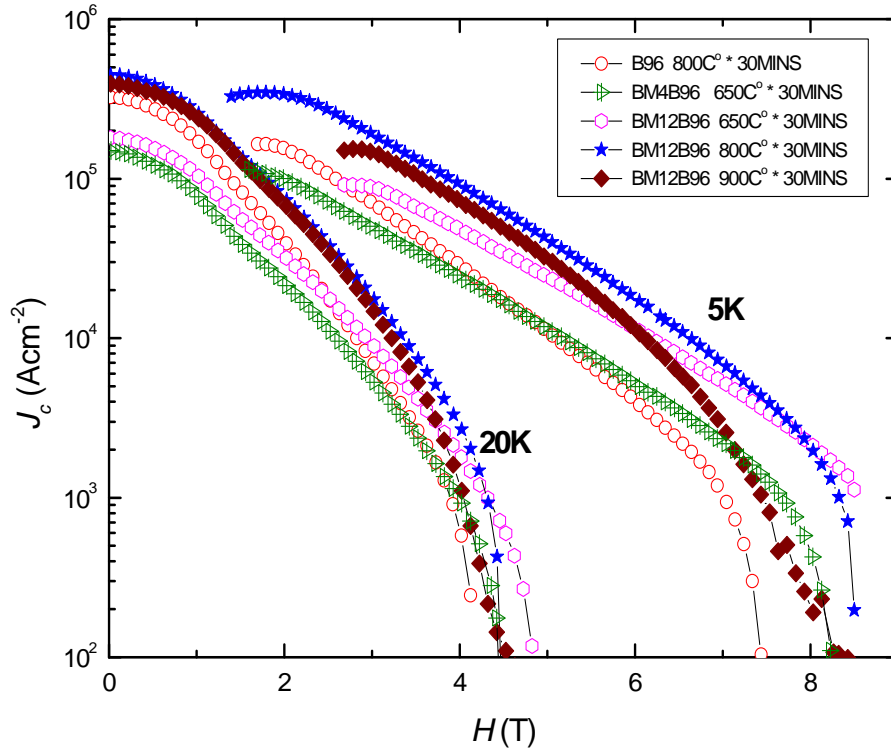


Figure 5.4 The magnetic critical current density J_c as a function of field for the MgB₂ samples.

The magnetic field dependence of J_c for all samples is shown in Figure 5.4. As can be seen in the figure, the BM12B96S800 sample made using ball-milled 96% B had a significantly higher J_c than the B96S800 sample using commercial 96% B. J_c reached $2 \times 10^3 \text{ Acm}^{-2}$ at 5 K and 8 T. We also plot the field dependence curves of the normalized volume pinning force ($F_p/F_{p,max}$) at 20K for different samples in Figure 5.5.

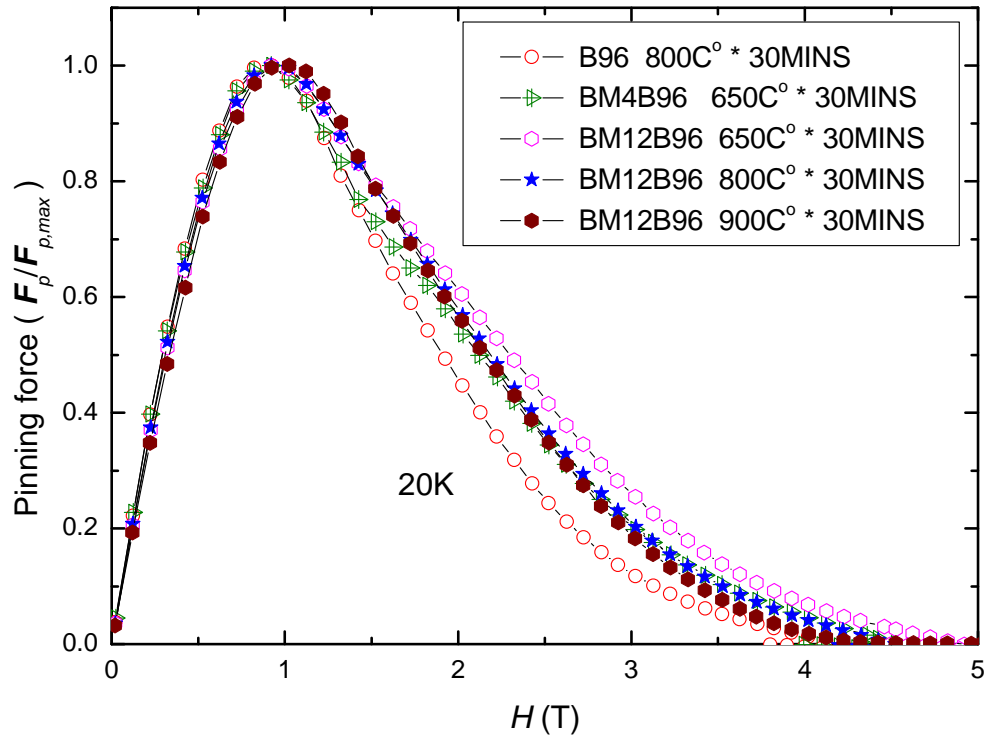


Figure 5.5 Normalized volume pinning force ($F_p/F_{p,max}$) as a function of field at 20K for the MgB₂ samples.

The improved pinning of this sample seems to be caused by enhanced grain boundary pinning provided by the large number of grain boundaries. The pinning force of the BM12B96S800 sample is larger than that of the reference B96S800 sample. The improved pinning of this sample seems to be caused by enhanced grain boundary pinning provided by the large area of grain boundaries. On the other hand, the results indicate that the highest F_p curve is obtained for the smallest grain size BM12B96S650

sample. However, the J_c performance is not just dependent on the grain size; it is also related to the purity, crystallinity, and so on. So, it suggests that keeping the balance between grain size and lattice strain can improve the superconducting properties of MgB_2 .

5.6 Summary

In summary, we have shown that the particle size of the starting B powders is important in determining the $J_c(H)$ performance of MgB_2 samples. 96% B powders can be improved by ball milling with toluene, leading to enhanced magnetic critical current densities, J_c , higher than for the original 96% B powder. It was considered that ball-milled B powder using toluene leads to smaller MgB_2 grains, resulting in enhanced J_c . Further study of the ball-milling process promises to allow adjustment of the desired phase form, for example, while reducing the grain size of MgB_2 , at the same time removing MgO phase to release the lattice strain or reducing the MgO particle size to provide pinning centres to improve J_c . MgB_2 made with low grade B powder via solid state reaction could be particularly useful for industrial applications because of the reduced material cost.

5.7 References

1. S. K. Chen, K. A. Yates, M. G. Blamire, and J. L. MacManus-Driscoll, *Supercond. Sci. Technol.* **18** 1473-1477, (2005).
2. X. Xu, J. H. Kim, W. K. Yeoh, Y. Zhang, and S. X. Dou, *Supercond. Sci. Technol.* **19** L47-50, (2006).
3. J. Jiang, B. J. Senkowicz, D. C. Larbalestier, and E. E. Hellstrom, *Supercond. Sci. Technol.* **19** L33-L36, (2006).
4. G. Giunchi¹, G. Ripamonti¹, S. Raineri¹, D. Botta, R. Gerbaldo, and R. Quarantiello, *Supercond. Sci. Technol.*, vol. **17**, S583-S588, (2004).
5. G. Giunchi, S. Ginocchio, S. Raineri, D. Botta, R. Gerbaldo, B. Minetti, R. Quarantiello, and A. Matrone, *IEEE Trans. Appl. Supercond.* **15** 3230 (2005).
6. C. E. Cybbubggan *et al.*, *Physica C* **353** 5-10, (2001).
7. G. K. Williamson and W. H. Hall, *Acta Metall* **1** 22-31, (1953).
8. A. Serquis, Y. T. Zhu, E. J. Peterson, J. Y. Coulter, D. E. Peterson, and F. M. Mueller, *Appl. Phys. Lett.* **79** 4399-4401, (2001).
9. M. Avdeev, J. D. Jorgensen, R. A. Ribeiro, S. L. Bud'ko, and P. C. Canfield, *Physica C* **387** 301-306, (2003).

Chapter 6: The Phase Transformation and Superconducting Properties of MgB₂ by Different Boron Source

6.1 Open Window for Low Purity Boron

MgB₂ play a significant role in determining its value as a replacement for conventional conductors and other low and high temperature superconducting materials. For instance, MgB₂ conductor has a very low materials cost at \$0.20 m⁻¹, which translates into \$1.00 m⁻¹ for finished strands and approximately \$1.00 kA⁻¹ m⁻¹ at 2 T and 4.2 K, based on a published report [1]. The natural abundances of Mg and B powders are also very great. Therefore, MgB₂ superconductor is one of the most promising candidates for magnet applications, when compared to Nb-Ti and Nb₃Sn, especially since its T_c of 39 K can be applied to a convenient cryogen-free magnet to work at an operating temperature of 15 - 20 K.

From the cost point of view, furthermore, high purity (> 99%) amorphous boron (B) powder is about 10 times more expensive than low purity (96-97%) B powders, which contain some crystalline phase. Eventually, low purity starting materials are expected to have a great impact on the production economics, if the low purity B powders can be applied to produce commercial MgB₂ conductors. However, there are still considerable advantages in the 99% B, i.e., amorphous B with > 99% grade has high reactivity compared to low grade 96% B, resulting in a decreased sintering temperature. To attain

the desirable properties of 99% B, the properties of the low grade B powders, such as purity, size distribution, particle size, etc., need to be well studied and systematically analyzed, as they can play an important role in determining the fundamental properties of the MgB_2 .

It is thus necessary to study sample preparation processing to achieve good superconducting properties with low purity B powder. Recently, Haessler et al [2-5] reported the best J_c result through pressure assisted sintering using a mechanically alloyed precursor powder in pristine MgB_2 and nanostructure carbon doped MgB_2 . From their result [2], it also emphasizes on the phase content, the density and the superconducting properties of MgB_2 on the choice of B precursor powder. So, we need further systematic study of ball-milling effects with our low grade B powder.

In this work, therefore, we evaluated the superconducting properties of MgB_2 made from low purity B powder with strong crystalline phase as a function of ball-milling time. We used low grade 96% commercial B powder with strong crystalline phase as our reference sample. The lattice parameters, grain size, lattice strain, J_c , critical temperature (T_c), residual resistivity ratio (RRR), upper critical field (H_{c2}), irreversibility field (H_{irr}), and microstructures for MgB_2 using ball-milled B are presented in comparison with the reference sample.

6.2 Experimental Detail

MgB₂ pellets were prepared by an *in-situ* reaction process. B powder (96%) with strong crystalline phase was prepared by ball milling, with toluene as the ball-milling medium. The ball-milling process was carried out for 4 hrs, 8hrs, and 12 hrs at a rotation speed of 160 rpm. The powder to ball ratio was 1: 16 in a planetary ball-milling with agate jar and balls. The ball sizes used were 5 mm and 10 mm, respectively. And then these powders were dried in a vacuum oven to evaporate the toluene. Four kinds of B powders were prepared, including a powder with no ball milling: these are denoted as B96, BM4B96, BM8B96 and BM12B96, respectively. These powders were then mixed, ground, and pressed with the same Mg (99%) powder. All MgB₂ samples were sintered at 800°C for 30min under high purity argon (Ar 99.9%) gas. These MgB₂ samples are again identified as B96S, BM4B96S, BM8B96S, and BM12B96S, respectively. The heating rate was 5°Cmin⁻¹. We also prepared the reference MgB₂ sample using 99% B for comparison.

The phase and crystal structure of all the samples were investigated by X-ray diffraction (XRD). The crystal structure was refined with the aid of the program Jade (ver. 5.0). T_c was defined as the onset temperature at which diamagnetic properties were observed. The magnetization was measured at 5 K and 20 K using a Physical Properties Measurement System (PPMS, Quantum Design) in a time-varying magnetic field up to 8.5 T with a sweep rate of 50 Oes⁻¹. All the samples for measurement were bar-shaped, with dimensions of 1 x 2 x 3 mm³. The magnetic J_c was derived from the width of the magnetization loop using Bean's model. Transport measurements for resistivity (ρ) were done using a standard AC four probe method. In addition, $H_{c2}(T)$ and $H_{irr}(T)$ were

defined as the fields where the temperature dependent resistance at constant magnetic field $R(H_{c2}, T) = 0.9R_{ns}$ and $R(H_{irr}, T) = 0.1R_{ns}$ with R_{ns} being the normal state resistance near 40 K. The grain morphology and microstructure were studied by scanning electron microscopy (SEM). The powder particle size and distribution were analyzed using a Mastersizer 2000 (ver. 3.01).

6.3 SEM Studies for Different Boron Powder

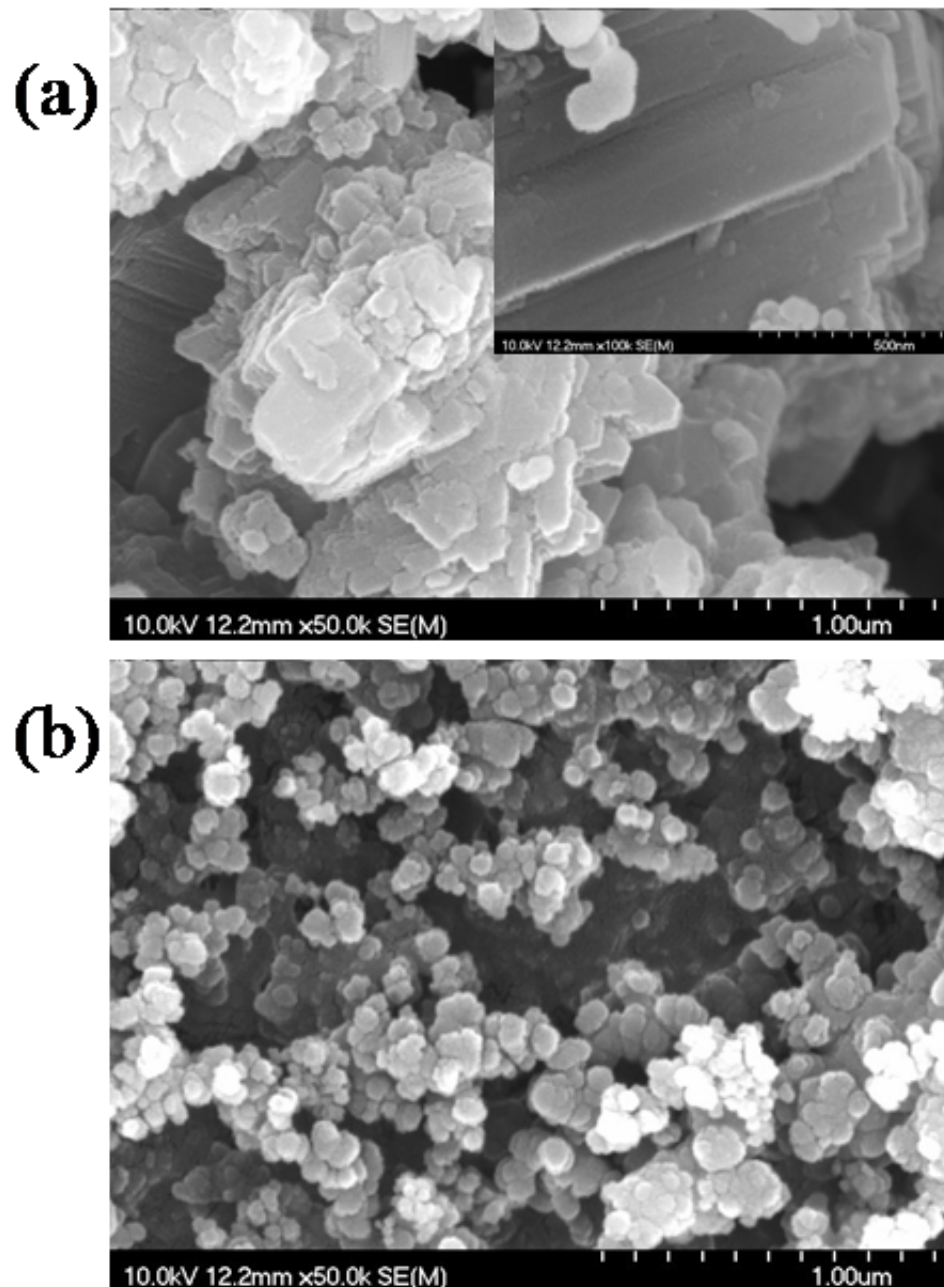


Figure 6.1 Scanning electron microscope (SEM) images of (a) 96% B and (b) 99% B. Inset shows a high magnification image of 96% B.

Figure 6.1 shows SEM images for (a) 96% B and (b) 99% B powders. From the XRD results, we checked the phases of both powders in their initial state. It was observed that the particle size of the reference 99% B is smaller than that of the 96% B (indexed by B96). In addition, it shows better homogeneity, especially in the size distribution. The inset shows a high magnification image of the 96% B. It appears to show strong crystalline phase from XRD, which is not like the amorphous 99% B. All of these characteristics can influence the phase transformation of MgB_2 during sintering.

SEM images as a function of ball milling time are shown in Figure 6.2. It was observed that the average particle size of the reference B96 was approximately 200 nm, while ball-milled B96 was in the size range of 150 nm to 170 nm. Even when the ball-milling time was significantly increased to 12 hours, the particle size did not show any significant differences in our ball-milled B96 powders. However, it seems to become more homogeneous with increasing ball-milling time.

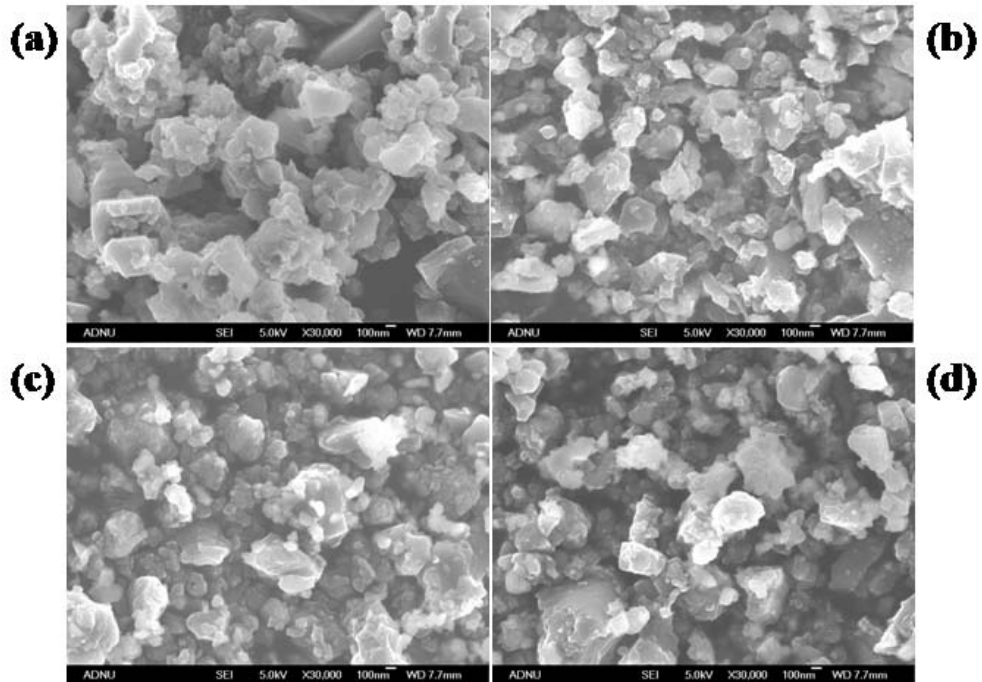


Figure 6.2 Scanning electron microscope (SEM) images for (a) B96, (b) BM4B96, (c) BM8B96, and (d) BM12B96.

6.4 Phase Transformation of MgB_2 Sample with Different Source

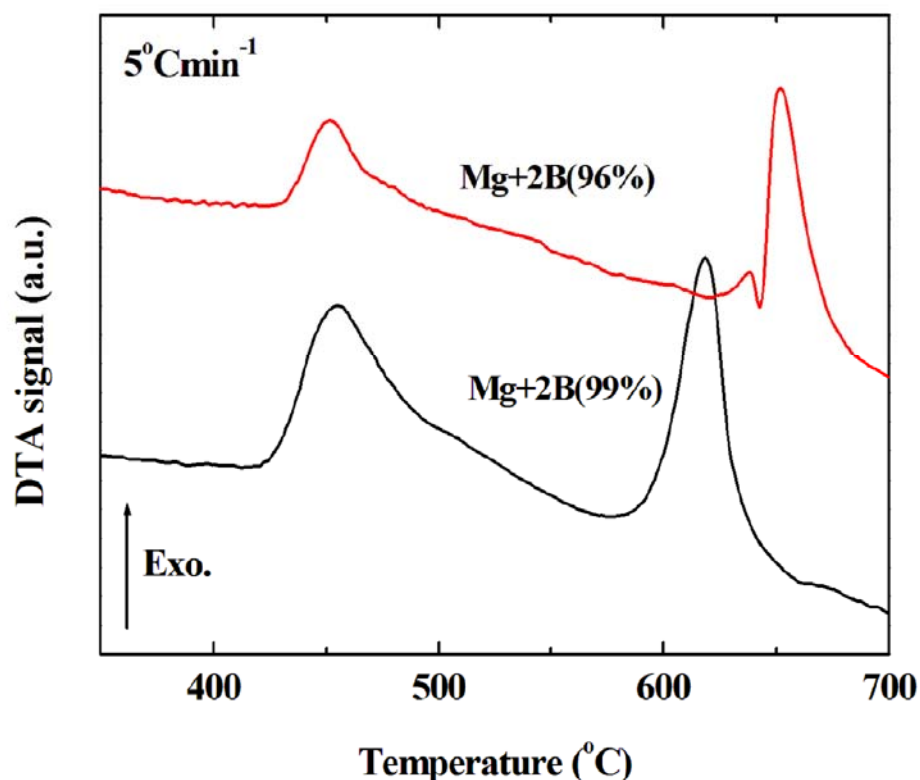


Figure 6.3 Differential thermal analysis (DTA) for MgB_2 with different B powders.

For the phase transformation of MgB_2 using 99% B and 96% B, differential thermal analysis (DTA) was performed, and the results are shown in Figure 6.3. The heating rate was 5°Cmin^{-1} under flowing Ar, as with our sintering conditions. In both samples, there were two exothermic peaks. The first exothermic peak is due to the reaction between melted B_2O_3 and Mg. The B_2O_3 has no melting point, but rather a progressive softening and melting range from 300°C to 700°C under particular conditions [5]. The crystals begin to break down at 300°C , and a series of sub-oxides are produced with partial melting until full fusion is reached at 700°C . The main reason for the presence of B_2O_3

in the B powder is because B has partially oxidized in air. As for the second exothermal peak, it can be attributed to the MgB_2 phase formation. What is interesting is that the second exothermal peaks of the two samples show different behavior. Specifically, the second exothermal peak of the sample using 96% B was slightly shifted to higher temperature, unlike sample using 99% B. In addition, there was a weak endothermal peak before the exothermal peak related to MgB_2 phase formation. This weak peak is related to the melting of Mg at around 650°C . Using 96% B with crystalline phase can introduce shifting of the second exothermal peak. We conclude that phase formation of MgB_2 using 96% B with crystalline B can occur after Mg melting. This is because using B with crystalline phase requires more energy, due to poor reactivity between Mg and B. This information was of importance in determining optimal sintering conditions for our samples. We speculate that the appropriate sintering temperature is above 650°C for MgB_2 using 96% B, and in particular, above the Mg melting point. Note that the first exothermal peak did not shift to higher temperature. If this peak is related to the solid-solid reaction of MgB_2 , this also should be shifted because of the different crystallinity. To improve the reactivity between Mg and 96% B with crystalline phase, we tried to ball mill the B powder by itself. This is because Mg handling is relatively difficult due to its easy oxidation.

6.5 Particle Size Distributions of Ball-milled 96% Boron Powder

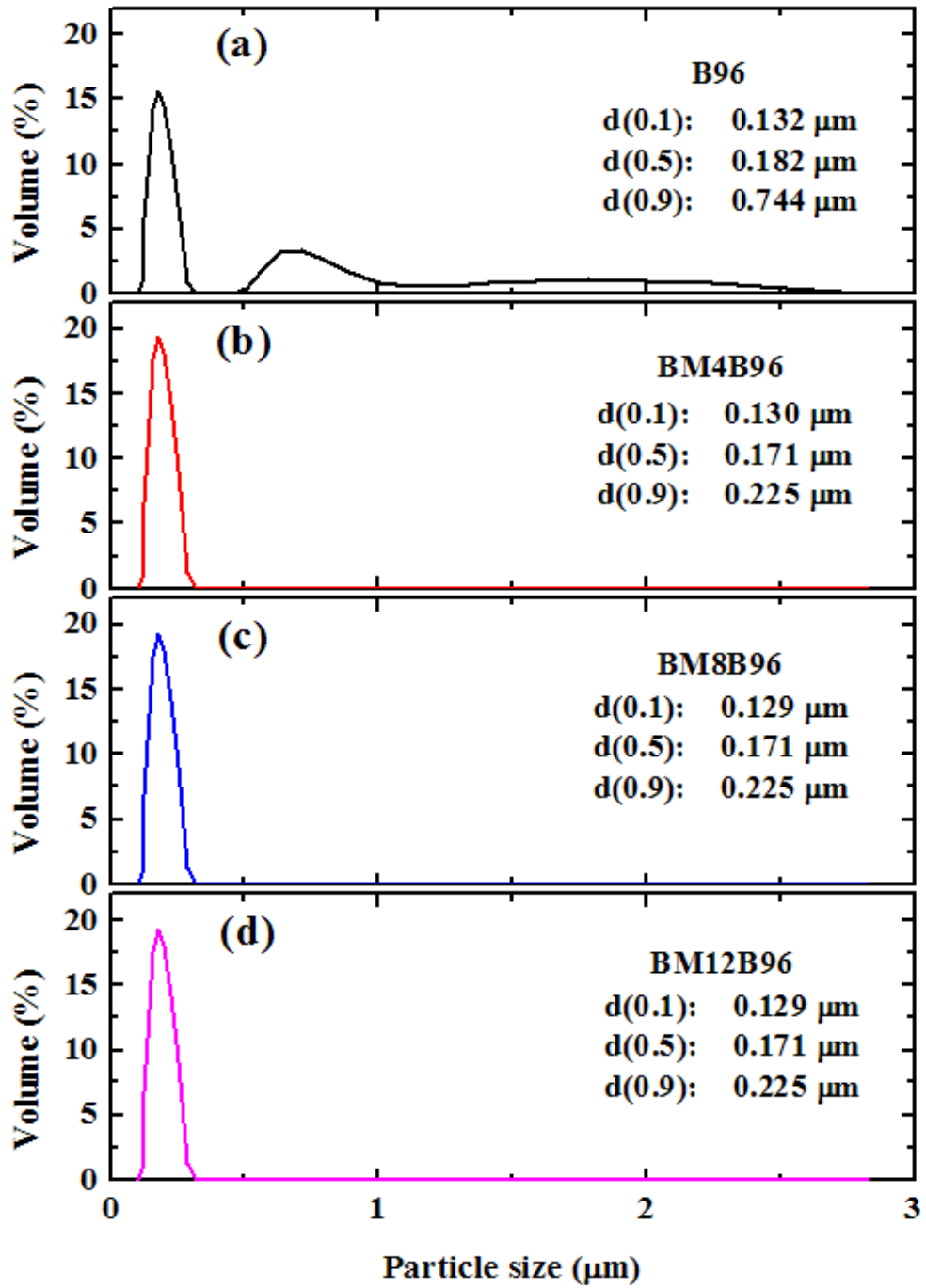


Figure 6.4 Particle size distributions for (a) B96, (b) BM4B96, (c) BM8B96, and (d) BM12B96.

Previous section results are further confirmed by the size distributions of particles in Figure 6.4. From the results, it can be seen that there was bi-modal behavior before ball-mill processing. That is to say, after ball milling, the B96 particles with sizes between 500 nm and 2500 nm disappeared. The agglomerated B powders were homogeneously dispersed. On the other hand, the results of particle size measurements show identical results for the ball milled powders. It is well known that such particle size measurements strongly depend on the agglomeration of the powder. It should be unlikely that increasing the milling time by 100% or more does not give a further reduction of particle size. As a result, the ball-milled B can improve the reactivity. The smaller particle size and greater homogeneity leads to the view that the MgB_2 particle size was determined by the size of the B powder during the sintering process, so this result must affect the superconducting properties of the samples that were formed from these B powders.

6.6 Phase Information and Lattice Parameters

Figure 6.5 shows the estimated results (from XRD) for MgB₂ superconductor made from B with different ball-milling times. We observed that lattice constants such as the *a*- and *c*-axis parameters did not change within the accuracy of error. However, the *c/a* value, which is related to structure volume, was a little decreased. This behavior can be related to the distortion of the lattice due to the storage of energy through ball milling. Even though we used a medium that contained carbon (C) in our experimental procedure, there were no apparent C substitution effects among the samples. At least, the doping level of C is almost the same within a 12 hr ball-milling time. According to Avdeev et al., results, the level of C substitution, *x* in the formula Mg(B_{1-x}C_x)₂, can be estimated as $x = 7.5 \times \Delta(c/a)$, where $\Delta(c/a)$ is the change in *c/a* compared to a pure sample. Estimated value for all samples was ~ 0.005 in the composition of Mg(B_{1-x}C_x)₂. In general, ball-milling processing leads to poorer crystallinity and connectivity of MgB₂. Finally, these can affect the full width at half maximum (FWHM) of diffractions. In our experiment, the ball milling affects the broadening of the FWHM of the characteristic MgB₂ peaks for sintered MgB₂ samples. This again indicates that crystallinity has become poorer. It is well known that the sorts of peak broadening reflected by the FWHM values can be caused by both crystalline size and lattice strain. In particular, the effects of the crystalline size of B powder can be attributed to the grain size of MgB₂. From the lattice defect point of view, again, the degradation of the crystallinity for MgB₂ originates from disordered crystal lattice that is caused by ball milling. As can be seen in Figure 6.5, the calculated FWHM values of the (110) peak were 0.309°, 0.334°, 0.374°, and 0.511°, respectively, for 0 hr, 4 hr, 8 hr, and 12 hr of

ball milling. The (100) and (002) peaks also showed the same trends. The T_c values decreased from 37.6 K to 36.4 K as the ball milling time increased to 12 hr. The behavior of T_c had an opposite trend from the FWHM.

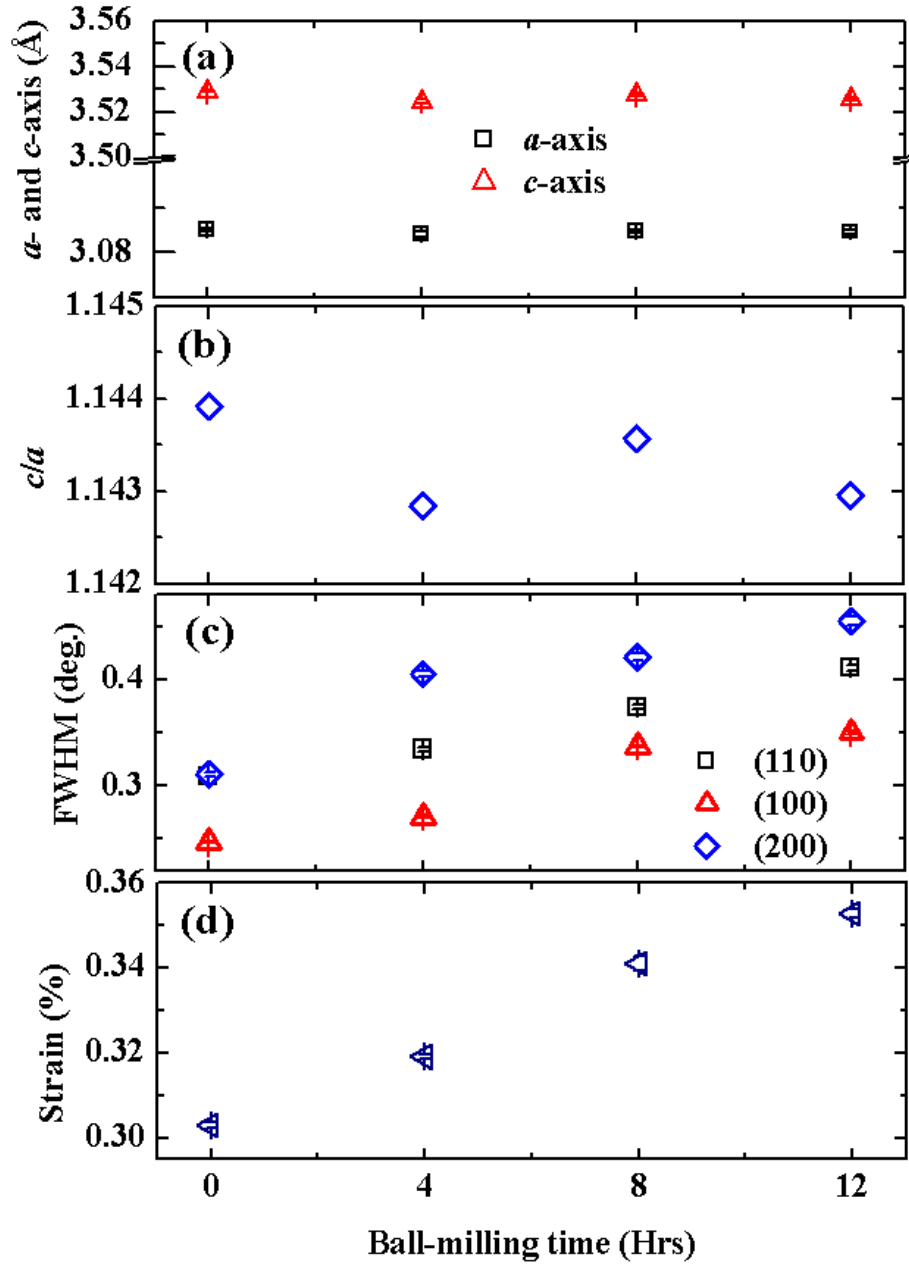


Figure 6.5 (a) a - and c -axis lattice parameters, (b) c/a , (c) full width at half maximum (FWHM) of the (110) peak, and (d) lattice strain of MgB_2 samples using different B.

6.7 MgO Effect (two knife-edges)

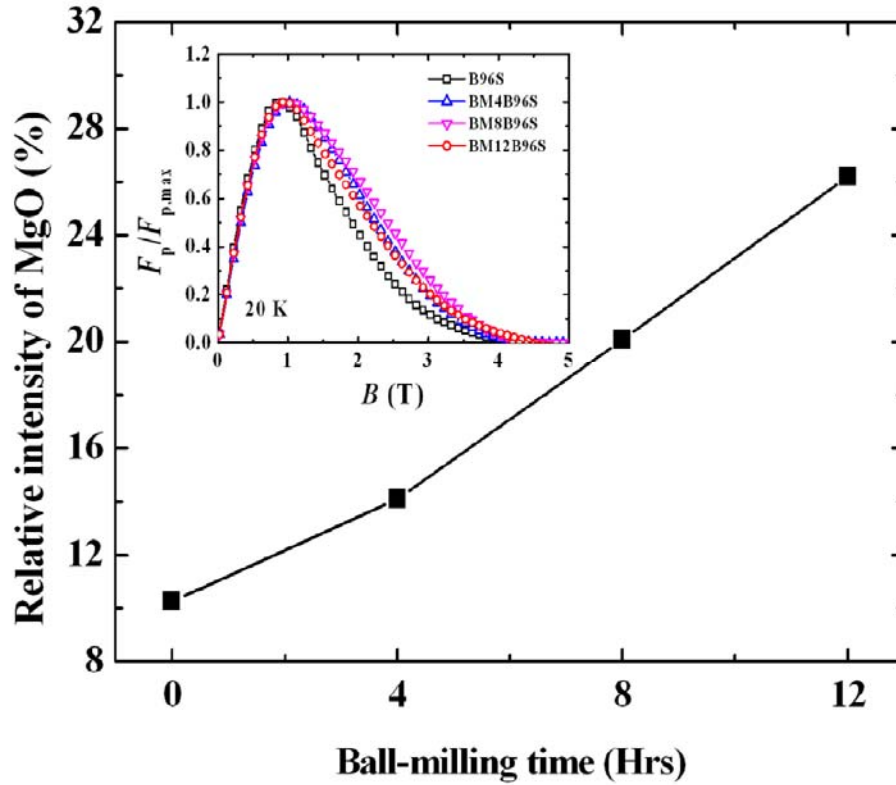


Figure 6.6 Relative intensity, $\text{MgO}(220) / \text{MgB}_2(110) + \text{MgB}_2(102)$, as a function of ball-milling time. The inset shows the relative pinning force as a function of field for the different samples.

It should be noted that the relative MgO intensity, $\text{MgO}(220) / \text{MgB}_2(110) + \text{MgB}_2(102)$ (%), increased with increasing ball-milling time, as is shown in Figure 6.6. Even though there was no oxygen (O) content in the toluene, ball milling and evaporation processing can introduce some O content, indicating the easy oxidation of B powder. Usually, B_2O_3 peaks ($2\theta \sim 14.6^\circ$ and 27.8°) appeared in the ball milled B powders. What is the key point is that the storage of energy in the B powder is increased through ball milling.

This can improve the reactivity between Mg and B, but on the other hand, this makes the reaction between B and O much easier during the mixing process.

That is to say, even though there was crystalline phase in low grade B powder, ball-mill processing can induce greater reactivity between Mg and B powders. In addition, the oxide layer on the B surfaces was probably broken during ball milling.

It is well known that an increased MgO fraction affects the degradation of superconductivity. The MgO nanoparticles could, however, enhance the flux pinning effects according to two-gap superconductivity theory. Since the coherence length $\xi^{ab}(0)$ of MgB₂ is approximately 6-7 nm, inclusion of MgO particles (~ 20 nm) within grains could result in strong flux pinning centers. However, the presence of excess oxide phases or large-sized particles (> 50 nm) at the grain boundaries could result in degradation of grain connectivity. For superconductivity, therefore, MgO as the main secondary phase will be of great importance and yield a positive or negative effect for the J_c at the same time. If oxidation results in the presence of MgO, it also causes Mg deficiency. The presence of Mg vacancies in the MgB₂ structure could be responsible for the change in the structural volume of our ball-milled samples and cause the significant degradation of T_c . Even though ball-mill processing still has a lot of disadvantages for MgB₂, this can also introduce small grain size after sintering, resulting in strong flux pinning centers, as can be seen in the inset of Figure 6.6. As a result, we need to study the correlation between MgO formation and flux pinning.

6.8 Resistivity and Connectivity Effect

To further understand the positive or negative effects of MgO particles in our samples, the dependence of the resistivity (ρ) of MgB₂ on the use of different ball-milled B powders, can be seen in Table 6.1, where resistivity values at 40 K and 300 K increased as the B ball-milling time increased. Specifically, a lower value of ρ at 300 K indicates good grain connectivity. This can be further supported by the RRR ($\rho_{300\text{ K}} / \rho_{40\text{ K}}$) values. The RRR values decreased from 2.65 to 1.86, as the ball-milling time increased. Rowell [6] also reported that $\Delta\rho$ ($\rho_{300\text{ K}} - \rho_{40\text{ K}}$) is of great importance for estimating the grain connectivity. According to the Rowell connectivity analysis, the active cross sectional area fraction (A_F) represents the connectivity, which is estimated by comparing the measured value with that of a single crystal. Although $\Delta\rho$ of Rowell and Jiang et al. [7] assumed 4.3 $\mu\Omega\cdot\text{cm}$ and 7.3 $\mu\Omega\cdot\text{cm}$, respectively, with different reference values, we can show that the behavior varies with different ball-milling times. The data can explain the connectivity effects on ball-milled samples, that when the ball-milling time is increasing, the grain connectivity becomes worse, leading to no obvious differences in J_c in low field at 20 K, but large improvements for the ball-milled samples in high field at 5 K.

Samples	$\rho_{40\text{K}}$ ($\mu\Omega\cdot\text{cm}$)	$\rho_{300\text{K}}$ ($\mu\Omega\cdot\text{cm}$)	$\Delta\rho$ ($\rho_{300\text{K}} - \rho_{40\text{K}}$) ($\mu\Omega\cdot\text{cm}$)	RRR	A_F	T_c (K)
B96S	13.4	35.7	22.3	2.66	0.33	37.6
BM4B96S	19.6	42.6	23.0	2.18	0.32	37.0
BM8B96S	29.8	54.5	24.7	1.83	0.29	36.3
BM12B96S	66.8	124.3	57.5	1.86	0.13	36.4

Table 6.1 The measured resistivity values, residual resistivity ratios (RRR), and active cross-sectional area fraction (A_F) for MgB₂ with different ball-milling times.

Currently in the literature, Matsumoto has reported that ball milling Mg alone enhanced the J_c . However, ball milled MgH_2 as a precursor did not result in increased J_c value. The presence of light MgO particles due to ball milling may be effective for high J_c . On the other hand, MgO acts as a current barrier in MgB_2 [7], causing decreased active area fraction and increased resistivity, while having effects on the grain connectivity, so as to reduce the J_c in low field. Clearly, the formation possibilities for MgO within MgB_2 exist because Mg can act as a potential O getter in air or because of oxidation during sintering due to gaseous O.

6.9 Comparison of T_c , J_c , and Pinning Force Strength

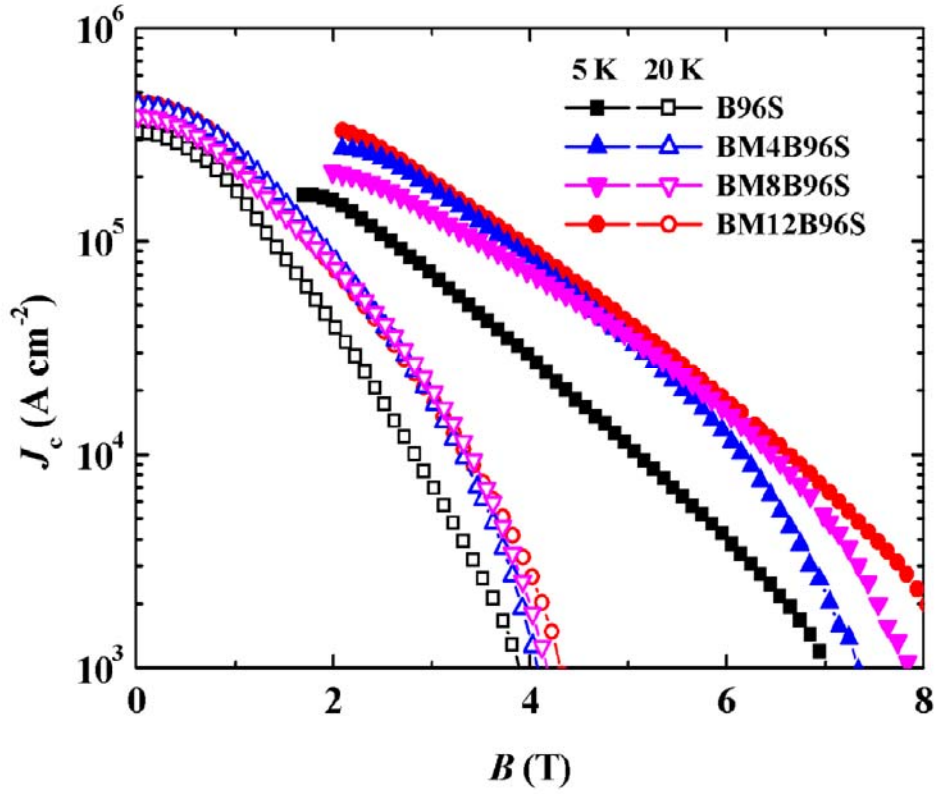


Figure 6.7 The magnetic critical current density (J_c) for all MgB_2 samples as a function of external magnetic field at 5 and 20 K.

Figure 6.7 shows the magnetic $J_c(B)$ behavior at 5 K and 20 K. At 5 K, J_c for the sample with 12 hr ball milled B was estimated to be 2000 Acm^{-2} at 8 T. This J_c value is much higher than for the sample without any ball-milling process. This is due to the small grain size, which is effective for enhancing flux pinning. However, the difference in the J_c became smaller under low field, $< 2 \text{ T}$. On the other hand, $J_c(B)$ behavior at 20 K did not exhibit much difference. This is because the T_c of the samples affected $J_c(B)$. In addition, grain boundary effects were negligible. For example, even though the samples using ball-milled B had good $J_c(B)$ performance at 4.2 K and 4 T, $J_c(B)$ for all samples

showed little difference at 20 K and 4 T. That is, grain connectivity or high T_c of samples is of great importance at 20 K. What is interesting is that self field J_c remained unchanged after ball milling. Further work is needed to clarify this issue.

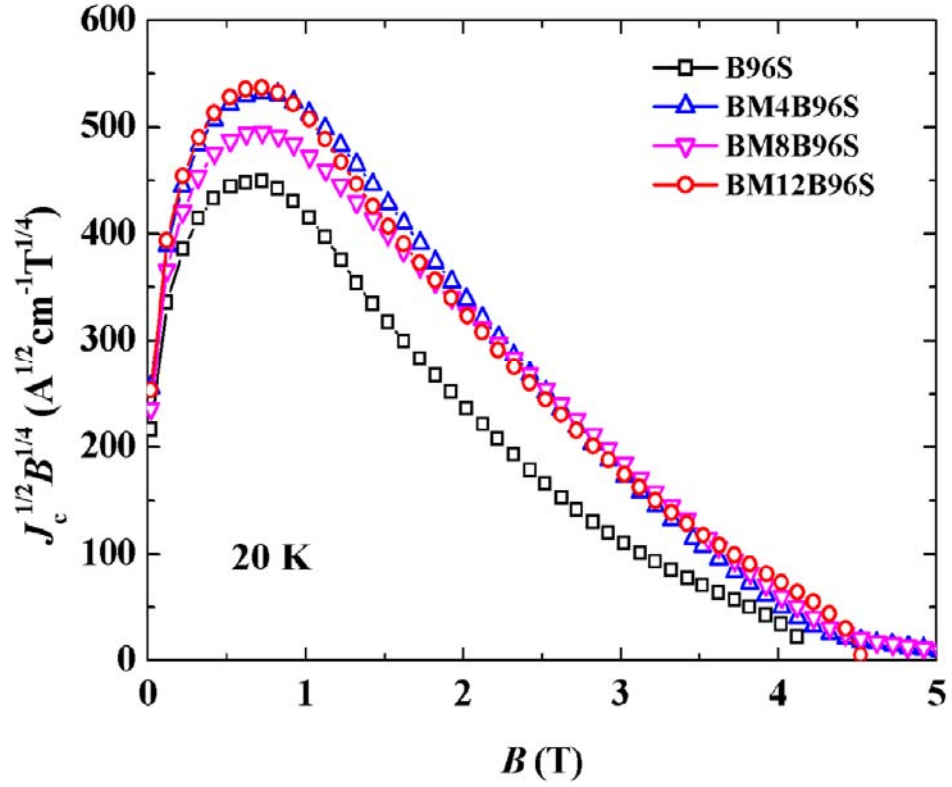


Figure 6.8 Kramer plot (F_k) of the pinning force, $J_c^{1/2} \times B^{1/4}$, for all samples at 20 K.

These phenomena can further be supported by the Kramer plot (F_k) [8] at 20K, as can be seen in Figure 6.8. Pinning force strength, $J_c^{1/2} \times B^{1/4}$, it was observed that the pinning force of all the ball-milled samples is larger than that of the reference sample. The improved pinning in field seems to be caused by the enhanced grain boundary pinning provided by the larger number of grain boundaries. Although F_k is not really linear at low field, if we extrapolate F_k to zero, we can deduce the characteristic H_{irr} values. The main reason for the curvature at lower J_c might be due to percolative paths, which in fact give a transport J_c that is always higher than the value extracted from magnetic loop [9].

6.10 Upper Critical Field and Irreversibility Field from Transport Measurement

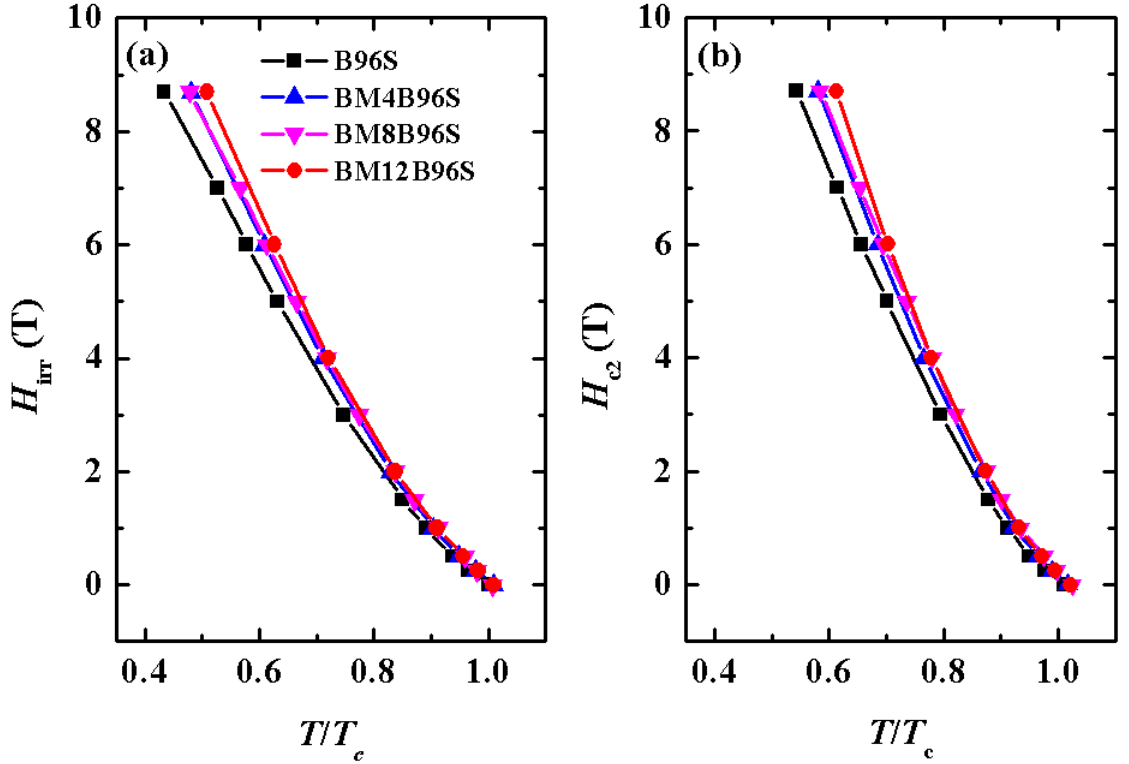


Figure 6.9 Temperature dependence of irreversibility field (H_{irr}) and upper critical field (H_{c2}) for all samples with different ball-milling times.

From R-T curve, the temperature dependence of H_{irr} and H_{c2} for all the samples is shown in Figure 6.9. As can be seen in the Figure, the values of H_{c2} and H_{irr} were enhanced systematically as the ball-milling time increased to 12 hr. These properties showed the same trends as $J_c(B)$ at 4.2 K. This indicates that degradation of crystallinity is the guiding principle for high H_{irr} and H_{c2} . In addition, the $H_{c2}-T$ curves of all samples show similar behavior to those of $H_{irr}-T$. For example, the curves showed a positive curvature very near T_c , while the curve was linear except for this region. The positive

curvature of H_{c2} at $T \approx T_c$ indicates that the diffusivity in the σ bands is suppressed compared to that in the π bands [10].

6.11 Conclusion

In conclusion, we have shown that the starting B powder is important in determining the $J_c(B)$ performance of MgB_2 samples. The reactivity of 96% B powder can be improved by using ball-mill processing, leading to enhanced magnetic critical current density, J_c , compared to the original 96% B powder. The A_F values can explain the connectivity effects on ball-milled samples; when the ball-milling time is increased, the grain connectivity becomes worse, leading to little change in J_c in low field at 20K, but strong effects on the high field J_c at 5 K.

This could be related to the small grain size and poor crystallinity. Specifically, the MgO fraction was increased within the matrix through ball milling, which influences properties such as flux pinning. Further study of the ball-milling process thus promises to allow adjustment of the desired phase form, which should be optimized along with the sintering conditions, so as to create a balance between the inter-grain connectivity and the pinning centers. We should also rethink the possibilities of metal oxide dopants in MgB_2 to obtain possible enhancements to the superconductivity. The MgB_2 made using low grade 96% B powder could be particularly useful for industrial applications because of its low material cost.

6.12 References

1. L. D. Cooley, A. K. Ghosh, and R. M. Scanlan, *Supercond. Sci. Technol.* **18** R51, (2005).
2. W. Haessler, B. Birajdar, W. Gruner, M. Herrmann, O. Perner, C. Rodig, M. Schubert, B. Holzapfel, O. Eible, and L. Schultz, *Supercond.Sci.Technol.* **19** 512, (2006).
3. M. Herrmann, W. Haessler, C. Mickel, W. Gruner, B. Holzapfel, and L. Schultz, *Supercond.Sci.Technol.* **20** 1108, (2006).
4. M. Herrmann, W. Haessler, C. Rodig, W. Gruner, B. Holzapfel, and L. Schultz, *Appl. Phys. Lett.* **91** 082507, (2007).
5. J. H. Kim, S. X. Dou, D. Q. Shi, M. Rindfleisch, and M. Tomsic, *Supercond.Sci.Technol.* **20** 1026, (2007).
6. J.M. Rowell, *Supercond. Sci.Technol.* **16** R17, (2003).
7. J. Jiang, B. J. Senkowicz, D. C. Larbalestier, and E. E. Hellstrom, *Supercond.Sci. Technol.* **19** L33, (2006).
8. E.J. Kramer, *J. Appl. Phys.* **44** 1360, (1973).
9. V. Braccini, L.D.Cooley, S. Patnaik, D.C. Labalestier, P. Manfrenetti, A. Palenzona, A.S. Siri, *Appl.Phys.Lett.* **81** 4677, (2002).
10. A. Gurevich , *Phys.Rev.B* **67** 184515, (2003).

Chapter 7: Further Study of Transport Current Density and Grain Connectivity in MgB₂/Fe Wire Made from Ball-milled Low Purity Boron

7.1 Why Need Wire Result for Comparison

It is well known that the critical current density (J_c) of pure MgB₂ is drastically decreased with an increasing external magnetic field because of its poor flux pinning properties, when compared to high temperature superconductors (HTS). Quite interestingly, however, unique features of the superconductivity observed in the MgB₂ are related to its two-band nature and the lack of weak-links at the grain boundaries [1]. In addition, the advantages of the simple binary composition, the transition temperature of 39 K, and the low cost of the starting materials have been sufficient to put it on the road to real applications.

So far, it has been achieved improvements in the critical current density (J_c) and upper critical field (B_{c2}) through ball-milling processing. As the first step, the effects of ball milling pure boron (B) powder (99%, amorphous) using different media, such as acetone, ethanol, and toluene, were studied. Using toluene led to enhancements in the magnetic critical current density (J_{cm}) in high field. For the second step, The samples were prepared from low grade boron (96%) with semi-crystalline phase via ball-milling in toluene as well. The results of this have demonstrated the possibility and cost effectiveness of fabricating high performance samples using low grade boron [2]. All

previous reports in the literature have been directed towards finding effective means of reducing the strong field dependence under high field. However, the low field performance might be further improved to attain a particular level, for example, $> 10^6$ Acm⁻². In particular, the initial Mg and B powders that we previously studied in pellet form are loosely connected before the reaction. After heat-treatment, even if reacted MgB₂ is expected to be more consolidated, it is likely to have some porosity, depending on the packing conditions in *in situ* processing. Therefore, it would be hard to estimate the connectivity factor from those pellet samples. What is important is that the results on our bulk samples still gave us the possibility that low grade 96% B powder can be adopted for industrial applications.

For conductors, the powder-in-tube (PIT) method is very common, in which a metallic sheath is packed with powders and then is drawn. The MgB₂ fabricated by the PIT method is polycrystalline with some orientation along the rolling direction, and it is well known that there are no weak-link effects at the grain boundaries. Thus, grain boundaries could act as the dominant pinning centres. In the wire conductor, the relative amount of porosity is decreased due to mechanical deformation, which results in improved core densification, unlike what is seen in pellet samples. As a result, we speculate that the wire processing further promoted the grain connectivity due to the high pressure applied to the sample and, thus, resulted in the different performances of conductors and pellets. Therefore, we need to evaluate the correlation between the transport current density and the grain connectivity in wire conductor. In addition, there are some more detailed reasons for this study. The transport critical current density (J_{ct}) is the real useful J_c that flows through the whole of the sample, while the magnetic critical current density (J_{cm}) overestimates the real J_c at low fields and underestimates it at high fields [3]. This difference between J_{cm} and J_{ct} in MgB₂ is related to the

microstructure of the superconducting MgB_2 core. There are superconducting screening currents flowing on different length-scales due to sample porosity and agglomeration of superconducting crystals [4]. Some simulations show that major defects in the superconducting core will have an affect on the transport current [5].

In the present work, therefore, studies of the transport critical current density (J_{ct}) and grain connectivity of the MgB_2/Fe wires fabricated from ball-milled boron have been conducted in detail, and strong correlations have been found. We evaluated the superconducting properties of MgB_2/Fe made from low-grade 96% commercial boron powder with a strong crystalline phase. The particle size of the boron, the transport critical current density (J_{ct}), the critical temperature (T_c), the residual resistivity ratio (RRR), the upper critical field (B_{c2}), the irreversibility field (B_{irr}), and the microstructures of MgB_2 made from ball-milled boron are presented in comparison with reference samples made at different sintering temperatures.

7.2 Sample Preparations

MgB₂/Fe monofilament wires were prepared by an *in situ* reaction process and the powder-in-tube method. Boron powder (Tangshan WeiHao, China) with strong semi-crystalline phase and 96% purity was processed by ball milling, with toluene as the ball-milling medium. The ball-milling process was carried out for 12 hrs at a rotation speed of 160 rpm. The powder to ball ratio was 1: 16 in a planetary ball-mill with an agate jar and balls 5 mm and 10 mm in size. The powders were then dried in a vacuum oven to evaporate the toluene. For our experiments, two kinds of boron powder were prepared, with and without ball milling: these are denoted by BP96 and P96, respectively. Here, the ball-milled boron is denoted by the initial B.

Magnesium (99%, 325 mesh), and the different boron powders with the nominal atomic ratio of Mg : B = 1 : 2 were mixed through grinding and were put into Fe tubes with a length of 140 mm, an outer diameter (O.D) of 10 mm, and an inner diameter (I.D) of 8 mm. The packing process was carried out in air. Both ends of the tubes were sealed with aluminum pieces, and then the tubes were drawn to a wire with a diameter of 1.4 mm. Short wire samples (4 cm each) were sealed with Zr foil, then sintered with a heating rate of 5 °C min⁻¹ in flowing high purity Ar to 650-800 °C and held at the final temperature for 30 minutes, followed by a furnace cooling to room temperature. The volume fraction of the superconducting core in the final wire was approximately 48%.

The boron powder particle size and distribution were determined by a JL-1166 Laser Particle Sizer (Chengdu, China) from Tangshan WeiHao. The phase and crystal structure of all the samples were investigated by X-ray diffraction (XRD). The crystal structure was refined with the aid of the program Jade (ver. 5.0). The grain morphology and the microstructure of the MgB₂ were studied by scanning electron microscopy

(SEM). The transport current (I_c) at 4.2 K was measured by the standard dc four-probe resistive method with a criterion of $1 \mu\text{Vcm}^{-1}$ in magnetic fields up to 12 T. T_c was determined using the standard ac four-probe method. In addition, $B_{c2}(T)$ and $B_{irr}(T)$ were defined as the fields where the temperature dependent resistance at constant magnetic field $R(B_{c2}, T) = 0.9R_{ns}$ and $R(B_{irr}, T) = 0.1R_{ns}$, respectively, with R_{ns} being the normal state resistance near 40 K.

7.3 Particle Size Distributions

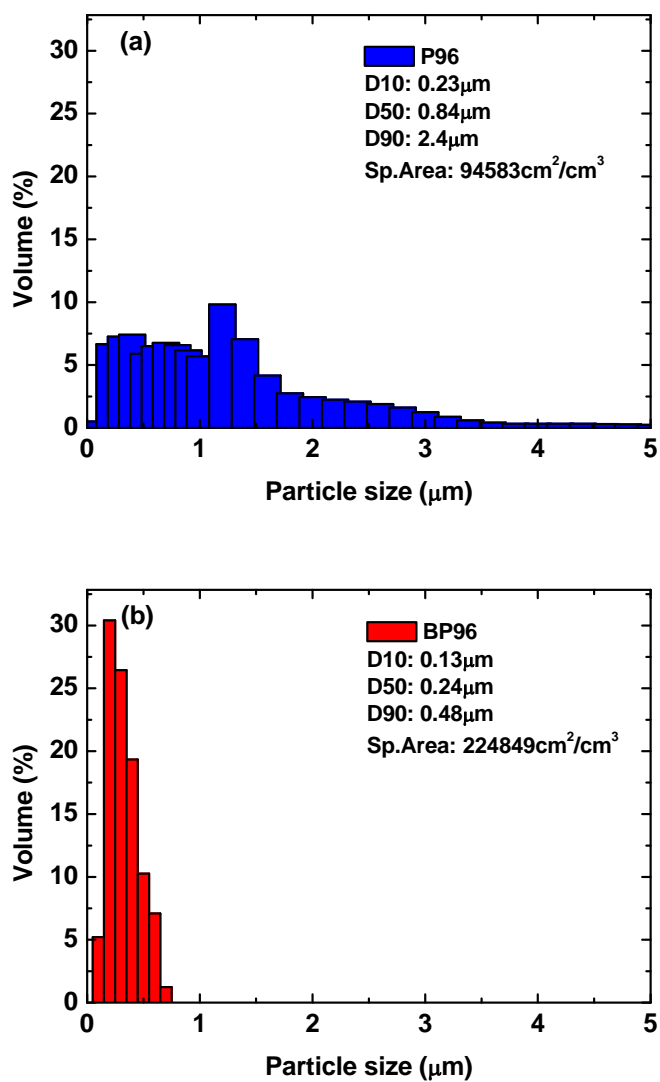


Figure 7.1 Particle size distributions for (a) as-supplied and (b) ball-milled boron powders.

Figure 7.1 shows the particle size distributions of (a) the as-supplied boron, P96, and (b) the ball-milled boron powder, BP96. It can be clearly seen that the average particle size of the original boron powder, P96, became smaller after ball-milling. For example, the median value (D50) decreased from 0.84 μm to 0.24 μm. The size distribution of the

BP96 also became narrow. If we neglect the effect of the powder shape, the small particle size led to a more than two-fold increase in the specific surface area, which may tend to improve the reactivity between the powders, even under the same solid reaction conditions. It is well known that the grain size of the MgB_2 as it is formed depends on the particle size of the boron powder. The small grains could act as strong flux pinning centres for MgB_2 . Therefore, it is not surprising that the MgB_2 prepared from the ball-milled boron powder (BP96) had small grain size and showed improved superconducting properties.

7.4 SEM Studies

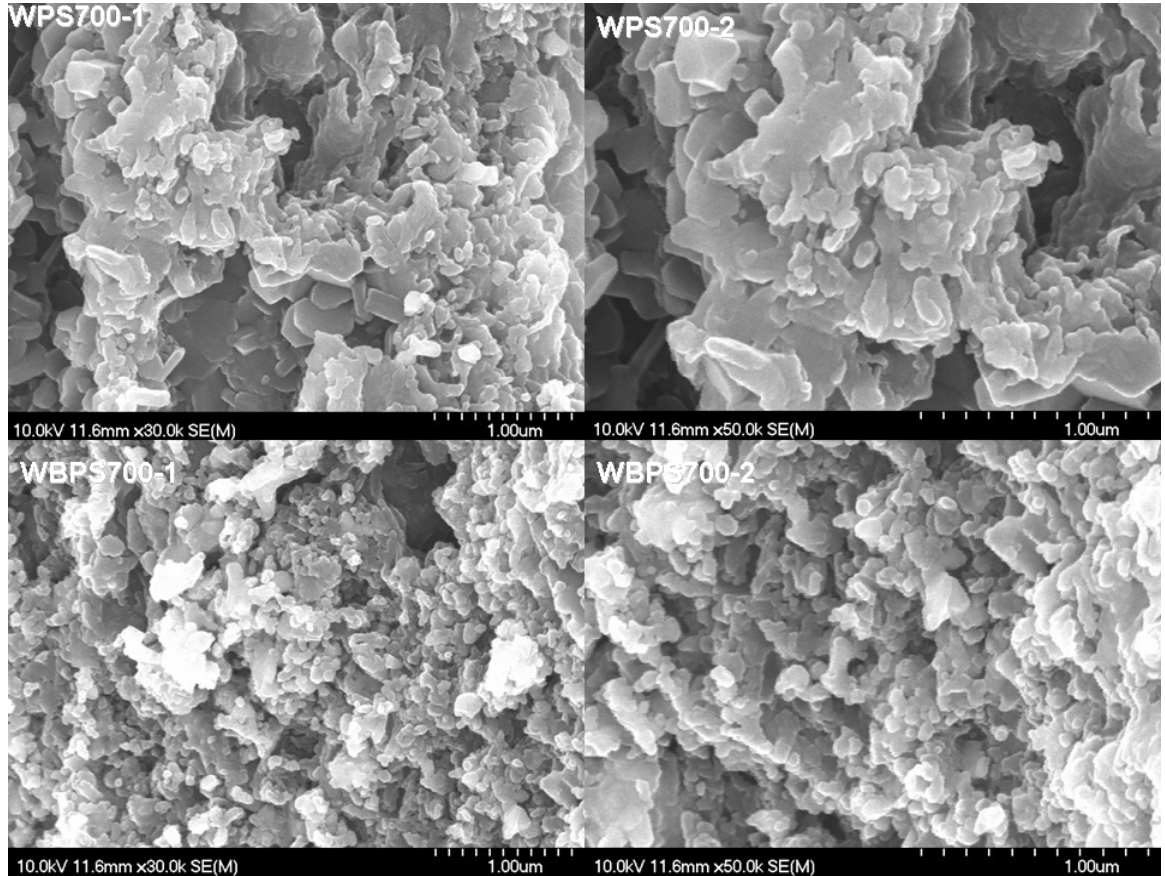


Figure 7.2 Scanning electron microscope (SEM) images at two magnifications for (top) wire sample prepared from as-supplied boron, and (bottom) wire sample prepared from ball-milled boron. All samples were sintered at 700°C for 30 minutes.

SEM images of MgB_2 wires made from (a) as-supplied boron (P96) and (b) ball-milled boron powders (BP96), denoted as WPS700, and WBPS700, respectively, are shown in Figure 7.2, with all samples sintered at 700 °C for 30 minutes. Here, the wire samples are identified by the initial W, and the sintering temperature is denoted by the numerals. It is clearly observed that the average grain size of the sample prepared from the ball-milled boron is much smaller than in the sample made from the as-supplied boron. It also seems to be more consolidated. From the crystallinity point of view, on the other

hand, the sample prepared from the ball-milled boron showed poor crystallinity, as evidenced by the degradation of the transition temperature, to be discussed below. The crystallinity effect has already been reported in our previous work [2]. In general, the crystallinity, as reflected by the lattice parameters, secondary phases, and micro-strain, is an important factor determining the T_c . We also observed that the MgO fraction increased over the entire MgB₂ volume after ball-milling, as evidenced by XRD measurements. The increased MgO may have caused loss of the initial stoichiometry, which affects the level of induced strain due to Mg deficiency. As the main secondary phase, we can not neglect MgO in the matrix, although the MgO particles can not be directly distinguished from the SEM images. Among our samples, the ball-milled samples (WBPS700) had a higher MgO intensity increase, approximately 9%, compare to samples (WPS700) prepared from as-supplied boron. Due to the large fraction of MgO, therefore, they showed increased $\Delta\rho$ ($\rho_{300\text{ K}} - \rho_{40\text{ K}}$) and decreased RRR ($\rho_{300\text{ K}} / \rho_{40\text{ K}}$) values (as shown in Table 7.1), a degraded grain connectivity factor (A_F), and reduced J_{ct} , which offset the strong pinning properties due to the effect of small grain size.

Samples ID	ρ_{40K} ($\mu\Omega\cdot\text{cm}$)	ρ_{300K} ($\mu\Omega\cdot\text{cm}$)	$\Delta\rho$ ($\rho_{300K}-\rho_{40K}$) ($\mu\Omega\cdot\text{cm}$)	RRR	A_F	T_c (K)	lattice strain (%)
WPS650	34.8	78.7	43.9	2.26	0.166	37.9	0.273(1)
WPS800	20.3	49.4	29.1	2.43	0.250	38.1	0.284(1)
WBPS650	84.5	151.1	66.6	1.78	0.109	37.4	0.338(1)
WBPS800	64.3	125.2	60.9	1.94	0.119	37.4	0.315(1)

Table 7.1 The measured resistivity values, residual resistivity ratios (RRR), active cross-sectional area fractions (A_F), critical temperatures (T_c), and lattice strain for MgB₂ wire made from ball-milled boron and from as-supplied boron under comparable sintering conditions.

7.5 Transport Critical Current (J_{ct})

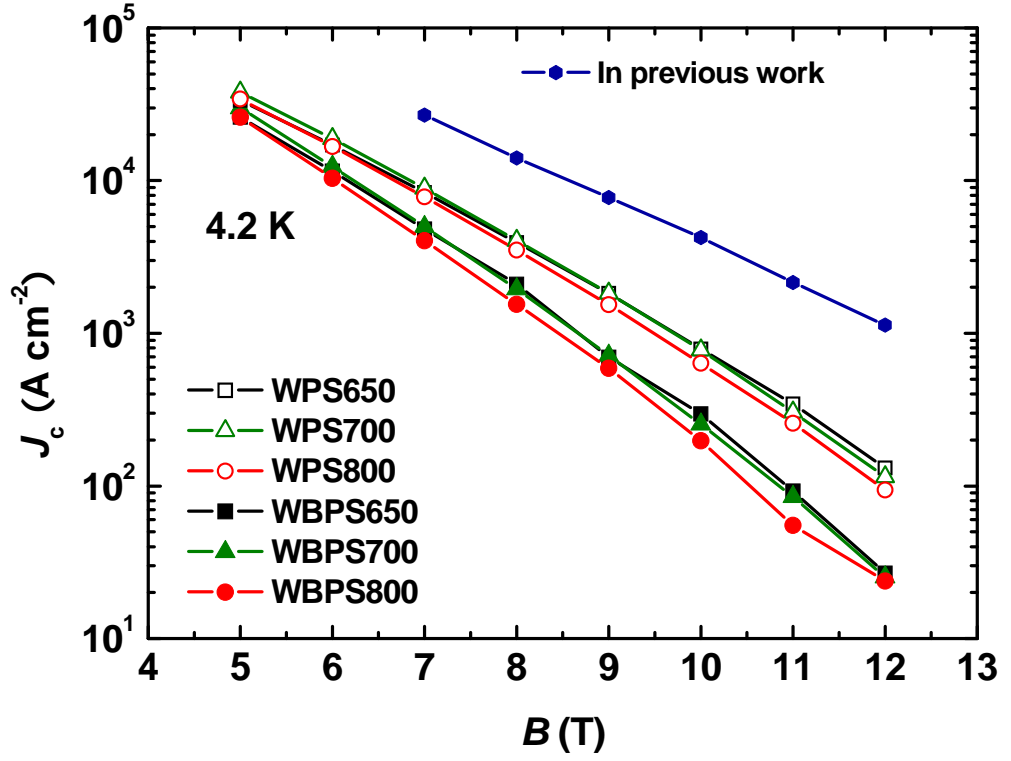


Figure 7.3 Transport critical current density (J_{ct}) for all MgB_2 wires as a function of external magnetic field at 4.2 K.

A comprehensive study comparing the positive “*small grain size*” and negative “*weak connectivity*” effects on the J_{ct} was conducted. The J_{ct} - B performance of the two kinds of the samples sintered at temperatures from 650 °C to 800 °C, denoted by WPS650, WPS700, WPS800, WBPS650, WBPS700, and WBPS800, respectively, is shown in Figure 7.3. MgB_2 sample was using 99% B for comparison from Ref.9.

It can be clearly seen that J_{ct} of samples prepared from the ball-milled boron showed better performance in the field range of 5 to 12 T. This indicates that ball milling causes

reduction of the MgB_2 grain size, which could act as a source of strong pinning centers due to the increased number of grain boundaries, as mentioned above.

However it was concluded that the ball-milling could not help to improve the J_{ct} at magnetic fields below 5 T. Compared to the magnetic J_{cm} under magnetic fields of 5 to 8 T, the transport J_{ct} increment is lower, because the transport current capacity is the real useful J_c that flows through the whole of the sample. That is to say, the difference between J_{cm} and J_{ct} in MgB_2 may be related to features of the microstructure of the superconducting MgB_2 core, such as porosity, agglomeration of superconducting crystals, and fraction of MgO as the main secondary phase. These could have negative effects on the J_{ct} , by acting as obstacles to current flow. Quite interestingly, the effects of these obstacles do not appear in magnetic loop measurements. That is why the magnetic J_{cm} does not represent the real J_c of MgB_2 wires [4].

7.6 Relation between the Transition Temperature and Resistivity

According to the Rowell connectivity analysis, the calculated active cross-sectional area fraction (A_F) represents the connectivity factor between adjacent grains. From Table 7.1, the A_F for all samples increased as the sintering temperature increased. This indicates that additional grain growth occurs due to high temperature sintering. The larger grains are also accompanied by improved density and grain connectivity. Thus the A_F increases. This can be further supported by the RRR ($\rho_{300\text{ K}} / \rho_{40\text{ K}}$) values. The RRR values for all samples were decreased through low temperature sintering, as well as by ball-milling. A large RRR is an important determinant of a high quality sample. In particular, an increased $\rho_{40\text{ K}}$ value is due to increased impurity scattering in the lattice. That is to say, it causes an increase in the lattice strain, resulting in degradation of the transition temperature.

If disorder is an important factor affecting the transition temperature of MgB_2 samples, there should be a relation between the resistivity and the transition temperature. In a previous review, the Testardi correlation, an empirical relation between the RRR and the transition temperature, was discussed in connection with Nb-Ge film [7]. As shown in Figure 7.4(a), we found that the critical temperature shows a dependence on the RRR, which can be expressed by a simple linear function. A more interesting correlation is suggested in a recent review of Eisterer between the transition temperature and the normalized resistivity [8], the ratio of the residual resistivity to the difference in resistivity between 300 and 40 K, $\rho_{\text{norm}} = \rho_{40\text{ K}} / \Delta \rho$, where $\Delta \rho = \rho_{300\text{ K}} - \rho_{40\text{ K}}$. Various reported data were compared, and it was argued that the transition temperature can be described by a simple linear relation, $T_c = (39.43 - 2.515 \rho_{\text{norm}})$ K. We found that our

data are also compatible with a similar linear relation: $T_c = (39.36 - 1.67 \rho_{\text{norm}})$ K, as shown in Figure 7.4(b). Thus, degradation of the transition temperature is strong evidence of poor crystallinity and connectivity.

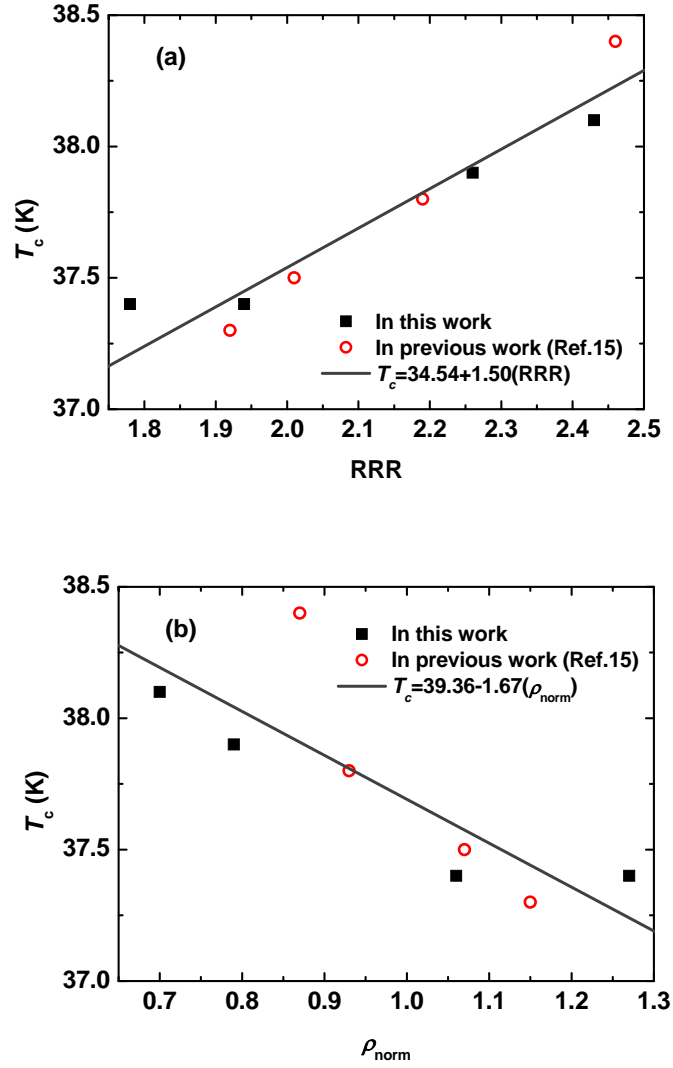


Figure 7.4 The correlations between (a) the transition temperature (T_c) and the residual resistivity ratio (RRR), and (b) the critical temperature (T_c) and the normalized resistivity (ρ_{norm}).

7.7 Upper Critical Field and Irreversibility Field from Transport Measurement

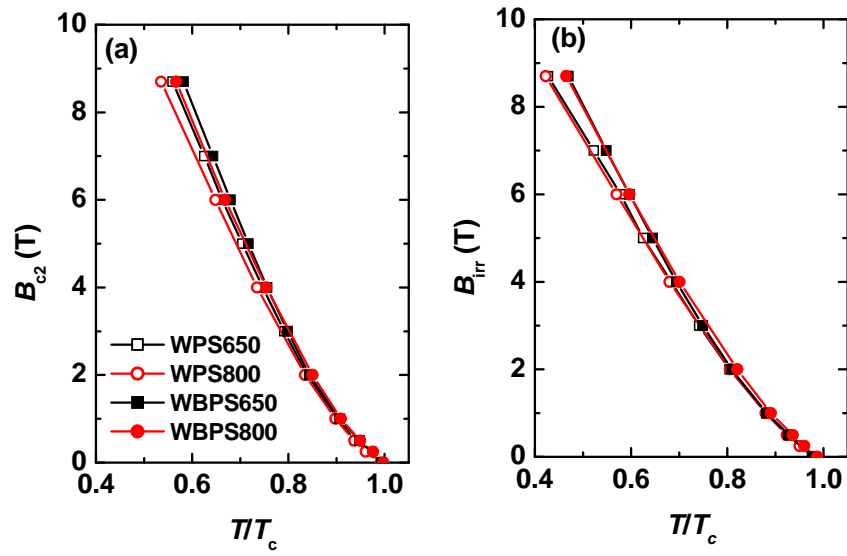


Figure 7.5 Temperature dependence of (a) the upper critical field (B_{c2}) and (b) the irreversibility field (B_{irr}) for MgB_2 wires as a function of sintering temperature.

From the resistance (R)-temperature (T) curves, the temperature dependence of B_{c2} and B_{irr} for all the samples is shown in Figure 7.5. As can be seen in the Figure, the values of B_{c2} and B_{irr} were enhanced via ball milling as well as by low temperature sintering. The B_{irr} showed the same trends as $J_{ct}(B)$ at 4.2 K, that is, a significant increase in the upper critical field, B_{c2} , is the main cause of the enhancement of the critical current density, J_c , in the high field region. Also, the $B_{c2}-T$ curves of the samples show that a

low sintering temperature is better than a high one, which indicates that more defects or poor crystallinity within grains induces lattice strain, decreases T_c , and increases B_{c2} .

7.8 Conclusion

In conclusion, a comprehensive study of ball-milling effects on the transport critical current density (J_{ct}) and grain connectivity factor (A_F) of MgB_2/Fe wires has been conducted. We observed that lattice disorder increased due to the ball milling. It caused both a slight reduction in the transition temperature and degradation of connectivity. The reduction in the transition temperature can change the upper critical field, so that the upper critical field is mostly affected by the lattice disorder. A significant increase in the upper critical field is the main cause for the enhancement of the critical current in the high field region. On the other hand, high temperature sintering in all types of samples can improve J_{ct} in the low field region because it leads to good grain connectivity.

7.9 References

1. D. C. Larbalestier, M. O. Rikel, L. D. Cooley, A. A. Polyanskii, J. Y. Jiang, S. Patnaik, X. Y. Cai, D. M. Feldmann, A. Gurevich, A. A. Squitieri, M. T. Naus, C. B. Eom, E. E. Hellstrom, R. J. Cava, K. A. Regan, N. Rogado, M. A. Hayward, T. He, J. S. Slusky, P. Khalifah, K. Inumaru, and M. Haas, *Nature* **410** 186, (2001).
2. X. Xu, J. H. Kim, M. S. A. Hossain, J. S. Park, Y. Zhao, S. X. Dou, W. K. Yeoh, M. Rindfleisch, and M. Tomsic, *J. Appl. Phys.* **103** 023912, (2008).
3. J. Horvat, W. K. Yeoh, J. H. Kim and S. X. Dou, *Supercond. Sci. Technol.* **21** 065003, (2008).
4. J. Horvat, S. Soltanian, X. L. Wang, and S. X. Dou, *Appl. Phys. Lett.* **84** 3109, (2004).
5. E. Bartolome, F. Gömory X. Granados, T. Puig, and X. Obradors, *Supercond. Sci. Technol.* **18** 388, (2005).
6. L. R. Testardi, R. L. Meek, J. M. Poate, W. A. Royer, A. R. Storm, and J. H. Wernick, *Phys. Rev. B* **11** 4304, (1975).
7. M. Eisterer, *Supercond. Sci. Technol.* **20** R47, (2007).
8. J. H. Kim, S. X. Dou, J. L. Wang, D. Q. Shi, X. Xu, M. S. A. Hossain, W. K. Yeoh, S. Choi and T. Kiyoshi, *Supercond. Sci. Technol.* **20** 448, (2007).

Chapter 8: The Doping Effects of Oxygen-free Pyrene on the Superconductivity of MgB₂ Wires

8.1 Presentiment the Doping Effects with Oxygen-free Carbon Source

The discovery of superconductivity in MgB₂ has aroused a great deal of interest in the relevant scientific and application fields. Specifically, its simple binary composition, lack of weak intergranular links, critical temperature (T_c) of 39 K, and the low cost of its starting materials make a MgB₂ a promising candidate for applications at operating temperatures around 20 K. However, pristine MgB₂ exhibits weak flux pinning, which results in a strong field dependence for the critical current density (J_c) and a low irreversibility field (B_{irr}) of ~ 8 T, compared to commercial low temperature superconductors such as the Nb-based ones[1]. It is thus necessary to further improve the J_c and B_{irr} for magnet applications.

Significant results were obtained by adding carbon (C) compounds to MgB₂, resulting in enhancement of both J_c and B_{irr} . In particular, SiC nanoparticles significantly enhanced the J_c under magnetic fields around 8 T. However, the addition of SiC to MgB₂ has been limited by local agglomerations of un-reacted SiC or C (with a size of ~ 30 nm), so it is difficult to achieve uniformly dispersion within the matrix. In our previous work, we first reported the C source possibilities of carbohydrate (malic acid, C₄H₆O₅) through a chemical solution route to achieve homogeneous mixing [2]. It was estimated that intragranular J_c estimated reached 2.5×10^4 Acm⁻² at 5 K and 8 T for

MgB₂ + 10wt% C₄H₆O₅ bulk when sintered at 900°C, with a T_c reduction of only 1.5 K. B_{irr} at 20 K was about 7 T with a J_c criterion of 100 Acm⁻². The advantages of the chemical solution route using various carbohydrates have now been confirmed by other groups[3-5]. However, our understanding of the cause of the significantly enhanced J_c and B_{irr} has still remained unclear due to the complicated reactions involved. In addition, although we conducted evaporation processing to eliminate the oxygen (O) content, the fraction of MgO due to included O from carbohydrate increased gradually with increasing doping level [6]. If we can reduce the MgO fraction within the matrix and find a highly active C source that will be effective at lower sintering temperatures ~600 °C the same as for MgB₂ formation, we speculate that high disorder due to C substitution, as well as strong flux pinning due to small crystalline size, can affect the in-field J_c simultaneously. A higher sintering temperature is usually necessary for most of the other C sources, leading to crystalline growth and worse pinning. The use of low temperature processing is also crucial for selection of various sensitive sheath materials and the reduction of production costs. Although Yamada *et al.* prepared Fe sheathed tape samples through liquid aromatic hydrocarbon as well as by ball-milling [7]; it is very difficult to control the composition during ball milling because of its volatile properties. In this study, therefore, we suggested a different hydrocarbon, pyrene (C₁₆H₁₀) without any oxygen content, as the C source. This is a colourless solid and consists of four fused benzene rings, resulting in a large, flat aromatic system. At around a temperature of 145-148°C, it decomposes separately, and then the highly active hydrogen that has been released may act as an oxygen getter at elevated temperature. In addition, it can be dissolved in a proper solution for homogeneous mixing. To clearly understand the J_c behaviour and superconductivity of MgB₂ using C₁₆H₁₀, the lattice parameters, the actual amount of C substituted, the lattice strain,

MgO fraction, transport J_c , and n -value were evaluated compared to pristine MgB₂/Fe wires.

8.2 Simply Sample Preparation Route

Magnesium (Mg, 99%), boron (B, 99%), and pyrene ($C_{16}H_{10}$, 98%) powders were used as starting materials. The mixed powders were packed into an Fe tube. The composites were drawn to an outer diameter (O.D.) of 1.42 mm. The fabricated wires were sintered at a wide range of temperatures from 600 to 800°C for 30 min to 4 hours under high purity argon (Ar) gas and then cooled in the furnace. The heating rate was 5 °C min⁻¹.

8.3 Phase Information and Lattice Properties

Figure 8.1(a) shows the calculated results for pristine MgB_2 and $\text{MgB}_2 + \text{C}_{16}\text{H}_{10}/\text{Fe}$ wires as a function of the amount of pyrene, $\text{C}_{16}\text{H}_{10}$. All wire samples were sintered at 650°C for 30 min. We observed that the a -axis parameter of $\text{MgB}_2 + \text{C}_{16}\text{H}_{10}/\text{Fe}$ wires decreased gradually with increasing amounts of $\text{C}_{16}\text{H}_{10}$. The shrinkage of the a -axis lattice parameter can be attributed to the substitution of C with small atomic size, which has an effect on disorder in the MgB_2 structure. This kind of disorder potentially changes the properties of MgB_2 [8]. What is interesting is that C substitution into B sites took place even at the low sintering temperature of $\sim 650^\circ\text{C}$. To further clarify the effects of C substitution, we calculated the lattice strain of the structure as a function of amount of $\text{C}_{16}\text{H}_{10}$, as can be seen in Figure 8.1(b). Lattice strain is usually an interesting parameter for quantifying disorder. Estimated strain values at different doping levels showed the opposite trend compared to changes in the a -axis parameter. This indicates that more C substitution introduces higher disorder into the MgB_2 structure. However, the MgO fraction does not increase with increasing doping level. Figure 8.1(c) shows the calculated MgO fraction of pristine MgB_2 and $\text{MgB}_2 + \text{C}_{16}\text{H}_{10}/\text{Fe}$ wires on the base of the Rietveld refinement. At the very least, the MgO fraction for $\text{MgB}_2 + 10\text{wt}\%$ $\text{C}_{16}\text{H}_{10}/\text{Fe}$ wires is less than or similar to that found in the pristine MgB_2 under our experimental conditions. Thus, the MgO effect on the degradation of J_c is at least negligible.

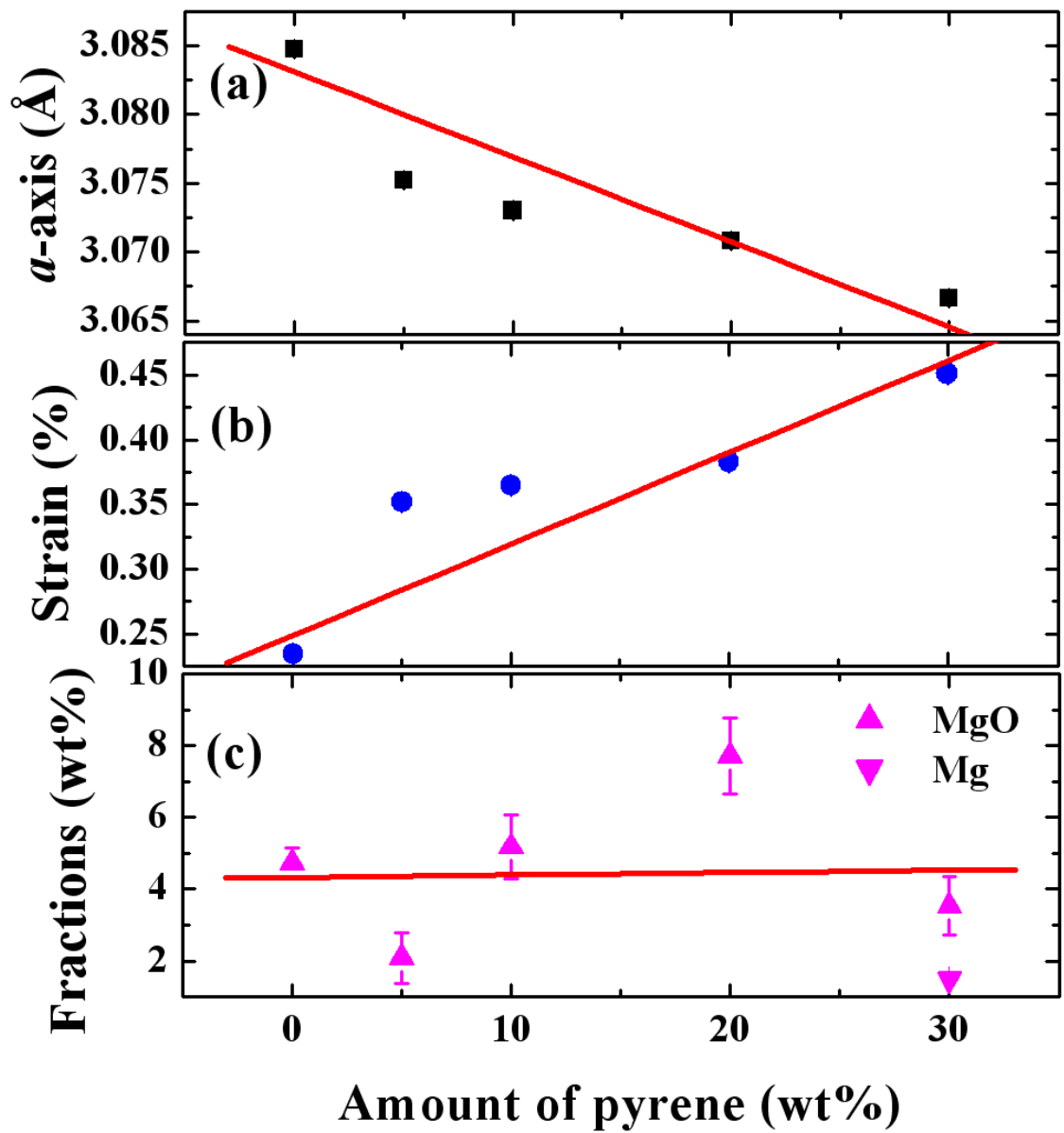


Figure 8.1 (a) a -axis lattice parameter, (b) lattice strain, and (c) fraction of MgO/Mg for pristine MgB_2 and $\text{MgB}_2 + \text{C}_{16}\text{H}_{10}/\text{Fe}$ wires as a function of amount of the pyrene. All wire samples were sintered at 650°C for 30 min. The solid line show a linear fit to the data.

Figure 8.2 shows the calculated results for pristine MgB_2 and $\text{MgB}_2 + 10\text{wt}\%$ $\text{C}_{16}\text{H}_{10}/\text{Fe}$ wires as a function of sintering temperature.

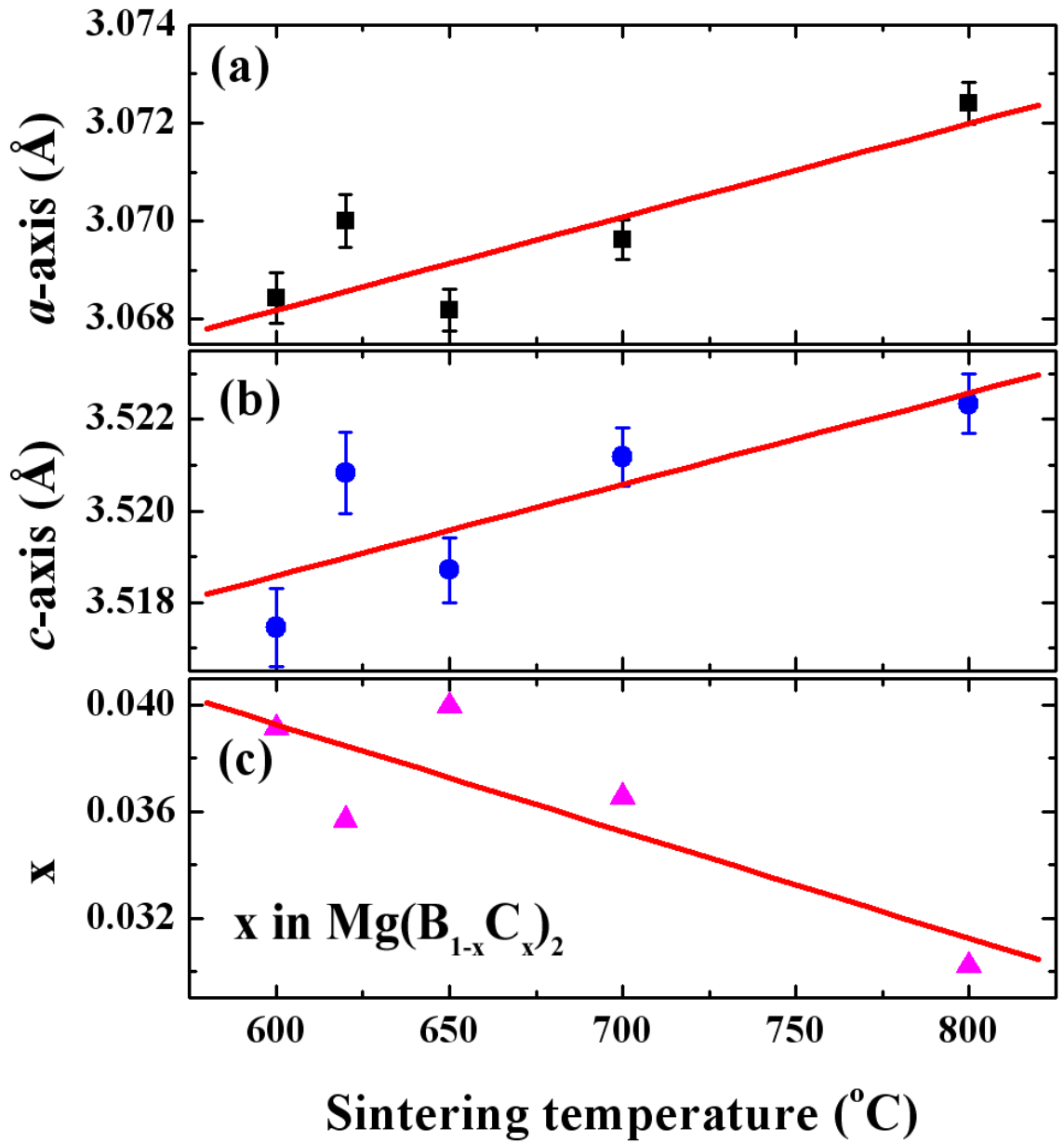


Figure 8.2 (a) a -axis lattice parameter, (b) c -axis lattice parameter, and (c) actual amount of carbon (C) substitution (x) in the composition of $\text{Mg}(\text{B}_{1-x}\text{C}_x)_2$ for pristine MgB_2 and $\text{MgB}_2 + 10\text{wt}\% \text{C}_{16}\text{H}_{10}/\text{Fe}$ wires as a function of sintering temperature. The wire samples were sintered at 600°C for 4 hours, 620°C for 1 hour, 650°C for 30 min, 700°C for 30 min, and 800°C for 30 min, respectively. The solid line show a linear fit to the data.

The wire samples were sintered at 600°C for 4 hours, 620°C for 1 hour, 650°C for 30 min, 700°C for 30 min, and 800°C for 30 min, respectively. What is surprising is that the a -axis parameter of $\text{MgB}_2 + 10\text{wt}\% \text{C}_{16}\text{H}_{10}/\text{Fe}$ wires showed a slightly increased trend from 3.0684 Å to 3.0724 Å with increasing sintering temperature (Figure 8.2(a)). However, this is not a typical phenomenon. Common C additives, such as C, SiC, and

carbon nanotube (CNT), can achieve much more C substitution into the MgB_2 structure as the sintering temperature further increases, resulting in enhanced B_{irr} and J_c . This unusual trend is probably because highly active C is much easier to evaporate with increasing temperature. The c -axis parameter also mimics the change in the a -axis one (Figure 8.2(b)). Obviously, a low sintering temperature can give rise to higher disorder in the MgB_2 structure, leading to broadening of the diffraction peaks. This implies combined effects of crystalline size reduction and increased lattice strain. Specifically, the crystalline size of MgB_2 superconductor can be attributed to the number of grain boundaries. Based on changes in the a -axis parameter, the actual amount C substitution can be estimated by comparing the calculated value with that of a single crystal. The actual C substitution for the sample sintered at 600°C was about $x \sim 0.03913$ in the composition of $\text{Mg}(\text{B}_{1-x}\text{C}_x)_2$ [15]. As a result, the maximum C substitution level can be easily achieved at a low sintering temperature, $\sim 600^\circ\text{C}$ under our experimental conditions (Figure 8.2(c)). At this temperature, the much greater amount of C substituted on the B sites introduces strong electron scattering centres that reduce the electron mean free path and thus could significantly enhance B_{irr} .

8.4 Transport Critical Current (J_c)

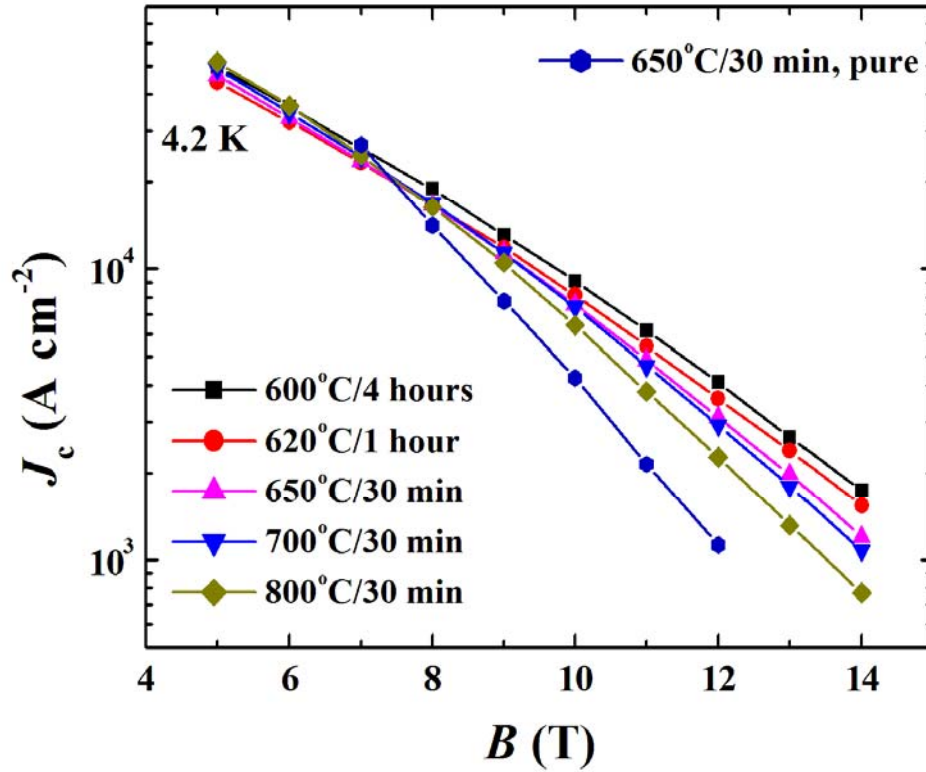


Figure 8.3 Transport critical current density (J_c) of pristine MgB_2 and $\text{MgB}_2 + 10\text{wt}\%$ $\text{C}_{16}\text{H}_{10}/\text{Fe}$ wires as a function of applied magnetic field and sintering temperature.

Figure 8.3 shows the transport J_c of pristine MgB_2 and $\text{MgB}_2 + 10\text{wt}\%$ $\text{C}_{16}\text{H}_{10}/\text{Fe}$ wires sintered within a temperature range of 600°C to 800°C . The J_c of $\text{MgB}_2 + 10\text{wt}\%$ $\text{C}_{16}\text{H}_{10}/\text{Fe}$ wires gradually decreased as the sintering temperature increased. This is because grain boundaries are likely to be acting as the predominant pinning centers. In addition, the amount of C substitution decreased with increasing sintering temperature. Note that J_c of $\text{MgB}_2 + 10\text{wt}\%$ $\text{C}_{16}\text{H}_{10}/\text{Fe}$ wires was higher than that of pristine MgB_2 wire under magnetic field from 7 T to 12 T. Transport J_c did not show any large

differences among $\text{MgB}_2 + 10\text{wt}\% \text{C}_{16}\text{H}_{10}$ wire samples. As a result, the C doped sample sintered at 600°C showed better J_c performance when we used $\text{C}_{16}\text{H}_{10}$.

8.5 Power-Law Relationship between J_c and n -value

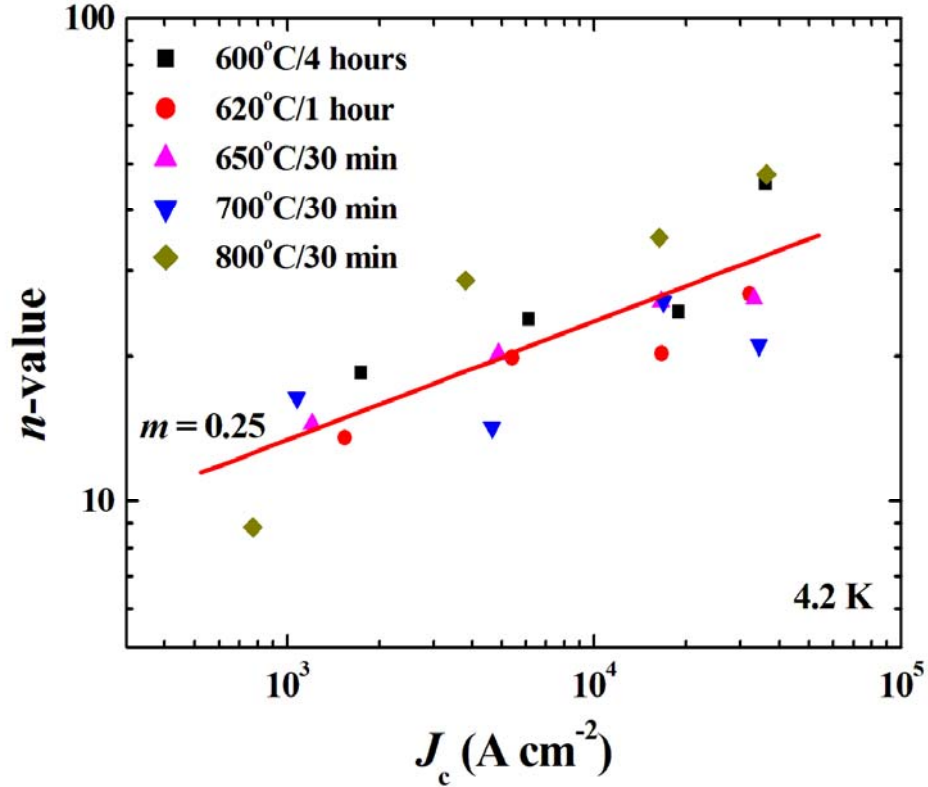


Figure 8.4 Power-law relationship between J_c and n -value, $n \propto J_c^m$.

In order to further improve the stability of the conductor for real applications. Thermal as well as electrical dissipations must be minimized, which mainly occurs due to the small n -value characteristic of MgB₂ superconductor.

Figure 8.4 shows the power-law relationship between J_c and the n -value, $n \propto J_c^m$. The n -values were determined from the slope in the plot of $\log E$ (electric field) versus $\log J$ in the E range from 0.1 to 1 μVcm^{-1} based on the power law $E_c = E(V/V_c)^n$. In general, the n -value is conventionally used to characterize the sharpness of the superconducting transition, which is affected by the intrinsic and extrinsic properties of the

superconductor [9, 10]. The n -value also decreases gradually with increasing magnetic field. As can be seen in Figure 8.4, we found that there was a closer relationship between the n -value and the J_c , $n \propto J_c^m$. m was approximately 0.25 for all samples. However, the m value increased from 0.25 to 0.41 with increasing sintering temperature. What is interesting is that the exponent m becomes higher for the higher n -value samples [10]. Obviously, a smaller m value in the log-log plot of $n \propto J_c^m$ can be attributed to a highly disordered structure due to low sintering temperature and more C substitution.

8.6 Summary

In summary, using $C_{16}H_{10}$ is effective for enhancing J_c of MgB_2 superconductor, even at low sintering temperatures as low as 600°C . Specifically, the J_c of the sample sintered at 600°C for 4 hours was $\sim 10000 \text{ Acm}^{-2}$ at 10 T and 4.2 K. The advantages of using $C_{16}H_{10}$ include the production of highly active C due to decomposition of the pyrene and the introduction of small grain size due to low temperature sintering, resulting in enhancement of J_c . In addition, a power-law relationship between J_c and the n -value is observed in the log-log plot of $n \propto J_c^m$. The exponent m becomes higher for the higher n -value samples. Obviously, smaller m also reflects higher disorder due to low sintering temperature and more C substitution.

8.7 References

1. Y. Iwasa, D. C. Larbalestier, M. Okada, R. Penco, M. D. Sumption, and X. Xi, *IEEE Trans. Appl. Supercond.* **16** 1457, (2006).
2. J. H. Kim, S. Zhou, M. S. A. Hossain, A. V. Pan, and S. X. Dou, *Appl. Phys Lett.* **89** 142505, (2006).
3. Z. S. Gao, Y. W. Ma, X. P. Zhang, D. L. Wang, Z. G. Yu, K. Watanabe, H. A. Yang, and H. H. Wen, *Supercond. Sci. Technol.* **20** 485, (2007).
4. B.-H. Jun, and C.-J. Kim, *Supercond. Sci. Technol.* **20** 980, (2007).
5. Z. S. Gao, Y. W. Ma, X. P. Zhang, D. L. Wang, Z. G. Yu, H. Yang, H. H. Wen, and E. Mossang, *J. Appl. Phys.* **102** 013914, (2007).
6. J. H. Kim, S. X. Dou, M. S. A. Hossain, X. Xu, J. L. Wang, D. Q. Shi, T. Nakane, and H. Kumakura, *Supercond. Sci. Technol.* **20** 715, (2007).
7. H. Yamada, M. Hirakawa, H. Kumakura, and H. Kitaguchi, *Supercond. Sci. Technol.* **19** 175, (2006).
8. S. Lee, T. Masui, A. Yamamoto, H. Uchitama, and S. Takama, *Physica C* **397** 7, (2003).
9. H. Kitaguchi, A. Matsumoto, H. Hatakeyama, and H. Kumakura, *Physica C* **401** 246, (2004).
10. D. M. J. Taylor and F. P. Hampshire, *Supercond. Sci. Technol.* **18** S297, (2005).

Chapter 9: Properties of Carbon Spheres doped MgB₂ Wire by Low Purity Boron powder

9.1 Possibility of Carbon Source Doping Effects in Low Purity Boron

One promising application of the MgB₂ superconductor is the next generation MRI magnet that can work at 20-25 K, a temperature range can be readily reached by a cryogen-free cryocooler [1]. Indeed, a huge amount of works have been done to improve the current carrying capability of MgB₂ wires/tapes, so that they can be used to construct the magnets [2, 3]. Generally, the attempts trying to improve the current transport properties of MgB₂ superconductor can be divided into two groups: improving the core density, hence the connectivity by optimizing the material processing parameters [4, 5]; and improving the flux pinning ability in high magnetic field by artificially introducing flux pinning centres, such as defects and precipitates [6, 7]. The former idea was based on the fact that volume shrinkage would occur during the *in situ* formation of MgB₂, so reducing the pores and voids by optimizing the thermo mechanical process could greatly increase the core density and transport property. The latter group of works were aiming at improving the flux pinning ability and upper critical field, so as to improve the J_c properties of MgB₂ superconductor.

. In this work, the doping effect of reactive submicron-sized carbon spheres (CS), which were prepared by hydrothermal treatment of glucose solution, on the properties of MgB₂ superconductor was investigated.

Another important issue for the current MgB_2 study is the quality of the starting boron powders. High purity amorphous boron with small particle size was believed ideal for preparation of MgB_2 in terms of high phase purity and better superconducting properties.. However, as such kind of high quality boron powders is rare and also very expensive, we have to consider starting from low purity boron powders to prepare MgB_2 superconductor. To begin with, the difference between using the low grade and high quality boron powders should be studied first. In this chapter, we chose a boron powder with only 96% purity and with crystalline phase as the starting boron source. The possible reasons for the low quality MgB_2 samples prepared from this low purity boron will be discussed.

9.2 Carbon Spheres Preparations

The carbon spheres were prepared by hydrothermal treatment of glucose solution at 180°C for 20 h in a Teflon-lined stainless steel autoclave [8]. Figure 9.1 shows the SEM image of the as-prepared carbon spheres. The typical size of the carbon spheres are between 250-300 nm. We can also see some big spheres in a diameter of about 1000 nm.

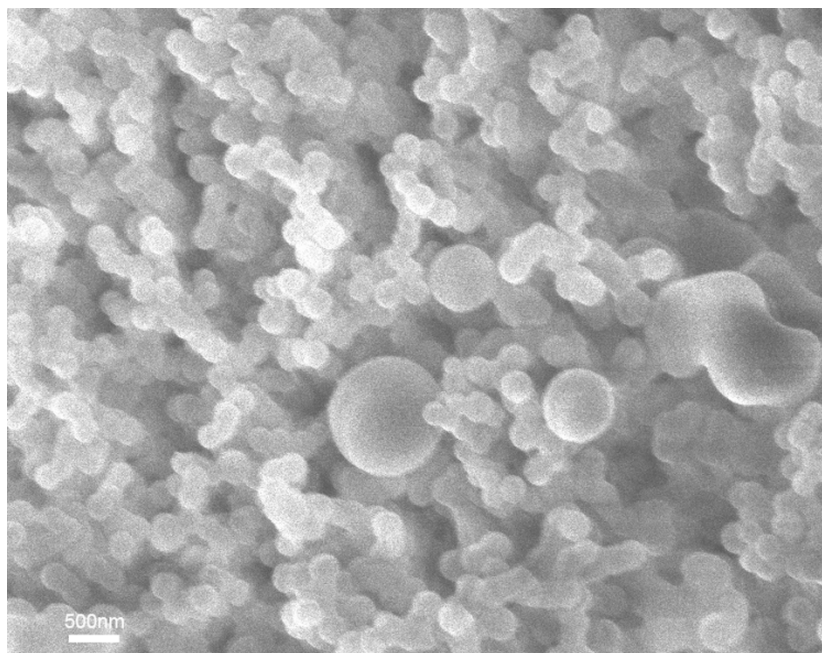


Figure 9.1 SEM image of the submicron-sized carbon spheres prepared by hydrothermal treatment of glucose solution at 180°C.

9.3 MgB₂ Wire Preparations

To prepare MgB₂ superconductor, stoichiometric magnesium (99%, about 40 μm) and boron (96%, 1.27 μm with average, Tangshan, China) powders were manually mixed with the carbon spheres in a weight ratio of 0, 5, and 10 wt%, respectively. The mixed powders were packed into pure iron tubes, which were then deformed into thin wires with a diameter of 1.4 mm. Short wires of 4 cm each were cut and sintered at 650 to 800°C for 30 min under flowing argon. A reference sample was also prepared from high purity amorphous boron (99%, about 100 nm). The cylinder shaped superconducting cores were mechanically taken out from the wires and subjected to magnetic and resistivity measurements. The applied DC current for resistivity measurement was 0.5 mA. T_c was obtained from measurements of AC susceptibility (amplitude =1 Oe). The XRD measurements were carried out on ground fine MgB₂ powders to minimize the influence of texture. The lattice parameters were calculated by Rietveld refinement method using the Jade 5.0 program (XRD pattern processing). Bean model was used to calculate the magnetic critical current density. The upper (H_{c2}) and irreversible (H_{irr}) critical fields were determined as the 10% and 90% transition on the resistivity-temperature (R - T) curves.

9.4 Comparison between MgB₂ Wires by High and Low Purity Boron without Doping

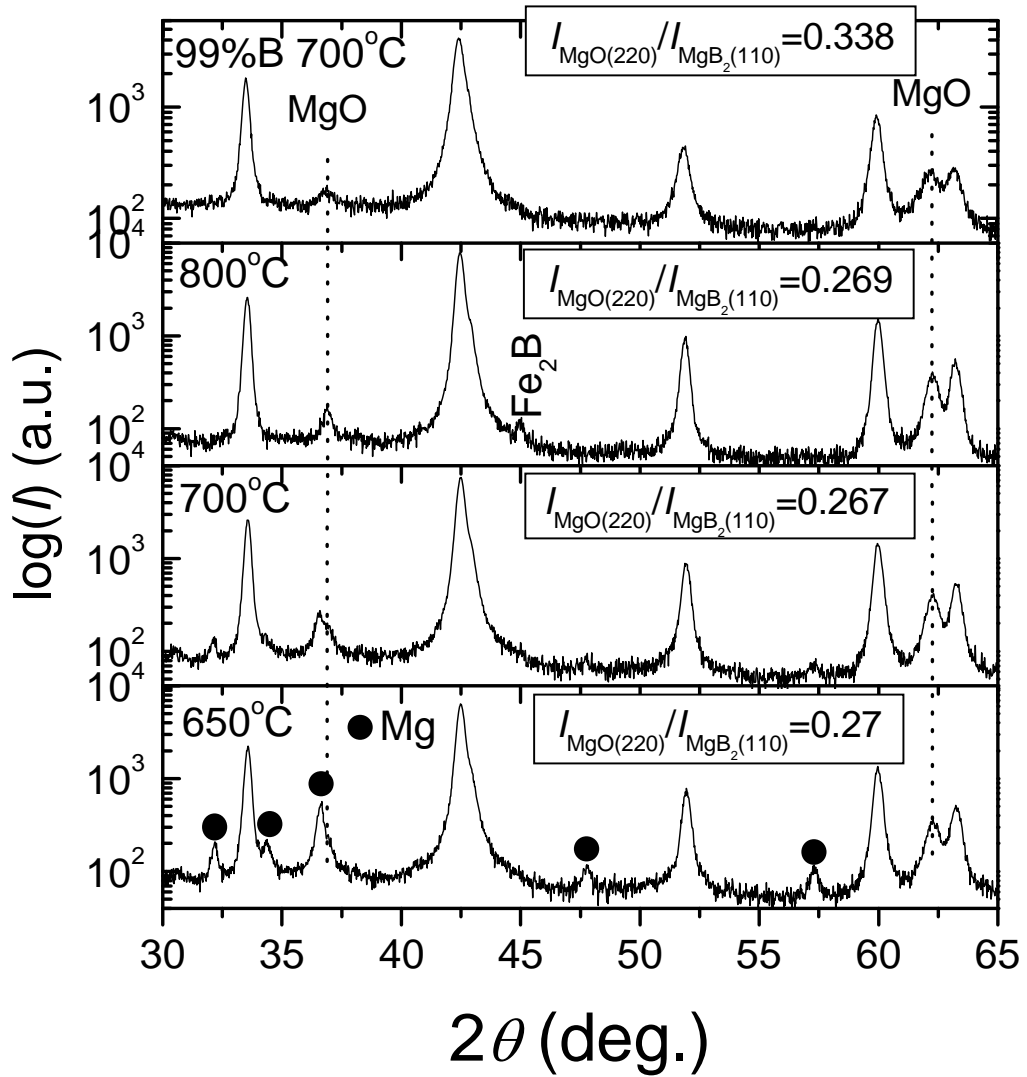


Figure 9.2 XRD patterns of the pure MgB₂ samples prepared by sintering at different temperatures.

Figure 9.2 shows the XRD patterns of the undoped samples that were sintered at different temperatures. The XRD pattern of the sample prepared from 99% amorphous boron and sintered at 700°C is also included. In order to see clearly the peaks of the

impurity phases, the intensity of the XRD patterns is plot in the logarithmic form. As can be seen, the sample sintered at 650°C contains a large portion of unreacted magnesium. Even in the sample sintered at 700°C, we can still observe Mg peaks. As has been discussed in our previous work [5], high phase purity MgB₂ could be obtained after 1 h annealing at 600°C when using high purity amorphous boron powders. The sample starting from 99% amorphous boron and sintered at 700°C also shows very high purity MgB₂ except MgO. The relative amount of MgO to MgB₂ in each sample was estimated by the intensity ratio of (220) peak and (110) peak of MgO and MgB₂, respectively. The data are listed in Fig. 2. The ratios, $I_{\text{MgO}(220)}/I_{\text{MgB}_2(110)}$, of the samples prepared from the low grade boron are almost the same, which are even lower than that of the sample prepared from the high purity amorphous boron. This suggests that oxidation is not the major problem of the low grade boron. One of the major differences between the high purity amorphous boron and the low grade boron used in this study is the low reactivity of the latter towards MgB₂ phase formation, which might be caused by the larger particle size, the existence of crystalline boron and boron oxide. The higher MgO content in the sample prepared from 99% boron might be due to the smaller grain size of MgB₂ resulted from the smaller size of the starting boron. The MgO formed during *in situ* reaction covers on or precipitates in MgB₂ grains. Because of the smaller MgB₂ grains, more MgO was exposed to x-ray diffraction, which subsequently increased the intensities of MgO peaks. The degree of amorphous and particle size of the boron powders have been proven of vital importance, as mechanical alloying using high energy ball mill can greatly improve the reactivity of the low purity boron by reducing the particle size and increasing amorphous boron phase.

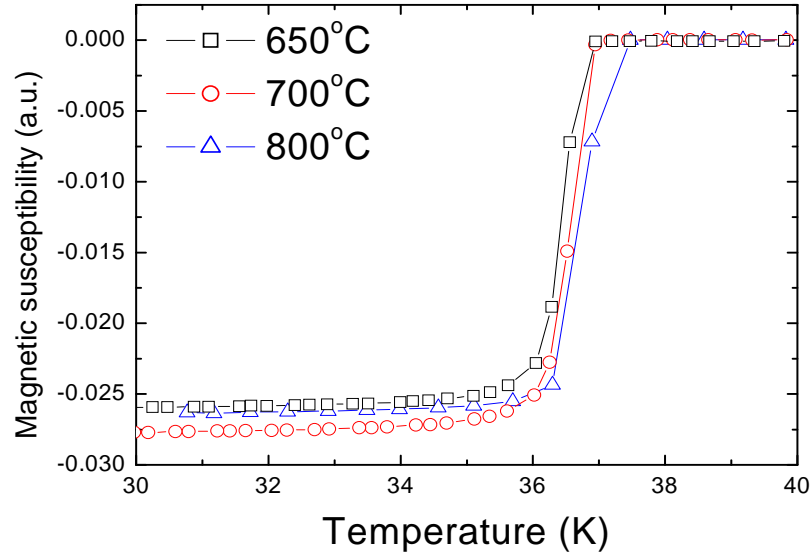


Figure 9.3 Magnetic AC susceptibility as a function of temperature for the pure samples sintered at different temperatures.

The T_c curves of the undoped samples, as determined by DC magnetization measurement, are shown in Figure 9.3. The onset T_c of the samples sintered at 650 and 700°C are 37 K, which is only 0.5 K lower than that sintered at 800°C. The slight increase of T_c can be ascribed to the improved crystallinity of the MgB_2 grains in the latter. However, as has been reported previously, a better crystallinity usually corresponds to a worse current transport properties at high magnetic field [9, 10].

Figure 9.4 plots the field dependence of the magnetic J_c properties at 5 and 20 K for the undoped samples sintered at 650, 700 and 800°C, respectively. The J_c properties of the sample prepared from 99% amorphous boron and sintered at 700°C are also shown in this figure. It is clear to see that, even though there is a large portion of unreacted Mg in the sample sintered at 650°C, which means it has the lowest volume fraction of MgB_2 , the J_c property of this sample is the best at high field. This might be due to the higher upper critical field of this sample, as will be discussed later. Increasing the heat treatment temperature, the J_c properties of the MgB_2 samples are improved at low

magnetic field, which are consistent with the better grain connectivity. At both 5 and 20 K, the sample prepared from high purity amorphous boron show much higher in-field J_c properties.

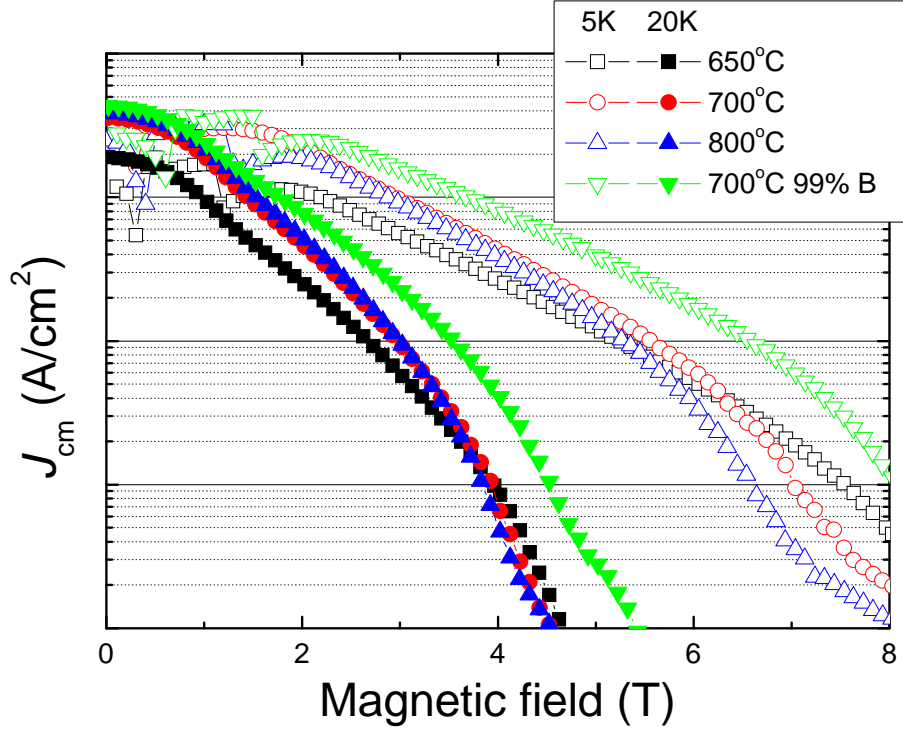


Figure 9.4 Critical current density, J_{cm} , as a function of magnetic field at 5 and 20 K for the undoped samples sintered at different temperatures. The J_{cm} of the sample (700°C) prepared from high purity (99%) amorphous boron is included as reference.

However, at 20 K and in low field (< 1 T), the samples made from the low grade boron and sintered at high temperatures show comparable J_c values to that prepared from the high quality boron. This demonstrates that the low grade boron is applicable for preparation of MgB_2 for low field use, such as MRI magnets. It should be pointed that our samples were prepared by hand mixing of the boron and magnesium powders for a few minutes and reacted in wires prepared by the conventional *in situ* powder-in-tube method without any pressure. So the absolute J_c values were still low. However, as reported by Herrmann et al, high energy ball milling and reactive sintering with pressure can increase the J_c values in magnitude. We believe that by using these techniques the J_c

properties of the MgB_2 superconductor prepared from this low grade boron can be improved to an acceptable level.

The upper and irreversible fields of the samples are shown in Figure 9.5 as a function of temperature. In comparison to the sample sintered at 800°C , the sample sintered at 650°C shows a slight increase in both H_{c2} and H_{irr} . This can be attributed to the larger crystal disorder in the low temperature sintered sample due to a poor crystallinity and small grain size. The larger amount of impurity phases in the sample sintered at 650°C , such as Mg and B, may also increase the electron scattering, hence the critical fields of MgB_2 . The higher H_{c2} of the sample sintered at 650°C may explain its higher J_c values in high field. The sample prepared from 99% boron shows much higher H_{c2} and H_{irr} , which might be also the major reason for its high in-field J_c properties.

9.5 Carbon Spheres doped MgB₂ Wires by the Low Purity Boron

In this section all “pure” means MgB₂ wire was made by 96% boron powder without doping.

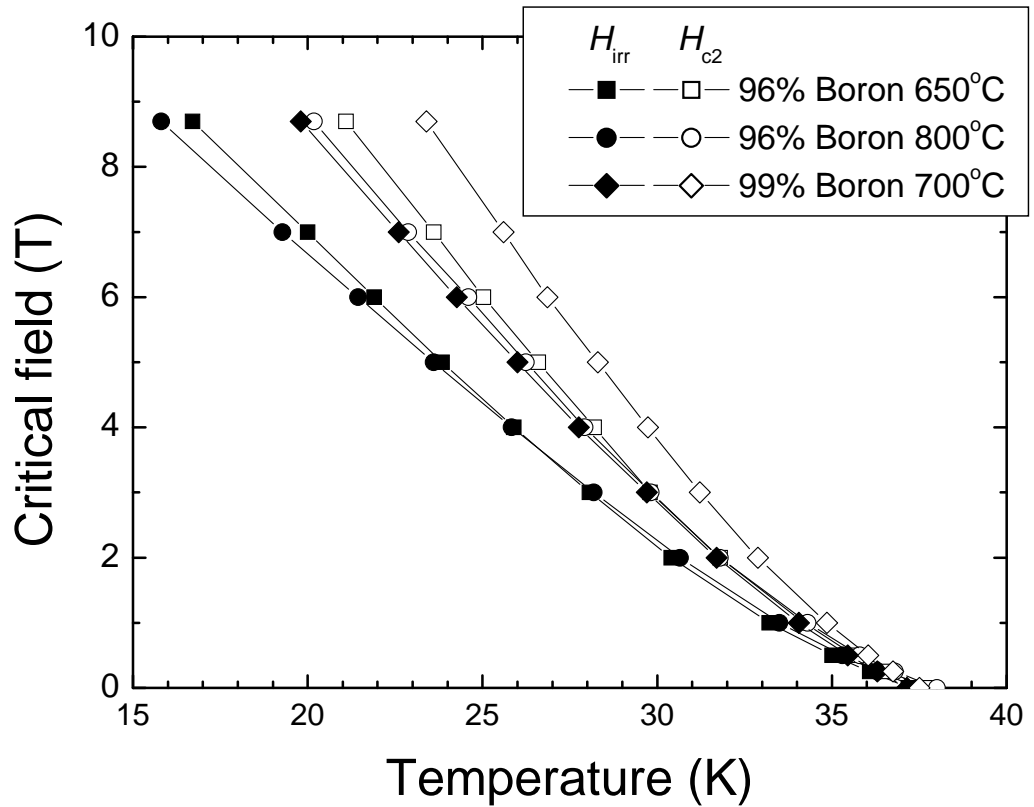


Figure 9.5 Temperature dependence of H_{c2} and H_{irr} for the pure samples sintered at 650 and 800°C, and the sample prepared from 99% amorphous boron sintered at 700°C.

Figure 9.6 plots the (002) and (110) XRD peaks of the pure, 5 and 10 wt% carbon spheres doped MgB₂ samples. The sintering temperature for these samples is 800°C. As can be seen, the (110) peaks are systematically shifted to higher 2θ angle with increase of the amount of carbon spheres. This suggests that the submicron-sized carbon spheres have successfully reacted with boron and resulted in carbon substitution on the boron site in MgB₂. Table 9.1 summarizes the characteristic data, such as the transition

temperature, transition width, a - and c - axis parameters, the actual carbon concentrations, resistivity at 40 K, grain size and strain, in the pure and CS doped samples. The actual substitution ratios of carbon for boron (x in $\text{MgB}_{2-x}\text{C}_x$) in the 5 and 10 wt% CS doped samples, as determined by the reduction ratio of a -axis parameter, are 0.018 and 0.045, respectively. The substitution levels are comparable to those of nano-C doped samples [11].

This means that the carbon spheres are reactive enough to introduce carbon doping in MgB_2 although they have smaller interface with the boron powders due to the larger particle size. The transition temperatures of the CS doped samples (determined by DC magnetization measurements) are decreased in comparison to the undoped sample. Meanwhile, the transition widths are much larger, namely 4.1-4.9 K. The decreased T_c and widened T_c transition suggest that carbon has indeed entered the MgB_2 crystal lattice. Meanwhile, the carbon substitution might be not homogeneous in each grain; the gradient of carbon concentration has thus increased the transition width. Also, in comparison to the added CS, the actual carbon content in $\text{MgB}_{2-x}\text{C}_x$ is very small; therefore, a large portion of the added carbon spheres must have acted as impurities, which can also widen the T_c transition. As an evidence, the resistivity at 40 K of the pure, 5, and 10 wt.% CS-doped samples are 26, 41, and 101 $\mu\Omega$ cm, respectively (see table 9.1). The resistivity is increased by increasing the doping level of carbon spheres, which is possibly due to the increased electrons scattering as a consequence of more crystal lattice defects and unreacted carbon impurities.

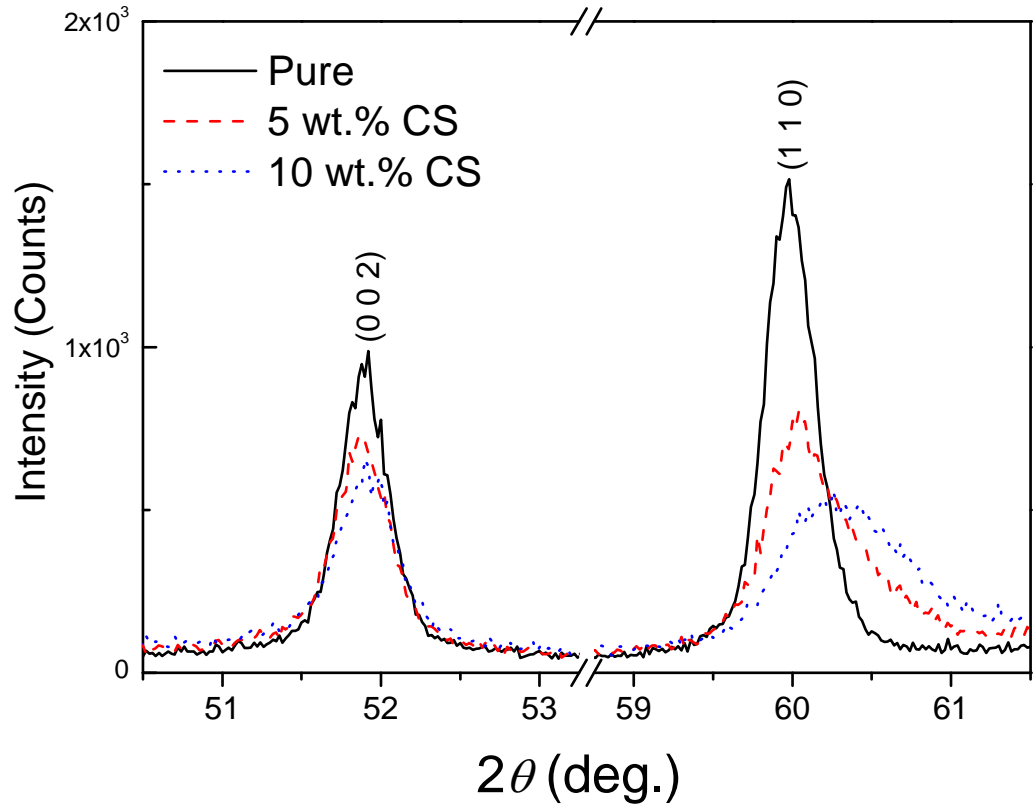


Figure 9.6 The (002) and (110) XRD reflections of the pure, 5 and 10 wt.% CS doped samples. The heat treatment temperature for these samples is 800°C.

Sample	T_c (K)	ΔT_c (K)	a -axis (Å)	c -axis (Å)	Estimated C concentration $MgB_{2-x}C_x$	ρ_{40K} ($\mu\Omega$ cm)	Grain size (nm)	Strain (%)
MgB_2	37.5	1.2	3.0836	3.5236	-	26	348	0.2451
MgB_2 +5wt.% CS	36.5	4.1	3.0827	3.5219	0.018	41	273	0.3431
MgB_2 +10wt.% CS	33.8	4.9	3.0765	3.5233	0.045	101	247	0.3878

Table 9.1 Summaries of characteristic data for the pure and CS doped MgB_2 samples sintered at 800°C

From table 9.1, we can also see that the size of MgB_2 grains is decreased with CS doping. There are two possible reasons to account for this particle size reduction. For one reason, the added CS may act as barriers to prevent Mg diffusion and grain growth. For a second reason, lattice distortion induced strain as the result of carbon substitution in boron honeycomb may also hinder the growth of MgB_2 grains.

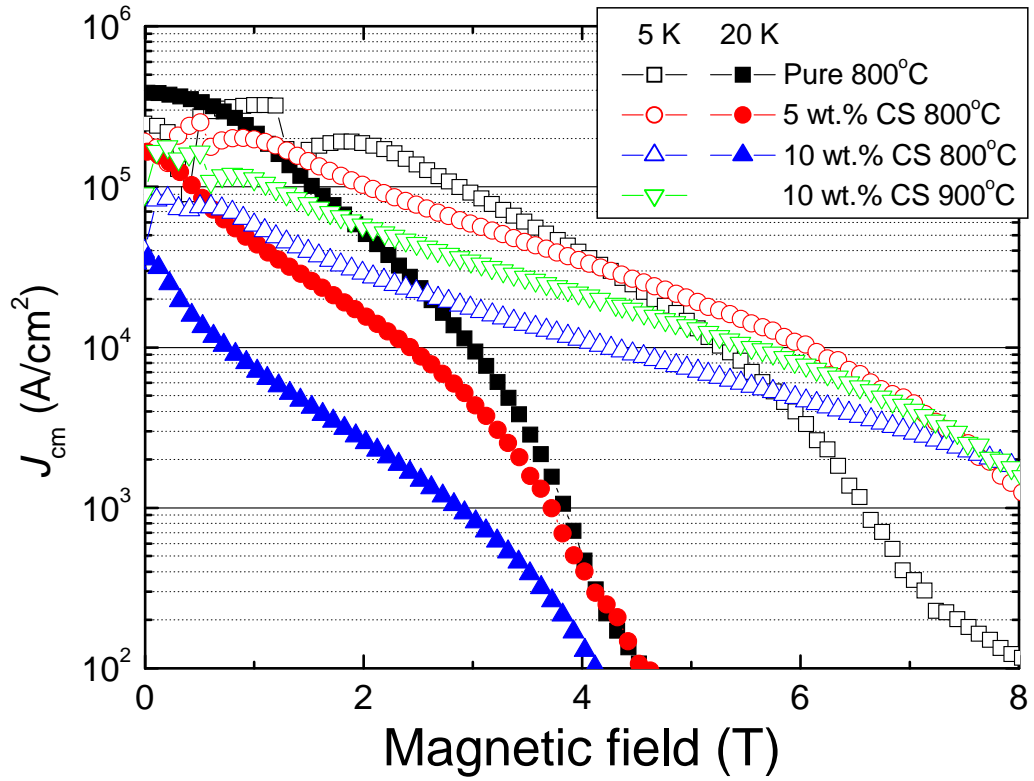


Figure 9.7 Critical current density, J_{cm} , as a function of magnetic field at 5 and 20 K for the pure and CS doped samples.

Figure 9.7 shows the field dependence of magnetic J_c properties of the pure and CS doped samples at 5 and 20 K. At 5 K, J_c enhancement in high magnetic field by the addition of CS can be clearly observed. For example, the enhancement is more than a magnitude at 8 T. The sample doped with 5 wt.% CS shows higher J_c than that doped with 10 wt.% CS in low fields. The latter shows very poor J_c in low magnetic field; however, its J_c surpasses that of the sample doped with 5 wt.% CS at 8 T. This result suggests that although increasing the doping level of CS to 10 wt.% can introduce more carbon substitution, hence leading to higher H_{c2} , however, more impurities can also be created, which destroys the grain connectivity and so forth decreases the J_c properties. The pure sample exhibits the best J_c at 20 K. This is because of the low T_c of the CS

doped samples, which suppresses the superconductivity near the T_c . However, from Fig. 9.7 we can still observe the flattening of the J_c -B curves of the doped samples, which should be attributed to the enhanced upper critical fields.

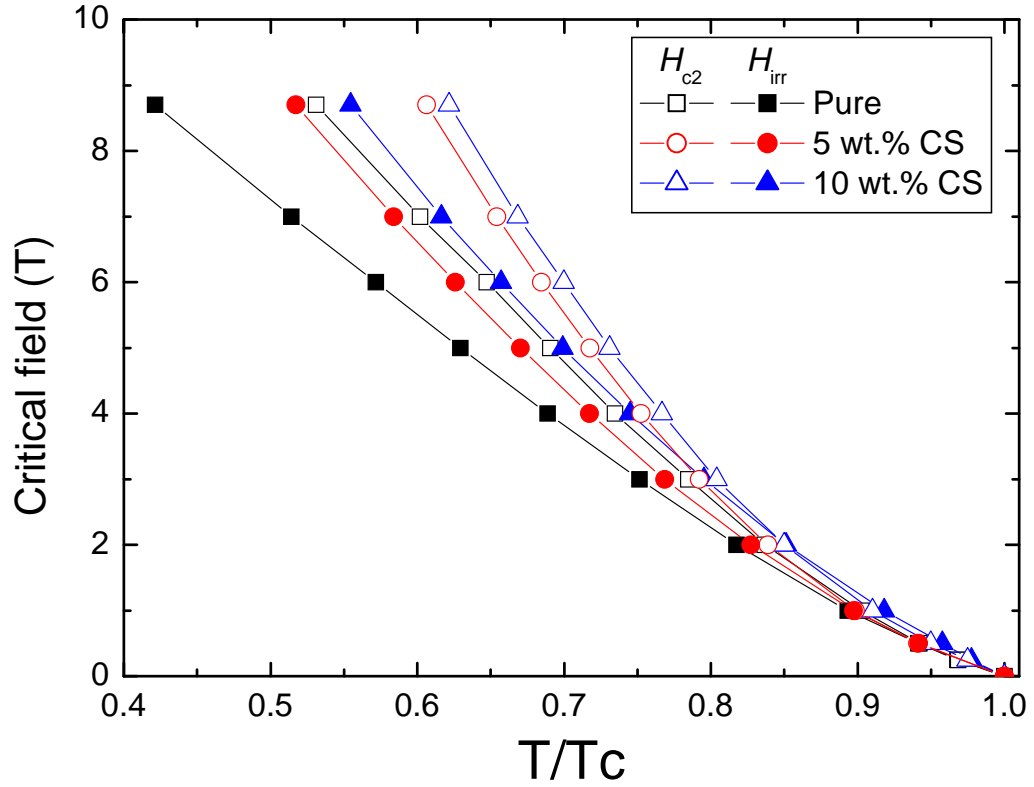


Figure 9.8 The H_{c2} and H_{irr} of the pure and CS doped samples sintered at 800°C as a function of reduced temperature (T/T_c).

Figure 9.8 depicts the H_{c2} and H_{irr} values of the pure and CS doped samples as a function of the reduced temperature. Clearly, the critical fields were greatly increased by the CS doping. For example, at 20 K, the H_{c2} and H_{irr} of the pure sample are 8.9 and 6.7 T, respectively. Whereas the H_{c2} and H_{irr} of the sample doped with 10 wt% CS are estimated to be 11.7 and 8.0 T, respectively. These values are even higher than those of nano-structured carbon doped samples achieved by high energy ball milling. As discussed above, carbon has been successfully doped into MgB_2 , which caused lattice distortion, as evidenced by the increased relative strain (see table 1), and so forth

changed the intrinsic properties, such as intra-band and inter-band scattering, of the MgB₂ superconductor [12].

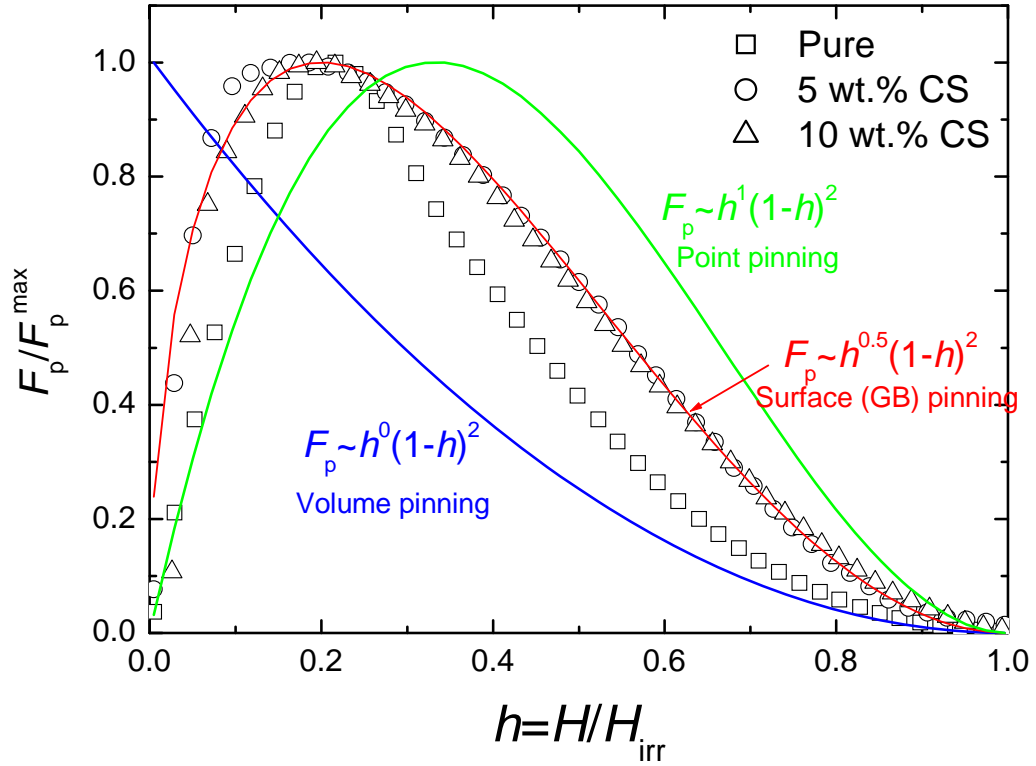


Figure 9.9 Normalized flux pinning force as a function of reduced magnetic field at 20 K for the pure and CS doped samples sintered at 800°C. The solids lines corresponds to the function $h^p(1-h)^q$ with different p and q values representing different pinning mechanisms.

The normalized volume flux pinning forces F_p/F_p^{\max} at 20 K for the pure and CS doped samples are plotted in Figure 9.9 against the reduced magnetic field ($h=H/H_{\text{irr}}$). Here H_{irr} was obtained by linear extrapolation to zero of the low- J_c segment of the Kramer curves, $J_c^{1/2}H^{1/4}(H)$ [13]. Dew-Hughes proposed a general relation: $F_p(h) = F_p/F_p^{\max} \propto h^p(1-h)^q$, to assess the pinning mechanisms in superconductor [14]. Different types of pinning mechanisms are described by different values of p and q , as indicated by the solid lines in Fig. 9.9. As can be seen, the pinning forces reached a maximum at $h^{\max} = 0.18 - 0.217$ for all the samples. The pinning curves of the CS-doped samples were well-reproduced by the function $h^{0.5}(1-h)^2$, suggesting that the dominant pinning type

might be grain boundary pinning. However, the pinning curve of the pristine sample cannot be fitted by any unique pinning mechanism as proposed in [14]. This might be a sign of the changed flux pinning in CS-doped samples. It may be pointed out that the Dew-Hughes model is initially proposed for low temperature superconductors where identical properties for all grains are essential. For MgB_2 , however, the anisotropy and grain connectivity also influence the pinning curves in conjunction with pinning types, which makes the discussion of flux pinning based on this model very arguable. For example, some fittings to the experimental data give q values larger than 2, which cannot be explained in the framework of present model [13–16]. Therefore, the result on pinning type based on Fig. 9.9 can only broadly indicate that the CS-doped samples show high pinning force at larger reduced field.

It is worthy to note that, unlike nano-carbon doping [24], increasing the processing temperature of CS-doped samples to 900°C did not further increase the upper critical field and irreversible field, although it did improve the J_c property in the whole field region, as shown in Fig. 9.8. In other words, increasing the sintering temperature has only improved the grain connectivity but not the carbon doping level. It is assumed that a saturation of carbon substitution has been reached, possibly due to the small contact area between the carbon spheres and boron powders.

9.6 Conclusion

The superconducting properties of pure and submicron-sized carbon spheres doped MgB_2 prepared from low purity boron powders were studied. In comparison to high purity amorphous boron, the low grade boron showed low reactivity towards MgB_2 formation. However, at 20 K and in low field (< 1 T), the J_c values were comparable to that of the sample prepared from high quality boron. It is believed that using high energy ball milling method can further increase the J_c properties to acceptable level. The submicron-sized carbon spheres prepared by hydrothermal process can successfully induce carbon substitution for boron within a short reaction time, which greatly improved the H_{c2} and H_{irr} , and so forth in-field J_c properties of the MgB_2 superconductor. It is believed that doping carbon spheres had effectively changed the intrinsic properties of MgB_2 and also reduced the grain size, both of which were responsible for the enhanced upper critical field and flux pinning force.

9.7 References

1. K. Vinod, R. G. A. Kumar, and U. Syamaprasad, *Supercond. Sci. Technol.* **20** R1, (2007).
2. R. Flukiger, H. L. Suo, N. Musolino, C. Beneduce, P. Toulemonde, and P. Lessa, *Physica C* **385** 286, (2003).
3. H. Kumakura, A. Matsumoto, T. Nakane, and H. Kitaguchi, *Physica C* **456** 196, (2007).
4. C. H. Jiang, H. Hatakeyama, and H. Kumakura, *Supercond. Sci. Technol.* **18** L17, (2005).
5. C. H. Jiang, S. X. Dou, and H. Kumakura, *Supercond. Sci. Technol.* **20** 1015, (2007).
6. Y. Bugoslavsky, L. F. Cohen, G. K. Perkins, M. Polichetti, T. J. Tate, R. Gwilliam, and A. D. Caplin, *Nature* **411** 561, (2001).
7. X. Z. Liao, A. C. Serquis, Y. T. Zhu, J. Y. Huang, D. E. Peterson, F. M. Mueller, and H. F. Xu, *Appl. Phys. Lett.* **80** 4398, (2002).
8. X. M. Sun, and Y. D. Li, *Angew. Chem. Int. Ed.* **43** 3827, (2004).
9. A. Yamamoto, J. Shimoyama, S. Ueda, Y. Katsura, I. Iwayama, S. Horii, and K. Kishio *Physica C* **445** 806, (2006).
10. C. H. Jiang, T. Nakane, and H. Kumakura, *Appl. Phys. Lett.* **87** 252505, (2005).
11. W. K. Yeoh, J. Horvat, J. H. Kim, X. Xu, and S. X. Dou, *Appl. Phys. Lett.* **90** 122502, (2007).
12. C. Krutzler, M. Zehetmayer, M. Eisterer, H. M. Weber, N. D. Zhigadlo, J. Karpinski, and A. Wisniewski, *Phys. Rev. B* **74** 144511, (2006).
13. E. Martínez, P. Mikheenko, M. Martínez-López, A. Millán, A. Bevan, and J. S. Abell, *Phys. Rev. B* **75**, 134515, (2007).

14. D. Dew-Hughes, *Philos. Mag. B* **55**, 459, (1987).
15. C. Tarantini, H. U. Aebersold, C. Bernini, V. Braccini, C. Ferdeghini, U. Gambardella, E. Lehmann, P. Manfrinetti, A. Palenzona, I. Pallecchi, M. Vignolo, and M. Putti, *Physica C* **463-465** 211, (2007).
16. O. V. Shcherbakova, A. V. Pan, J. L. Wang, A. V. Shcherbakov, S. X. Dou, D. Wexler, E. Babic, M. Jercinovic, and O. Husnjak, *Supercond. Sci. Technol.* **21** 015005, (2007).

Chapter 10: Conclusions and Further Work

10.1 Conclusion

It has been shown that the critical current density of MgB_2 is strongly dependent on the starting boron precursor powder. Furthermore, it is also demonstrated that the critical current density can be optimized by using a ball-milling process and chemical additions such as carbon source doping .

The purity of the starting boron powders are important in determining the $J_c(H)$ performance of an MgB_2 sample: the purer the starting boron powders, the better the $J_c(H)$ performance. However, compared to the pure 99% powder used in this work, the low purity boron powders still showed more oxide impurities, lower surface reactivity, less uniform grain distributions, and larger grain size.

The effects of B powders that were ball milled in different media, such as acetone, ethanol, and toluene, on the superconducting properties of MgB_2 were systematically evaluated. Specifically, ball milling B in toluene leads to smaller MgB_2 grains, resulting in enhanced J_c under high field.

There was strong evidence that the particle size of the starting B powders is important in determining the $J_c(B)$ performance of MgB_2 samples. The reactivity of 96% B powder can be improved by using ball-mill processing, leading to enhanced magnetic critical current density, J_c , compared to the original 96% B powder. The different A_F values can explain the connectivity effects in the ball-milled samples: when the ball-milling time is increased, the grain connectivity becomes worse, leading to little change in J_c in low field at 20 K, but strong effects on the high field J_c at 5 K.

However, the MgO fraction was increased within the matrix through ball milling, which influences properties such as flux pinning. Further study of the ball-milling process thus promises to allow adjustment of the desired phase form, which should be optimized along with the sintering conditions, so as to create a balance between the inter-grain connectivity and the pinning centres. MgB₂ made with low grade B powder via solid state reaction could be particularly useful for industrial applications because of the reduced material cost, provided that the correct processing conditions are applied.

From a comprehensive study of ball-milling effects on the transport critical current density (J_{ct}) and grain connectivity factor (A_F) of MgB₂/Fe wires, it was observed that lattice disorder increased due to the ball milling. This caused both a slight reduction in the transition temperature and degradation of connectivity. The reduction in the transition temperature can change the upper critical field, so that the upper critical field is what is most affected by the lattice disorder. A significant increase in the upper critical field is the main cause for the enhancement of the critical current in the high field region. On the other hand, high temperature sintering in all types of samples can improve J_{ct} in the low field region, because it leads to good grain connectivity.

Using pyrene, C₁₆H₁₀, is effective for enhancing J_c of MgB₂ superconductor, even at sintering temperatures as low as 600°C. The advantages of using C₁₆H₁₀ include the production of highly active C due to decomposition of the pyrene and the introduction of small grain size due to low temperature sintering, resulting in enhancement of J_c . In addition, a power-law relationship between J_c and the n -value is observed in the log-log plot of $n \propto J_c^m$. The exponent m becomes higher for the higher n -value samples. Obviously, smaller m also reflects higher disorder due to low sintering temperature and more C substitution.

It is proposed that doping with carbon spheres effectively changes the intrinsic properties of MgB_2 and also reduces the grain size, which were both responsible for the enhancements of upper critical field and flux pinning force that were observed in the present work.

10.2 Suggestions for further work

- How to improve the density and reduce porosity in polycrystalline MgB_2 samples: Mg diffusion processing is the best solution to improve the density of MgB_2 bulk sample, but how to make wire samples is the key difficulty and could benefit from further work.
- How to combine the benefits of low temperature processing in terms of critical current density and irreversibility field with high physical density: for sintering at temperatures below 650°C , the reaction is completely solid-solid, so if a highly dense sample can be achieved, the grain connectivity must improve. If this could be achieved, low temperature sintering + long sintering time would definitely be the most desirable sintering conditions. These low temperature sintering conditions could also be beneficial for MgB_2 by allowing a wider choice of sheath material and by creating some defects that are useful as pinning centers. For sintering above 700°C , a solid-liquid reaction will begin to take place, due to the melting of Mg (solid + liquid), so these conditions make it much easier for porosity to appear during the cooling down process. Also, the density is very difficult to control, so that at these temperatures, vacuum sintering is the best way to control the porosity. The principle is same as creating glass bubbles to use glass to bond two pieces of ferrite materials for a magnetic head.
- Major inroads could be made on the grain connection problem if the mechanisms of the MgO effects in MgB_2 could be fully understood. This would include a comprehensive understanding of the effects of different sintering

atmospheres, and of the oxygen content from starting powders and even from the doping conditions.

Publications

- C. H. Jiang, **X. Xu**, and S. X. Dou, “Properties of pure and carbon sphere doped MgB_2 prepared from low grade boron powders”, *Supercond. Sci. Technol.* **21**(6): 5006 (2008)
- J. H. Kim, **X. Xu**, M. S. A. Hossain, D. Q. Shi, Y. Zhao, X. L. Wang, S. X. Dou, S. Choi, and T. Kiyoshi, “Influence of disorder on the in-field J_c of MgB_2 wires using highly active pyrene”, *Appl. Phys. Lett.* **92**, 042506 (2008)
- **X. Xu**, J. H. Kim, M. S. A. Hossain, J. S. Park, Y. Zhao, S. X. Dou, W. K. Yeoh, M. Rindfleisch, and M. Tomsic, “Phase transformation and superconducting properties of MgB_2 using ball-milled low purity boron”, *J. Appl. Phys.* **103**, 023912 (2008)
- W. K. Yeoh, J. Horvat, J. H. Kim, **X. Xu**, and S. X. Dou, “Effect of processing temperature on high field critical current density and upper critical field of nanocarbon doped MgB_2 ”, *Appl. Phys. Lett.* **90**, 122502, (2007)
- M. S. A. Hossain, J. H. Kim, **X. Xu**, X. L. Wang, M. Rindfleisch, M. Tomsic, M. D. Sumption, E. W. Collings, and S. X. Dou, “Significant enhancement of H_{c2} and H_{irr} in $\text{MgB}_2+\text{C}_4\text{H}_6\text{O}_5$ bulks at a low sintering temperature of 600°C ”, *Supercond. Sci. Technol.* **20** (8): L51 (2007)
- J. H. Kim, S. X. Dou, M. S. A. Hossain, **X. Xu**, X. L. Wang, D. Q. Shi, T. Nakane, and H. Kumakura, “Systematic study of a $\text{MgB}_2+\text{C}_4\text{H}_6\text{O}_5$ superconductor prepared by the chemical solution route”, *Supercond. Sci. Technol.* **20** (7): 715 (2007)
- J. H. Kim, S. X. Dou, X. L. Wang, D. Q. Shi, **X. Xu**, M. S. A. Hossain, W. K. Yeoh, S. Choi, and T. Kiyoshi, “The effects of sintering temperature on superconductivity in MgB_2/Fe wires”, *Supercond. Sci. Technol.* **20** (5): 448 (2007)
- M. S. A. Hossain, J. H. Kim, X. L. Wang, **X. Xu**, G. Peleckis, and S. X. Dou, “Enhancement of flux pinning in a MgB_2 superconductor doped with tartaric acid”, *Supercond. Sci. Technol.* **20** (1): 112 (2007)
- **X. Xu**, Dayse I. dos Santos, J. H. Kim, W. K. Yeoh, M. J. Qin, K. Konstantinov, and S. X. Dou, “Effect of Boron powder purity on superconducting properties of bulk MgB_2 ”, *Physica C* 460–462 **602** (2007)
- W. K. Yeoh, J. H. Kim, J. Horvat, **X. Xu** and S. X. Dou, “Enhancement of critical current density and irreversibility field by nano-carbon substitution in MgB_2 ”, *Physica C* 460–462 **568** (2007)
- W. X. Li, Y. Li, M. Y. Zhu, R. H. Chen, S. X. Dou, M. J. Qin, **X. Xu** and P. Yao, “Effect of magnetic field processing on the microstructure of micronsize Zn doped MgB_2 ”, *Physica C* 460–462 310 (2007)
- **X. Xu**, J. H. Kim, W. K. Yeoh, M. Rindfleisch, M. Tomsic, Dayse I. dos Santos,

and S. X. Dou, “Influence of Ball-Milled Low Purity Boron Powder on the Superconductivity of MgB_2 ”, *IEEE Trans. Appl. Supercond.* **17** (2): 2782 (2007)

- J. H. Kim, W. K. Yeoh, X. Xu, D. Q. Shi, and S. X. Dou, “Improvement of upper critical field and critical current density in single walled CNT doped MgB_2/Fe wires”, *IEEE Trans. Appl. Supercond.* **17** (2): 2907 (2007)
- W. K. Yeoh, J. Horvat, J. H. Kim, X. Xu, and S. X. Dou, “Effect of carbon substitution on the superconducting properties of MgB_2 doped with multi-walled carbon nanotubes and nano-carbon”, *IEEE Trans. Appl. Supercond.* **17** (2): 2929 (2007)
- W. X. Li, Y. Li, M. Y. Zhu, R. H. Chen, X. Xu, W. K. Yeoh, J. H. Kim, and S. X. Dou, “Benzoic acid doping to enhance electromagnetic properties of MgB_2 superconductors”, *IEEE Trans. Appl. Supercond.* **17** (2): 2778 (2007)
- J. H. Kim, W. K. Yeoh, M. J. Qin, X. Xu, S. X. Dou, P. Munroe, H. Kumakura, T. Nakane, and C. H. Jiang, “Enhancement of in-field $J(c)$ in MgB_2/Fe wire using single- and multiwalled carbon nanotubes”, *Appl. Phys. Lett.* **89**, 122510, (2006)
- J. H. Kim, W. K. Yeoh, M. J. Qin, X. Xu, and S. X. Dou, “The doping effect of multiwall carbon nanotube on MgB_2/Fe superconductor wire”, *J. Appl. Phys.* **100**, 013908 (2006)
- X. Xu, J. H. Kim, W. K. Yeoh, Y. Zhang, and S. X. Dou, “Improved J_c of MgB_2 superconductor by ball milling using different media”, *Supercond. Sci. Technol.* **19** (11): L47 (2006)
- X. Xu, M. J. Qin, K. Konstantinov, Dayse I. dos Santos, W. K. Yeoh, J. H. Kim, and S. X. Dou, “Effect of boron powder purity on superconducting properties of MgB_2 ”, *Supercond. Sci. Technol.* **19** (6): 466 (2006)
- W. K. Yeoh, J. H. Kim, J. Horvat, X. Xu, M. J. Qin, S. X. Dou, C. H. Jiang, T. Nakane, H. Kumakura, and P. Munroe, “Control of nano carbon substitution for enhancing the critical current density in MgB_2 ”, *Supercond. Sci. Technol.*, **19**(6): 596 (2006)
- J. H. Kim, W. K. Yeoh, X. Xu, S. X. Dou, P. Munroe, M. Rindfleisch, and M. Tomsic, “Superconductivity of MgB_2 with embedded multiwall carbon nanotube”, *Physica C* **449** (2): 133 (2006)